Low Temperature Force Microscopy on a Deeply Embedded Two Dimensional Electron Gas

James Augustin Hedberg

Department of Physics
McGill University
Montréal, Québec, Canada
2011

A thesis submitted to McGill University in
partial fulfillment of the requirements of
the degree of Doctor of Philosophy

ACKNOWLEDGEMENTS

Guillaume Gervais, I'm glad you called me at 6 in the morning hoping to get me on board with team ULT-SPM. Your support in every aspect over the years since has been unfailing. For this I am grateful.

To the other faculty who were part of the ULT-SPM collaboration: Michael Hilke, Peter Grütter, Roland Bennewitz, and Aashish Clerk, I thank you for offering your time, resources, and diverse expertise to the project.

Cory Dean, I couldn't have wished for a better companion in the early days, back when the sweet aromas of PVC glue filled the lab and dust from ceiling drillings floated through the air. I thank you for your friendship in trying times and for your generous council. Vera Sazonova, as time passes, I realize how lucky I was to have access to your talents for two years during the infancy and adolescence of the project. Your immense contributions to the development of both the microscope and myself will never be forgotten. Benjamin Piot, your stay in the lab and North America was all too brief. I'm indebted to you for your guidance in many ways.

Ashwin Lal, the latest addition to the ULT-SPM team, has taught me much in a short time. I'm glad he was there during our late night measurements. Yoichi Miyahara also should be recognized for his expert input and advice.

John Smeros has ensured the regular flow of precious cryogenic fluids to the lab - a duty not for the faint of heart and for which he deserves bounteous applause. Richard Talbot, whose fastidious handiwork is seen in many of the circuit boards through which flow the delicate electrons our work depends on, gets my wholehearted thanks for his contributions. I also thank Robert Gagnon, the go-to guy for almost all the miscellaneous systems and processes that power the CPM and who with infinite patience and resourcefulness was always there when called upon. All three of these men also lent critical hands (and backs) in the early days when the lab resembled more so a construction site than a physics experiment.

I thank Carlo Requiao da Cunha for his foundational contributions the microscope. The immaculate schematics and designs originally drawn by Leo Nikkinin were indispensable components of the instrument. Thanks also goes to Till Hagedorn for sharing his meticulous tip etching protocols with us.

From my desk in our basement lab, where the social graces of scientists are tested as much

as the equipment we build, I extend a hearty thanks to Michel Savard, Matthew Bonin, Ben Schmidt, Jon Buset, Guillaume Dauphinais, Xiaoqing Zhou, Andrew Mack, Jason Riordon, and Greg Crisp for making it an enjoyable and productive place to spend a few years.

To the future stars of science: Hugo Brandao, Anton Dubrau, Maryse Lapierre-Landry, Guillaume Lambert, and Jonathon Guillemette, who dedicated their precious summers, metaphorical or real, to the ULT-SPM project, I owe you gratitude for your contributions.

In the machine shop, my occasional Isle of Innisfree, I learned to shape the metals that once seemed so stubbornly set in their ways. For this I thank Steve Kecani, Pascal Bourseguin, and François Poirier. Special thanks also goes to Eddie Del Campo who like a midwife tended to and delivered from the womb of the CNC mill, the fragile skeleton of the AFM.

Diane Koziol, Elizabeth Shearon, Sonia Viera, Louise Decelles, Paula Domingues, and Lauren Kay deserve special thanks for their graceful handling of many seemingly impossible tasks. Thanks goes as well to Élise Saint-Jacques for assorted assistance.

The above acknowledgments have been entirely devoted to the professional aspects of this dissertation. In so doing, I might appear to be overlooking my friends and family and the roles they took in all of this. Nonsense. To all who share the water of life with me, I thank you for being where you were when you were there and not elsewhere, and drink deeply.

ABSTRACT

Experimental physics in the low temperature limit has consistently produced major advances for condensed matter research. Likewise, scanning probe microscopy offers a unique view of the nanometer scale features that populate the quantum landscape. This work discusses the merger of the two disciplines via the development of the Ultra Low Temperature Scanning Probe Microscope, the ULT-SPM.

We focus on the novel characterization of an exotic condensed matter system: a deeply buried two dimensional electron gas with a cleaved edge overgrowth geometry. By coupling the dynamics of the force sensing probe microscope to the electrostatics of the electron gas, we can remotely and non-invasively measure charge transport features which are normally only observable using physically contacted electrodes. Focusing on the quantum Hall regime, we can exploit the high sensitivity of the local force sensor to study spatially dependent phenomena associated with electronic potential distributions. The instrument shows promise for many exciting experiments in which low temperatures, high magnetic fields, and local measurements are critical.

Designed for operation at 50 mK, in magnetic fields reaching 16 T, many components of the instrument are not commercially available and were therefore designed and constructed in-house. As such, the intricate details of its design, construction and operation are documented thoroughly. This includes: the microscope assembly, the modular components such as the scan head and coarse motors, the electronics developed for controlling the instrument, and the general integration into the low temperature infrastructure. A quartz tuning fork is used as the force sensor in this instrument, enabling a wide selection between different modes of operation, the most relevant being electrostatic force microscopy. Noise limits are investigated and matched sources of experimental noise are identified. Detailed schematics of the instrument are also included.

ABRÉGÉ

La physique expérimentale aux limites des basses températures contribue constamment à des percées majeures dans le domaine de la matière condensée. Pour sa part, la microscopie à balayage de sonde offre la possibilité unique d'observer les éléments nanométriques qui caractérisent le paysage quantique. Ce projet allie les avantages de ces deux disciplines par le développement d'un microscope à balayage de sonde opérant à très basse température (Ultra Low Temperature Scanning Probe Microscope), le « ULT-SPM. »

Nous étudions en particulier un système exotique de la matière condensée : un gaz d'électrons bidimensionnel profondément enfoui, comportant une croissance latérale sur le bord clivé. Le couplage des forces dynamiques de la sonde du microscope et électrostatiques du gaz à électrons, nous permet de mesurer à distance et de façon non invasive, les caractéristiques de transport des charges, qui ne sont normalement observables qu'à l'aide d'électrodes et donc, par un contact physique. Dans le régime de l'effet Hall quantique, nous pouvons exploiter la grande sensibilité du capteur de force local pour étudier des phénomènes spatiodépendants associés aux distributions de potentiel électronique. L'instrument se révèle prometteur pour la poursuite de nombreuses expériences passionnantes où les conditions de basse température, champ magnétique élevé et mesures locales sont essentielles.

Comme il est conçu pour fonctionner à 50 mK et sous un champ magnétique pouvant atteindre 16 T, plusieurs composantes du microscope ne sont pas disponibles commercialement et ont donc été entièrement conçues et fabriquées sur place. Les détails intrinsèques de la conception, de la construction et du fonctionnement sont ainsi documentés à fond. Ceci inclut : l'assemblage du microscope, les composantes modulaires comme la tête de balayage et les moteurs, l'électronique des contrôles de l'instrument et l'intégration à l'infrastructure opérant à basse température. Dans cet instrument, un diapason de quartz fait office de capteur, ce qui permet une grande flexibilité quant aux différents modes d'opération, le plus utile étant la microscopie de force électrostatique. Les limites de bruit sont étudiées et comparées aux sources de bruit expérimentales. Les schémas détaillés de l'instrument sont également inclus.

STATEMENT OF ORIGINALITY

The author, JH, claims the work contained herein to be an original contribution to the scholarship of experimental physics. Some of the results have been published where mentioned.

The author's specific contributions are widespread and encompass all phases of the project.

- *Laboratory Space - Design and Construction:* The overall conception of the lab space and instrument were in place before JH's arrival. Upon completion of the institution lead construction phase, JH and other lab members began the construction of the various, large scale infrastructure components. This is documented in chapter 3.
- *The Apparatus:* Preliminary aspect of the apparatus design were sketched before JH's arrival as well. JH contributed to the finalized design phase and the construction of the apparatus leading to a functioning instrument. Chapter 2 discusses this.
- *Operation:* Characterization of the apparatus was performed by JH. Results of this work are found in chapter 4.
- *Experimental Work:* The first results from the instrument were obtained in experiments performed by JH. These have lead to a publication [Hedberg et al, Appl. Phys. Lett. **97**, 143107 (2010)];

An article describing the instrument is currently in preparation.

Contents

LIST OF FIGURES

LIST OF TABLES

LIST OF SYMBOLS & ABBREVIATIONS

Δf	The frequency shift of the tuning fork
μ	carrier mobility
ν	filling factor
ω	angular frequency $= f \times 2\pi$
ω_c	The cyclotron frequency of a charged particle in a magnetic field $= (eB)/m^*$
Φ	contact potential difference
ϕ	phase of an oscillator
B	magnetic field strength
C	capacitance
e	charge of an electron $= 1.602 \times 10^{-19}$C
E_F	Fermi energy
f	frequency of an oscillator
f_0	resonant frequency of an oscillator
h	Planck's constant
k_B	Boltzmann's Constant $= 1.38 \times 10^{-23}$
l_B	magnetic length $= \sqrt{\hbar/eB}$
m^*	The effective/reduced mass (0.067 m_e for an electron in GaAs)
1,2,3D	one, two, three dimensional
2DEG	Two-dimensional electron gas
ac/dc	alternating current/direct current
AFM	atomic force microscope
BW	measurement bandwidth
CEO	cleaved edge overgrowth

cooldown Here I refer to the entire process of bringing the microscope from room temperature in air to the 4 K or lower high-vacuum environment.

E Young's modulus

EFM Electrostatic force microscopy, sometimes with an ac or dc prefix as well

F/IQHE fractional/integral quantum Hall effect

FM-AFM frequency modulated Atomic Force Microscopy

I-V current to voltage, as in a current to voltage converter

LL Landau level

MBE molecular beam epitaxy

PLL phase locked loop

PZE piezoelectric effect

PZT Lead zirconate titanate, the standard ceramic used in many of the ULT-SPM piezoelectric devices

Q quality factor

S/N signal to noise ratio

SdH Shubnikov-de Haas

SPM refers to scanning probe microscopes in general. That is, STM, AFM etc..

STM scanning tunneling microscope

t-s tip-sample, for example the force between the tip-sample: $F_{\text{t-s}}$

TF tuning fork

topo Short for topography, the physical features of the surface

ULT-SPM Ultra-low temperature scanning probe microscope. I use this to describe the experimental apparatus as a whole

VCO voltage controlled oscillator

CHAPTER 1

INTRODUCTION AND CONTEXT

1.1 Introduction

This thesis documents the development and application of a new scientific instrument. In the ever present cycle linking theory and experiment, both sides require continual improvements to their tools. As will be discussed in the following pages, our tool is the ULT-SPM: Ultra Low Temperature Scanning Probe Microscope. The organization of the thesis is as follows.

CHAPTER 1: INTRODUCTION TO SPM AND LOW TEMPERATURE MEASUREMENTS

Containing an overview of scanning probe microscopy (SPM), its applicability to experimental physics, and the importance of low temperature environments. A review of similar apparatuses is also presented.

CHAPTER 2: AFM DESIGN AND CONSTRUCTION

Considerations, concerns and details regarding the design and construction of the atomic force microscope (AFM). Mechanical as well as electrical issues are discussed.

CHAPTER 3: LOW TEMPERATURE INFRASTRUCTURE

How to integrate the SPM with a low temperature apparatus and ensure both components function well together.

CHAPTER 4: CHARACTERIZING THE AFM IN LOW-T, HIGH B

Benchmarks regarding the performance of the instrument and details of operation at low temperature in high magnetic fields.

CHAPTER 5: THE CLEAVED EDGE OVERGROWTH

An example system studied with the ULT-SPM: Novel characterization of an exotic mesoscopic system. Force microscopy is used to investigate electronic properties in the Quantum Hall regime.

CHAPTER 6: OUTLOOK

What to do with it next.

1.2 SPM

Probe Microscopy Basics

While analytical inquiries into modern physics have the opportunity to declare a temperature, T, equals zero, or that a given length is small and can therefore be ignored, and in so doing allow for otherwise masked consequences of the quantum mechanics to emerge, experimental approaches are not so blessed, and must create as best they can, such conditions in the lab. This has led to the continual effort in experimental science to create new tools that can operate at the extremes of nature. Likewise, as circumstances forced a reduction in the size of modern technologies, the need for instrumentation capable of characterizing matter on the scale of nanometers grew. Thus was born the Scanning Tunneling Microscope (STM).[1, 2] Combining newly harnessed powers of piezoelectric crystals which permitted precise mechanical actuation on the scale of nanometers with some long established consequences of quantum mechanics, the STM became the first of many variations on the theme of probe microscopy. The unifying theme being: pick an interaction that has a position dependence at short length scales and then monitor this interaction as a function of position, all within a very small area. Figure 1.1 schematically portrays this concept.

In the case of the STM, the interaction is the tunneling current that flows between two conductors at different potentials, separated by a potential barrier. This current is exponentially dependent on the distance between the two conductors and can therefore be used as a measure of the separation between the two elements. Once we have in place the notion of a distance dependent interaction in addition to fine control over the positioning of the interaction sensor, we are free to substitute different interactions in place of the tunneling current. For example, without even changing the instrumentation set up, the STM can also probe electronic properties, since the tunneling current not only depends on position, but also on additional factors such as the local electronic density of states. In the last three decades, dozens of acronyms have been coined to describe the cornucopia of new types of probe microscopy: EFM, SCM, SGM, MFM, NSOM... The list grows continuously to this day and offers inspiration for new instrumental advances.

As evidenced by the multitude of probe techniques, each one must have its own virtues and limitations. In the case of STM, there needs to be a tunneling current between the probe and the sample under investigation. This effectively rules out an entire class of samples where the surface material is nonconductive, or the area of interest is buried deep underneath an insulating capping layer.[1] To overcome this limitation, the scanning force microscope (SFM) was introduced, following quickly on the heels of the STM.[3]

[1] Advances have been made in this direction recently, but the statement in general still applies.

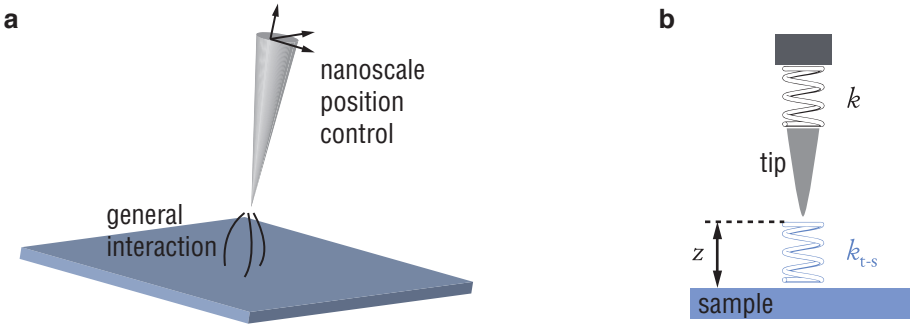

Figure 1.1: **a**: A generalized interaction between a generalized tip and sample. The interaction strength depends on position and the tip is capable of nanoscale motion in all three dimensions. **b**: The effective, distance dependent spring constant $k_{t\text{-}s}$ created by the tip-sample interaction.

Relying on the relation expressed so succinctly by Hooke's Law:[4]

$$F = -kx\,, \tag{1.1}$$

the force microscope measures the changes in the force, F, exerted on a small, spring-like probe with a spring constant k, while it is interacting with a second body, henceforth called the sample.[2] Numerous methods exist in which this relationship can be exploited, each essentially capturing a type of force microscopy. For example, in static force microscopy, the probe, which is really a lever fixed on one side with the opposite side free to interact, is held in contact with the sample and scanned over an area. If the deflection, x, it suffers due to the interaction with the surface is held constant by adjusting its relative position to the surface, it will result in a mapping of the z profile of the surface: a standard contact-mode, topographic image results. This was the original mode of operation for atomic force microscopy (AFM).

An even more effective mode, at least for many desirable applications, uses an oscillating beam, or cantilever rather than a static deflector. Known collectively as dynamic mode atomic force microscopy (DM-AFM), the force gradients, ∇F, near the sample becomes the measurable quantity. The force gradients act as an effective spring constant for the system, $k_{t\text{-}s} = \partial F/\partial z$, which leads to frequency shifts, Δf, of the resonant cantilever, conceptualized in figure 1.1**b**. In the limit of small oscillation amplitudes, typically less than 1 nm, the resonant frequency of

[2]It should be noted out of historical interest that Robert Hooke was also responsible for some of the very first microscopic images to be published, shown in his work *Micrographia*,[5] wherein he visually documented the strange new landscape of the very small, drawing specimens such as fleas and needle points as they appeared through the eyeglass of his microscope.

the oscillator, f_0, will be altered according to:[6]

$$\frac{\Delta f}{f_0} \cong \frac{1}{2k}\frac{\partial F}{\partial z}\,. \tag{1.2}$$

Several methods have been used to detect this frequency shift. Initially, the resulting change in amplitude, A, caused by the Lorentzian line shape of its resonance curve shifting in the frequency domain, was used as the signal of interest, as seen in figure 1.2**a**.[7] However, this method suffers from long time scales for measurement acquisition since the time needed to allow for changes in amplitude was determined by the quality factor of the resonator, a parameter that in general improves measurements as it increases.[3] Thus, an improvement was made in which the frequency shift was monitored directly, via the zero-crossing of the oscillator's phase, allowing for improved measurement bandwidths.[8] This mode, called Frequency Modulation AFM (FM-AFM) (Figure 1.2**b**) has proven itself useful in many contexts and will be used often in our studies. Innovations continue to the present day and the capabilities of instruments based on these approaches are still improving.

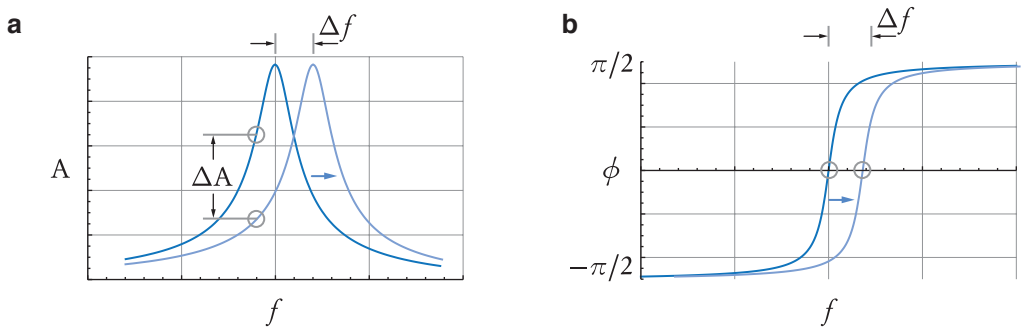

Figure 1.2: **a**: Slope, or amplitude detection of a changing resonance. **b**: Phase detection offers a much faster means. The grey circles indicate the measured quantities.

Of course, little interest would be given to such developments had there not been something useful to gain. That is, how has this instrumentation helped and why does the world need more of them?

Relevant Applications of Force Microscopy

Best known to the world for its ability to measure surface topographies at the nanoscale, the AFM has indeed proven itself an indispensable component to modern surface science. Nonethe-

[3]The time scale for this amplitude modulation based measurement scheme is given by the characteristic time $\tau = 2Q/\omega_0$, where Q is the quality factor of the resonator and ω_0 the resonant angular frequency. Appendix B contains more about the quality factor of an oscillating beam.

less, even in the early years of its conception, it was immediately obvious that the potential for much more existed.[9] Since the tip and the sample form a capacitively coupled system, described by a geometrically defined capacitance, C, there will exist an electrostatic force, F_{ES}, between the two components given by:[10]

$$F_{\text{ES}} = \frac{1}{2}\frac{dC}{dz}V_{\text{t-s}}^2\,, \tag{1.3}$$

where $V_{\text{t-s}}$ accounts for the potential difference between the tip and the sample. Since the $V_{\text{t-s}}$ term affects the force on the sensor, and it can change locally, the microscope can now resolve position dependent electrostatic forces. A host of possibilities now presents itself.

From a technology standpoint, the ever increasing need for nanoscale electronics has provided ample opportunity for the characterization of devices by force microscopy. Modern electronics function in part, due to control over the location of charge carriers, to say it bluntly. As the critical length scales of such devices continue to decrease, more sophisticated methods are required to characterize the distribution of these charges. AFM has provided a means to map potential distributions, non invasively, and with the requisite spatial resolutions. Tasks such as failure analysis in RAM devices,[11, 12] ionic current mapping in fuel cell membranes,[13], Si doping analysis,[14] just portray a few of the technologically relevant applications that AFM's sensitivity to electronic properties has provided to industrial research labs. (For more thorough reviews, see refs. [15],[16], [17], and [18])

As an industrial tool, there is no question about the importance of force microscopy. Likewise, in the realm of more fundamental research into the physical sciences, the AFM also offers a unique access point to the microscopic underpinnings guiding macroscopic phenomena. With Planck's quanta of action and the revolutions of quantum mechanics that were soon to follow, it became all the more desirable to have experimental access to the terraced landscapes of atoms and winding paths of electrons. As Planck himself pointed out,

> The material with which theoretical physics operates is measurements... All physical ideas depend upon measurements, more or less exactly carried out, and each physical definition, each physical law, possesses a more definite significance the nearer it can be brought into accord with the results of measurements.[19]

Slowly, real apparatuses were devised that could take the place of the ubiquitous Gedanken experiments from which sprang so many of quantum theory's initial elaborations. Generally speaking, to access the quantum regimes, it was clear that the length scales probed by any experiment had to be small. Objects with relatively large quantum mechanical wavelengths, $\lambda > 10^{-9}$ m, were ideal. Given large wavelengths, systems with critical dimensions in the order of nanometers were likely to exhibit quantum effects.

Coincident with the desire to become small, is also the notion that by reducing the number of dimensions relevant to a physical system, we can heavily influence the physics that guides that system. If the standard translational degrees of freedom for the microscopic entities of a system, be they electrons, photons, phonons, etc..., are restricted below the usual 3 that accompany our terrestrial life, we obtain a low-dimensional system. Thus, confining electrons to a planar region requires 2D physics. Helium atoms in a row become 1D. An exciton stuck in a potential well requires a 0D treatment. Each reduction in dimensionality requires a reevaluation of the physical laws which govern. Of course, we can never truly escape the three dimensional cage of reality, but using recent advances in materials science, we can create structures and systems that are small enough to manifest reduced dimensionality. Considering the above mentioned request for measurement, the force microscope has all the capabilities necessary for realizing a wide variety of experimental situations, all with the goal of probing the unique properties of matter with small length scales.

Let us briefly pick a few examples of reduced dimensionality systems and examine the role probe microscopy can play.

Two-Dimensional Systems

Quantum Hall: A widely studied 2D electronic system studied with force microscopy is the quantum Hall regime.[20, 21] To be discussed in greater detail later in the text, we can just mention here that when confined to a planar region, charge transport in the presence of an externally applied magnetic field exhibits features only explainable through quantum mechanics. Exotic phenomena such as quantized Hall resistance, fractionalized charges, and zero-resistance states are all manifested in the context of quantum Hall physics. It has been established that the mechanisms behind these features manifest in real space and therefore can be mapped with position sensitive measurements.[22] Again, length scales are important here. While the Quantum Hall Effect (QHE) can be observed in large, macroscopic samples with mm scale extension, many of the facets worth probing are confined to smaller, sub-micron scale areas, most notable being the edges of the sample.[23] Experiments to date have focused on mapping electric potential distributions as functions of position and applied magnetic field, yielding spatially relevant information unavailable through standard transport measurements. We will return to the quantum Hall effect in chapter 5 as an important system for study using the ULT-SPM.

Electron Crystal: While not limited to 2D structures, electron crystallization has been shown to be more realizable in a system confined to two dimensions. As the kinetic energies of the electrons in the 2D gas are reduced due to decreasing the density, the potential energy given by Coulomb repulsion dominates. Minimizing the potential energy of the system requires a

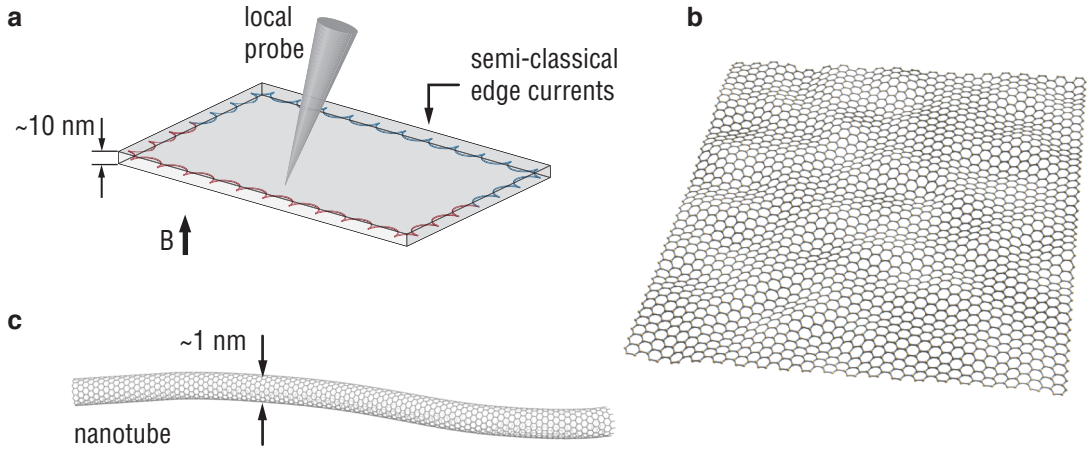

Figure 1.3: **a**: Charges confined to 2D in the presence of a perpendicular magnetic field leading to Quantum Hall Effects. **b**: A graphene sheet - the closest thing to 2D we can make. **c**: A carbon nanotube.

periodic lattice, and so an electron crystal, or Wigner Crystal after the initial discoverer, can be formed under the appropriate conditions.[24] Detecting such exotic states has so far proved possible only via indirect transport measurements. However, since single electron resolution is possible to a variety of force microscopy techniques, and the lattice spacing of the crystals, while variable, can be tuned to the order of 100 nm, observing a Wigner Crystal in 2D should be within reach of a force microscope.

Graphene: The most popular playground for condensed matter physics at the moment is arguably the recently discovered monolayer crystals of carbon: graphene.[25] As a 2D, single atom thick, conducting plane, graphene plays host to many of the same phenomena studied previously in 2D systems, but in its own unique way. For example, quantum Hall physics has been reproduced in graphene, with some modifications.[26] The molecule also presents many options for probe microscopy. With every atom being a member of the surface, unlike most other materials, there is little or no obstruction between a force microscope probe and the area of interest, as compared to the standard electron gas structure which is always buried underneath a capping layer of some kind. To date, only a few experiments which rely on force microscopy to characterize the electronic properties of graphene have been undertaken (eg: [27],[28]). As sample preparation becomes more routine and reliable, it is likely that SPM will have a lot to contribute to this burgeoning field of research.

One-Dimensional Systems

Carbon Nanotubes: Before graphene stole the spotlight, the quasi 1D carbon structures known as carbon nanotubes (CNT) were all the rage.[29] Scores of reports documenting the use of SPM to probe the electronic transport properties of CNTs exist. Commonly, the probe tip can be used to visualize where along the CNT relevant transport phenomena occur. For example, defects in the tube structure can be located and correlated to conduction properties.[30]. Also, semiconductor-metal transitions can be induced via localized pressure from the AFM tip.[31] (For a review of transport in nanotubes probed by AFM, see [32])

Quasi 1D constrictions: The Quantum Point Contact (QPC) offers another means to force currents into nearly 1D channels. Quantized conductance values in line with expectations for 1D current flow are measured using such devices. Using an AFM probe as a movable, local gate allows for very fine control over the currents passing through these constrictions. Electron trajectories have been mapped to great success using QPCs and SPMs.[33]

Quantum Hall, pt. II: Again, we should briefly mention the quantum Hall regime here in the context of 1D systems. Although the mechanism underlying the QHE are based in a 2D analysis, the phenomena can manifest as quasi 1D (as shown semi-classically in figure 1.3). The quantum Hall edge states, to be discussed in greater detail later, can be considered as 1D conduction channels.

Zero-Dimensional Systems

Quantum Dots: If the dimensions of a system are restricted in all three dimensions until relevant length scales are smaller than the characteristic length of the confined particles, a quasi-zero dimensional system will be formed. Generally referred to as quantum dots (QD), these systems have generated much excitement as potential candidates for a wide variety of applications, but they are also interesting as model systems as their properties can be approximated quite well by basic quantum frameworks. Rather than bulk systems where the number of particles is large, i.e. $N \to \infty$, QDs can operate in the single charge regime. Force microscopy has been able to probe these systems very effectively using many different techniques. For example, by coupling the cantilever to the dynamical aspects of charges, electronic structures of QDs have been described.[34]

1.3 Low Temperature Physics

Absent from the previous discussions was any mention of one of the more critical experimental parameters that effects all experimental physics: temperature. As new technologies allowed for accurate and wide range control over temperature, in particular towards the direction of absolute zero, low-temperature physics has become a discipline in itself.

Kamerlingh Onnes reported the immeasurably low resistance of a mercury wire upon reaching very low temperatures in 1911. Immediately, the theoretical gears of the scientific machine set to work on an explanation. Yet, it would take until 1957 for a complete microscopic theory to emerge at the hands of Bardeen, Cooper, and Schrieffer.[35] In the four decades occupying this gap between observation and explanation, it was slowly accepted that the standard frameworks for electrical conductivity and resistance could not be massaged or modified to account for the phenomena Onnes called superconductivity. New physics was needed.

Similarly, the quantized resistances of the QHE might never have been noticed without the aid of low temperature experiments. In this case, as the sample temperature was reduced, the energy levels of the quantized states became relevant when compared to the thermal energy. With energy scales given by the Landau quantization for charged particles in a magnetic field, B:

$$E_N = (N + 1/2)\hbar\frac{eB}{m^*}, \tag{1.4}$$

where e is the electron charge and m^* is the particle's effective mass, we can expect energy level separations, ΔE_N, of 2.6 meV at for electrons in GaAs at magnetic fields of 1 T. Thus, as temperatures are reduced below 30 K, the thermal energies, $k_B T$, become smaller than the Landau level spacing. Continuing further towards $T \to 0$, we will reach the regime where $k_B T \ll \Delta E_N$. Only in this regime, can we expect to observe the subtle yet potent quantum Hall effect.

While these two examples highlight major conceptual advances due in part to our abilities to manipulate matter at low temperatures, we have much to gain from a signal to noise perspective as well. While the reasons for going to low temperatures are plenty, we can point to several that have direct influence on the project at hand.

1. Carrier mobility, μ, in semiconductors describes *how well* the charge carriers move during transport. High mobility samples, where $\mu > 10^6$ cm^2/V$\cdot$s, are required for experiments which seek to bring out many of the exotic quantum states. Fortunately, many of the scattering mechanisms which reduce the mobility are correlated with temperature, and can be reduced significantly by working at low temperatures. [36]

2. Johnson-Nyquist noise,[37, 38] which we must deal with when a resistance, R, is present in an electric circuit, leads to a root mean square voltage noise, δV_{RMS}, with dependencies

on the measurement bandwidth, BW, and temperature T:

$$\delta V_{\mathrm{RMS}} = \sqrt{4 k_B T R \,\mathrm{BW}}\,, \tag{1.5}$$

and can therefore be reduced by lowering temperatures.

3. The frequency noise during measurement of a mechanical oscillator also decreases with temperature:[8]

$$\delta f \propto \sqrt{\frac{T}{Q}}\,, \tag{1.6}$$

and as the quality factor, Q, increases at low temperatures, we have much to gain by performing FM-AFM at low temperatures.

4. Thermal drift, wherein the relative positions of mechanical components shift over the course of a measurement due to thermal fluctuations, a major problem for room temperature instruments, is also significantly reduced at low temperatures.

The above list offers some general motivations for low temperature physics, which in combination with the more dramatic motives mentioned earlier, make a good case for pursuing microscopy in the low-T limit. But, nothing comes without a cost. The realization of low temperature experimental physics requires significant instrumentation, with every step closer to absolute zero harder than the last. As we'll see in the following chapters, this requires some concerted effort.

1.4 Review of Low-T Force Microscopes

The marriage of low temperature physics and force microscopy was inevitable. Even the 1986 paper announcing the new instrument suggests a 300 mK version, in the hopes of lowering the noise floor.[3] Figure 1.4 shows the rapid pace at which experimental temperatures in force microscopy have declined in recent years. Highlighted are a few notable achievements that overcame previous difficulties and spurred the ongoing development. [4]

Binnig, Quate and Gerber, PRL 1986

This publication announced the AFM to the world and started the very prolific field of force microscopy. Originally a hybrid system between a cantilever and an STM tip, the early AFMs used the tunneling current from a nearby STM tip to measure the deflection of the cantilever

[4] We will forego discussion of instruments designed only for STM application, since that could comprise an entire thesis separately.

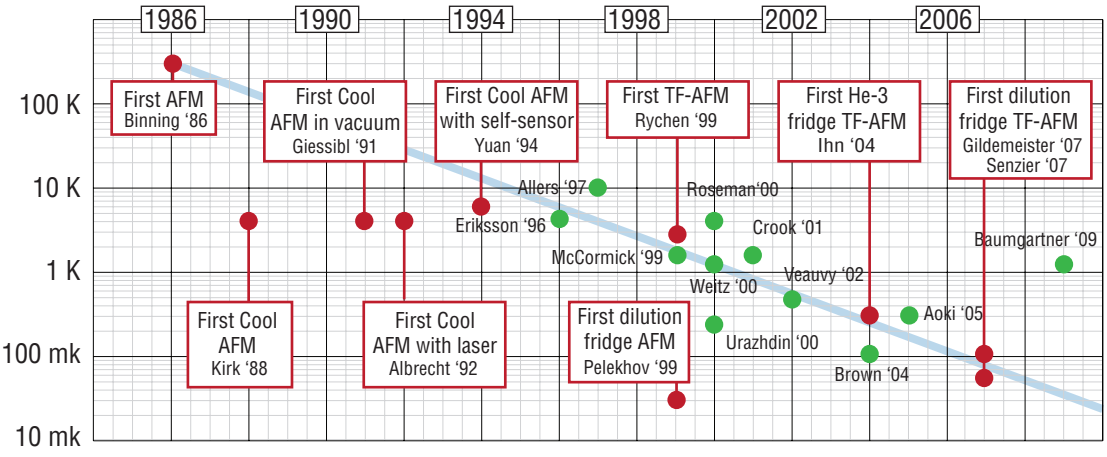

Figure 1.4: A review of the literature for low temperature force microscopes in the last 2 decades.

allowing for highly sensitive surface mapping of samples in a non-destructive manner. While the instrument discussed in this paper operated at room temperature, a prescient line from the third page reads:

> If the system is cooled below 300 mK we estimate that the lower limit [in force sensitivity] will be 10^{-18} N.

And thus the low temperature AFM was conceived.[3]

Kirk, Albrecht, and Quate, RSI 1988

A mere two years later, the Stanford group essentially submerged a similar system into liquid helium, thereby performing the first force microscopy at 4.2 K. While operating in liquid helium was found to be somewhat less than ideal, the instrument opened the door to further improvements.[39]

Giessibl, Gerber, and Binnig, J. Vac. Sci. 1991

While still using the STM tip as the deflection sensor, the IBM researchers in this 1991 paper constructed an 4 K AFM that operated in vacuum, rather than liquid. The performance of the microscope was improved, though atomic resolution still remained unclaimed at this point.[40]

Albrecht, Grütter, Rugar, and Smith, Ultramicroscopy, 1992

A major improvement in usability and performance arrived when a fiber interferometer was employed to measure the cantilever deflection rather than the tunneling current from a nearby STM tip in the previous three instruments. 16 Å crystal planes of a high-Tc superconductor were imaged at room temperatures, and magnetic bits from a recording medium were visible at 5 K. This instrument also featured a solenoid surrounding the sample permitting the application of external magnetic fields.[41]

Yuan, Batalla, Zacher, De Lozanne, Kirk, Tortonese, APL, 1994

While interferometric detection schemes proved highly useful for many AFM setups, their application to low-T AFM is somewhat problematic. First of all, simply aligning the laser and cantilever at low temperature can be quite difficult. Secondly, heat dissipation from the laser can be significant. And, perhaps most importantly, many of the semi-conductor based samples destined for the ULT-SPM are sensitive to light. These considerations encouraged researchers to find alternative deflection means. The piezoresistive cantilever[42] offered a way out of optical deflection. This work showed the application of such a cantilever in a low temperature force microscope, demonstrating the feasibility of self-sensing cantilevers in such apparatuses. Temperatures were still limited to > 4 K and the resolution of the instrument was not quite up to today's standards.[43]

Pelekhov, Becker, Nunes, RSI, 1999

Although milliKelvin environments offered by dilution refrigerators had been common in low temperature physics labs for decades, the previous instruments were all connected to standard liquid helium reservoirs, meaning their base temperatures would be 4.2 K. The Dartmouth group showed the first successful combination of a dilution unit with an AFM. Although their instrument would prove not entirely useful, it was a wonderful proof of concept showing that milliKelvin AFM was possible. Just like the first low-T AFM reported above, the basic strategy was to simply insert an AFM into the cryogenic liquid. Rather than just ^{4}He however, the microscope was placed inside the mixing chamber of the dilution fridge, where the ^{3}He/^{4}He mixture was cooled to 20 mK (Section 3.2 will discuss these in detail). Operating the cantilever in the superfluid proved difficult as large frequency shifts were observed as well as a large decrease in the quality factor. The reported noise floor of 6 Å was quite high for force microscopy at the time. Magnetic field up to 9 T were applied however, which showed that high-field microscopy at low temperatures should be possible. Despite mixed results from the instrument, the closing line of the paper captures the spirit best:

Clearly, this is an area worthy of future study.[44]

Rychen, Ihn, Studerus, Herrmann, Ensslin, RSI 1999

In what has become a standard methodology for low-T force microscopy, the ETH Zurich group was the first to construct a low-T instrument which utilized the recently developed quartz tuning fork force sensor[45]. Its piezoelectric properties were exceedingly useful as it permitted a self-sensing cantilever that has turned out to be very compatible with low-T environments. The microscope successfully imaged in FM-AFM mode at 2.2 K and was compatible with high-field (8 T) environments. Another key achievement from this report was the integration of a phase-lock loop (PLL) in the measurement electronics. Although already shown effective at room temperatures[46, 45], the PLL is now an almost standard component in low-T cantilever deflection electronics.[47]

A divergence in the force

At this point in the history, the field of low-T AFM branches into two forks. One thrust continues towards improving the resolution of the microscopes while staying within the 4 K temperature regime. Very impressive instruments have been constructed in this vein.[48, 49, 50, 51] Other groups decided to press on towards lower temperature regimes. This second branch is more relevant to the instrument presented here.

Weitz, Ahlswede, Weis, von Klitzing, Eberl

The von Klitzing group has contributed significant advances to the low-T scanning force community. Again employing the piezoresistive cantilever at about 1 K, the instrumentation did not differ drastically from the previous efforts. However, important results were obtained from their microscope. They have studied in depth the edge states of the quantum Hall regime using highly specialized samples made with probe microscopy in mind (an issue we'll turn to later).[52]

Ihn, 2004

The next generation of low-T SPM from the ETH Zurich showed a marked improvement in instrumentation. Rather than simply relying on ^{4}He in the liquid state, this apparatus was based on a ^{3}He refrigerator. Operating in vacuum, but thermally connected to the 300 mK cold plate, the AFM suffers none of the distortions from liquid operation as reported in the previous instruments, while still maintaining the low temperatures expected of the more advanced insert. The force sensor and detection scheme in this instrument continue the tradition of the PLL/tuning fork setup.[53]

Gildemeister, Ihn, Barengo, Studerus, Ensslin, RSI, 2007

Not content with ^{3}He alone, the next instrument reported by the ETH Zurich group finally presented an AFM mounted to, rather than inside, a dilution refrigerator. A natural extension of the previous instrument, the experimental temperature range of force microscopy in the instruments reaches comfortably to 100 mK. Magnetic fields up to 6 T were noted to have no observable influence on the scanning assembly, however, no data was presented which incorporated magnetic dependencies.[54]

Senzier, Luo, and Courtois, APL 2007

Right on the heels of the previous instrument, the CNRS group from France successfully modified their existing STM[55] to allow for force measurements by incorporating a tuning fork based sensor. Their work presented 90 mK images, although no magnetic fields were applied in the measurements.[56]

ULT-SPM: 2010

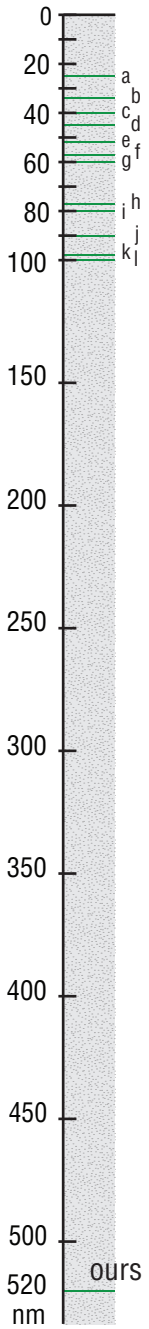

Figure 1.5: 2DEG depths from the literature.

And thus we are ready to explore how our ultra low temperature scanning probe microscope (ULT-SPM) was designed, constructed and applied. The following chapters should be useful as a guide for anyone interested in pursuing this line of instrumentation research.

Our initial experiments with the ULT-SPM will deal with a Quantum Hall (QH) structure as described earlier. We will show the effective coupling between the cantilever force sensor and the electronic states in the QH regime, which has the potential to reveal highly useful spatial information regarding the distributions of currents in these samples. Our work builds on previous studies with similar motivations but departs in several interesting aspects. Most importantly, the electron gas used is located very far from the surface of the sample. As seen in the graphic in figure 1.5,[5] which plots the relative depths of several other studies involving scan probes and 2DEG systems, our 2DEG is located about an order of magnitude further away from the surface. This is desirable in some ways, since the more isolated from the external environment the electron gas is, the less scattering related mobility losses occur. As noted earlier, these losses can preclude the formation of many of the exotic states found in such systems. At the same time however, burying the 2DEG under more than 500 nm of insulating material severely reduces the interaction strength between the tip and the charge carriers in the structure, thus demanding extremely low level measurement capabilities from the instrumentation.

We will focus our attention on the edge of the QH system under investigation. As will be made clear later, the edge deserves attention as a complete picture of the mechanisms at play on the edge of a QH system is still wanting. At present, there are few methods available for characterizing the sub-micron size features of the edge transport. The SPM boasts several modes of operation that have the potential to resolve some of the questionable properties of the edge.

[5]References from the graphic: a: [57], b: [58], c: [49], d: [59], e:[60], f: [61], g: [62], h: [63], i: [64], j: [65], k: [66], l: [67], ours: [68]

CHAPTER 2

AFM - DESIGN AND CONSTRUCTION

2.1 Introduction to AFM construction

While the proliferation of commercial AFMs has made their use accessible to nearly any research topic in need, the general product lines of most companies have yet to reach the extremes of conceivable applications. Thus, to perform force microscopy experiments in milliKelvin and high B-field environments, the only option is to *build one yourself*. As seen in the first chapter, other research groups have attempted this previously, thus a growing body of knowledge is available to help guide the design and realization of a ULT-SPM.

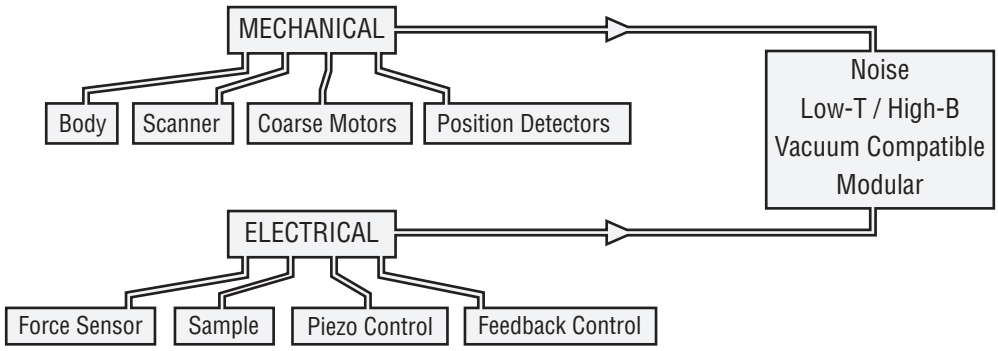

Figure 2.1: A schematic portraying the main concerns regarding the design and construction of the ULT-SPM. All the factors are interrelated and while conceiving of each individually is necessary, attention must also be paid to the apparatus as a whole.

This chapter guides us through the various considerations, requirements, and choices that when summed together, led to the ULT-SPM in its current configuration. As shown in Figure 2.1, we can divide the features of the AFM into its mechanical and electrical components and examine how factors such as noise, the extreme environments, and usability entered into its realization.

2.2 Mechanical Design

Corpus

There are several major considerations influencing the large-scale design of the microscope.

- *Spatial constraints are the most obvious.* The superconducting magnet has a bore of 52 mm, and the interior diameter of the vacuum can is just 47 mm, thus, the entire microscope must be no bigger than $\sim$ 40 mm in diameter. There is more room in the vertical direction, but exact positioning is paramount as the region of maximum field is only 1 cm^3 and the sample needs to be located carefully within this region.

- *Most of the other major restrictions arise from the extreme nature of the experiment.* The microscope must be able to withstand repeated transitions from room to milliKelvin temperatures, be compatible with high vacuum environments, and provide the necessary electrical and magnetic properties. Many materials commonly used in probe microscopes are not suitable for such applications. Drastic deformations from repeated thermal expansions and contractions can occur, as well as more fatal cracking and breaking due to rapid temperature changes. In addition, all materials must be minimally affected by the external magnetic field. Finally, any material with a superconducting transition temperature above 50 mK cannot be used since uncontrollable eddy currents will form due the changing field strengths.[1]

- *An often neglected design issue that should also be considered is ease of use.* Handling the microscope needs to be a relatively facile process since samples and tips need repeated replacement and any repairs or maintenance operations need to be able to be performed without drastic dismantling. For this reason, a modular design was chosen making the instrument more accessible to the experimentalist. Cables that need to be removed frequently should be mated using connectors, when possible.

Body

The main body of the microscope was made from the machinable glass ceramic Macor[69]. Shown to be successful by other groups pursuing similar applications [51, 70], Macor was one of the few options available given the environmental restrictions of the experiment. It has a minimal thermal expansion coefficient[2] in the relevant temperature scales, is non-superconducting,

[1] Even though at fields above the critical field, B_C, the superconducting state is destroyed, the concern is still valid

[2] The ratio of the change in length ΔL to the undeformed length, L, per degree Kelvin, is used to measure the thermal contraction of a material. For Macor: $\Delta L/L = 74 \times 10^{-7}$/K[69]

and is not affected by the external magnetic fields. Using slow feed rates in the CNC milling machine enables Macor to be machined with very accurate precision.

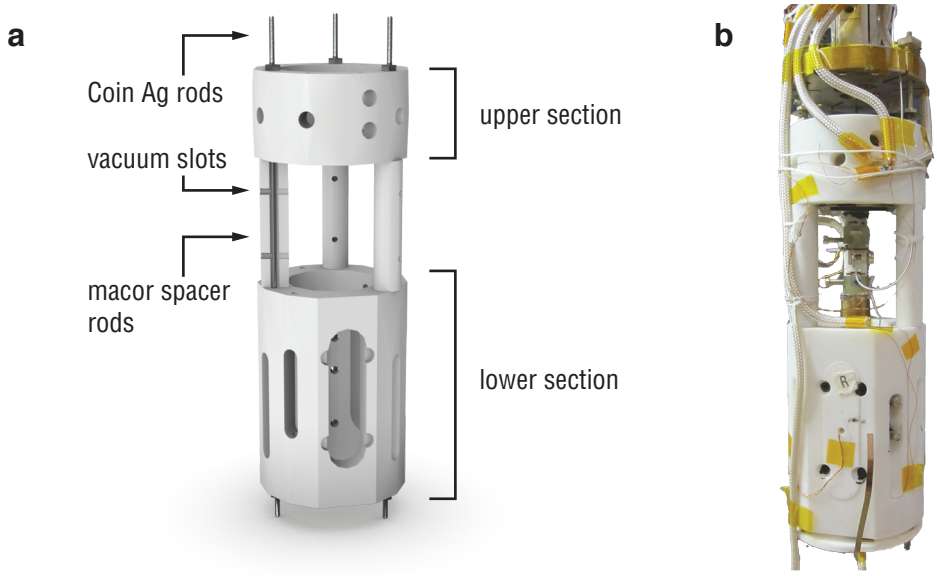

Figure 2.2: **a**: Model of the macor body of the microscope and **b**: photo of the microscope shortly before a cool-down.

The body was constructed in two parts, an upper section that houses either the tip or the sample and x-y coarse positioning motors, and a lower section containing the scanning assembly. Based on a modular design, the two sections can be separated from each other, allowing for easy access to their respective components. As the mechanical rigidity of the microscope directly affects the stability of measurements, it is crucial that the two sections are well affixed to each other. To accomplish this, three coin silver threaded rods are fed through the whole unit and tied down with coin silver nuts as shown. Figure 2.2**a** shows the macor body of the microscope along with the coin silver hardware.

The upper section contains six piezoelectric actuators that can translate the sample in the *x-y* plane over a square distance of about 1 cm. The motors were fabricated using stacks of polarized piezoceramic materials which are driven in unison resulting in the translation of a thin sapphire disc. The lower section contains a similar motor assembly for coarse manipulation of the scanning unit in the *z* axis. Six piezo-stacks grip the sapphire prism containing the scan piezo on its three faces. More details regarding these motors can be found in section 2.2.

Scanner Assembly

The scanner assembly is the solution to the following problem: how can we move the force sensor to a large number of points in a rectangular grid as quickly as possible, with the desired level of resolution ($\sim$ 1 nm in this case). Many choices regarding the scanner assembly can influence the possible rates of acquisition of the instrument. Since the beginning of scanned probe microscopy, several different solutions to this engineering problem have been identified, each with its own set of advantages and compromises. Nearly all rely on the piezoelectric properties of certain materials.

The earliest probe microscopes used a tripod arrangement of piezo actuators (see figure 2.3**a**), in which three separate stacks were responsible for creating motion in the three orthogonal axis: x, y, and z.[2] However, such designs would need to be quite large to allow for reasonable scan ranges, and were therefore not considered for this microscope. Slip-stick motors have also been used to move the scanning stage, but are generally unable to perform well at the nanometer scale. [71]

The most common design for a scanner uses a tube piezo, capable of bending in two dimensions as well as extending or contracting along the axial direction. Despite several limitations of the tube piezo scheme, it still affords the best means of nano-positioning in three axes given all the restrictions of the low temperature AFM.

The standard piezo tube consists of a hollow cylinder with 5 electrodes: 4 on the external surface defining the 4 axis of bending, and one on the inside, as shown in figure 2.4**b** and **c**. The dimensions and piezoelectric constants of the tube will dictate the maximum scan range

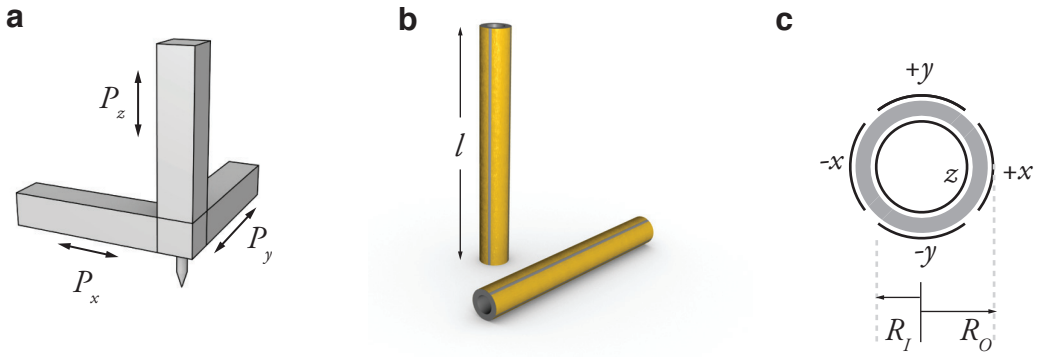

Figure 2.3: **a**: The tripod type scanner, **b**: A standard piezoelectric tube used for SPM scanners and **c**: an axial view of the tube showing the quartered electrode configuration.

possible, a factor which impacts the usability of the instrument, especially at low temperatures where piezoelectric coefficients of the lead zirconate titanate material (PZT) can decrease by a factor of 5.[3] Additionally, the geometry of the tube will also influence the internal resonance of the scanner, a parameter which is also important and will be discussed below.

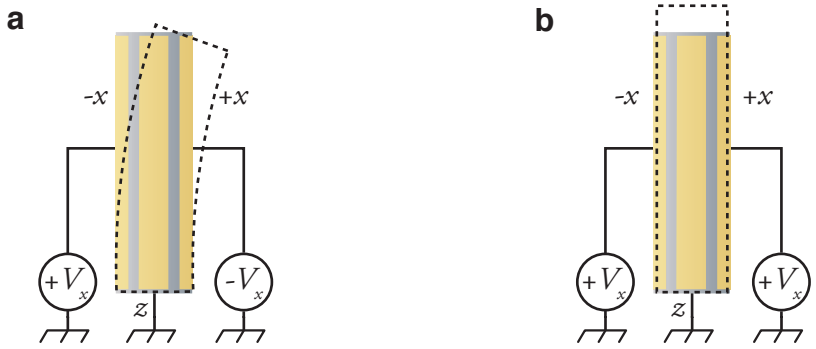

Figure 2.4: **a**: Diagram indicating the bending motion accomplished by application of opposite voltages to opposing electrodes. The center electrode, z, is considered the reference for the bending mode. **b**: The scheme for creating axial extension or contraction of the tube.

Considering the basic analysis of the bending beam, to be discussed further in the context of the force sensing cantilever in section 2.3, we can induce a bending distortion in the tube by compressing one side while extending the opposite side of the tube, as shown in figure 2.4**a**. In general, opposite voltages are applied to the outer electrodes to accomplish this. Similarly, the extension and contraction distortion is created by applying a potential difference between the inner electrode and the outer electrodes, as shown in figure 2.4**b**. Such distortions are used to generate the raster scan pattern, as well as to position the tip vertically.

A primary consideration regarding the mechanics of the scanner concerns the mechanical resonance of the unit. We can perform a quick measurement to assess the resonant properties of the tube.[72] By exciting one of the outer electrodes over a range of frequencies, and monitoring the induced voltage on the opposite electrodes, we can obtain a transfer function for the tube. Such a plot is shown in figure 2.5. From the amplitude and phase response, the first resonance is found to be at 860 Hz. Since the sawtooth wave used to generate the fast scan axis motion will contain harmonics higher than the actual scan rate (figure 2.6**b**), it's possible that these harmonics may induce unwanted oscillations at these resonance points.[4] Thus, the scan rates are usually limited to frequencies less than 1% of the lowest resonance peak,[73] other-

[3] Appendix A contains more details of the piezoelectric material used in this microscope.
[4] Also, a low resonance frequency invites external vibrations into the temple of the scanner assembly.

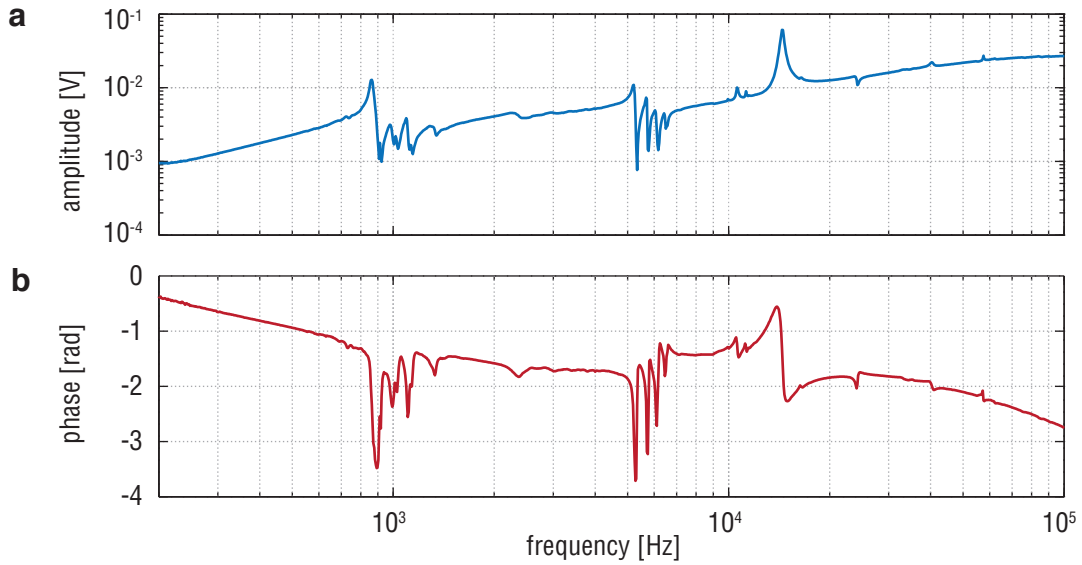

Figure 2.5: Resonances of the piezotube. By applying an ac excitation signal of 100 mV between the +X and the Z electrodes, the tube will bend. The bending will also induce, piezoelectrically, a voltage between the -X and Z electrodes corresponding to the amplitude of the displacement.

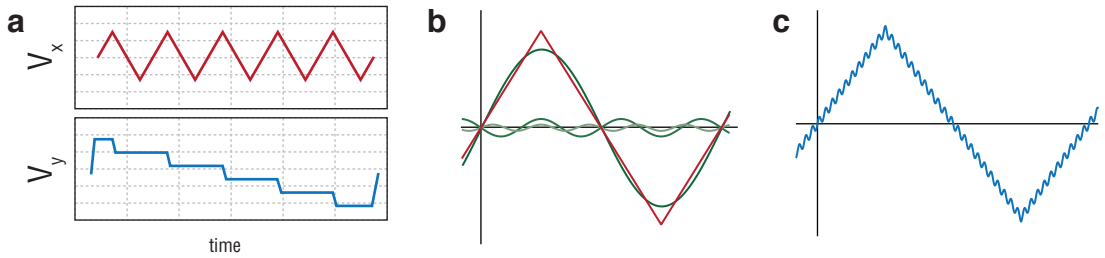

Figure 2.6: Generalized plots of the scanning waveforms. **a**: Fast and slow scan qualitative signals. **b**: Superposition of sinusoidal signals creating a triangle wave. **c**: Distorted triangle wave occurring when one harmonic (the 20th in this case) is multiplied, as would occur in a resonant structure such as the piezo tube.

wise, distortions to the tip position can lead to artifacts in the piezo response, as shown in the distorted triangle wave in figure 2.6c.

In designing the microscope, we must choose whether to scan the tip or the sample. That is, one of the two will remain stationary during data acquisition while the other will translate in space according the action of the scanner. Naturally, choosing one scheme over the other

is not a trivial determination as each option carries with it both advantages and disadvantages. The most obvious drawback from scanning the sample is the addition of mass to the end of the piezo tube. This results in a lower first resonance of the tube, thereby decreasing the maximum scan rate. More often, the tip assembly will have a smaller mass than the sample, making it more desirable to scan the tip rather than the sample. Figure 2.7 shows the decrease of the first resonance of the piezo tube upon application of mass to the free end. With the sample holder on the piezo, this peak descends to $\approx$ 500 Hz. It additionally becomes more jagged due to imperfect anchoring of the attached masses.

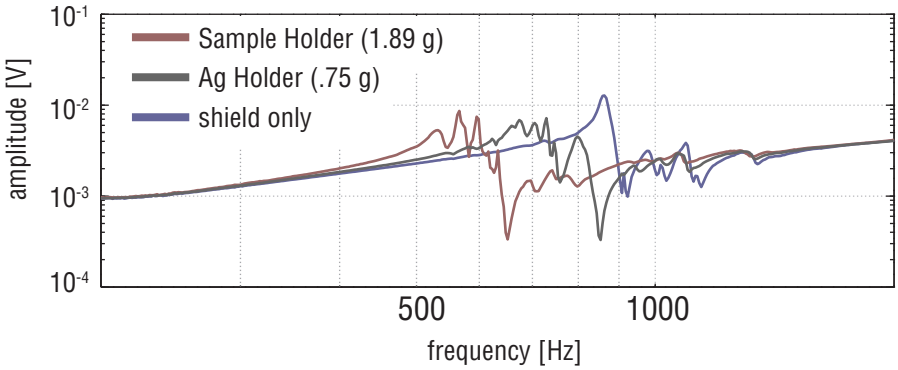

Figure 2.7: The resonant frequency of the piezotube with varying loads.

Since the tip assembly is generally less massive than the sample, scanning the tip will add less mass to the scan tube, however, other unexpected complications arise in this configuration as well. In the idealized case, the AFM cantilever represents a simple harmonic oscillator whose only interaction is with the sample. In the *real world* however, our cantilever is actually one tine of a quartz tuning fork, and is just one part of a complex system of coupled oscillators.[5] There are approximately 8 glue joints between the tip of the tungsten wire and the sapphire prism, each one represents an additional source of dissipative loss for the tuning fork/scanner assembly. Additionally, the state of the piezo tube itself was found to influence the dynamics of the tuning fork. For example, frequency shifts and damping changes were found to occur based on the extension and retraction of the piezo tube alone, independent of any tip-sample interactions.

Figure 2.8 shows the frequency response of the tuning fork when excited via a constant-amplitude ac excitation signal. The mechanical coupling between the tuning fork and the scanning structure is evident in the resonant frequency shifts of $\sim$ 1 Hz and fluctuations in the measured quality factors as different dc voltages are applied to the piezotube.[6]

[5]The quartz tuning fork as force sensor will be discussed in great detail in section 2.3

[6]Other measurements were also taken with the tuning fork in the exact same location, but mechanically decou-

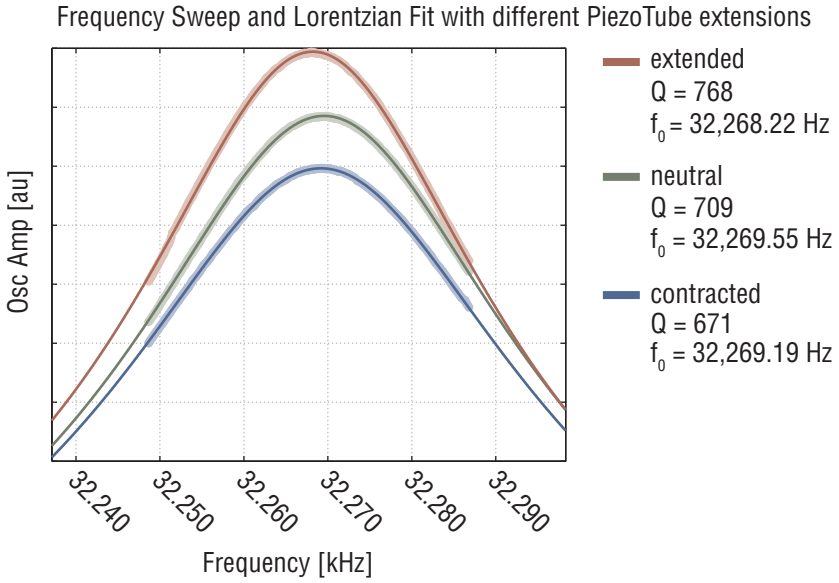

Figure 2.8: Frequency sweeps of a tip-less tuning fork in the qPlus configuration with different voltages on the piezotube. Both the resonant frequency and the quality factor are affected by the state of the piezo tube.

The effect is not only dependent on the vertical displacement of the piezotube, but can also be seen as a function of the x-y flexing of the scanner, as shown in the 2D scans in figure 2.9. This artifact adds unwanted complications to the data acquisition process.[74] Thus, in this instrument, scanning the sample, and keeping the tip structure stationary during acquisition seems to be a better arrangement, despite the lower resonance of the tube due to the additional mass loading of the sample.

Coarse Motors

Principle of operation

Early low temperature AFM/STM set ups lacked the ability for coarse translation of the sample, and scanner unit at base temperatures.[75] This meant that once the relative tip sample positions were set at room temperature, there would be no means of relocating to another position of interest, outside the limited range of the tube piezo, without warming the entire insert. Although it significantly increases the complexity of the instrument, the inclusion of coarse po-

pled from the piezotube in order to show that the effect was not caused by electrostatic fields from the high voltages ($\approx$ 200 V) on the tube. No correlations between the piezo voltage and tuning fork parameters were found in this configuration. This result also precludes the possibility that capacitive coupling between the high-voltage cables and the tuning fork wiring was to blame.

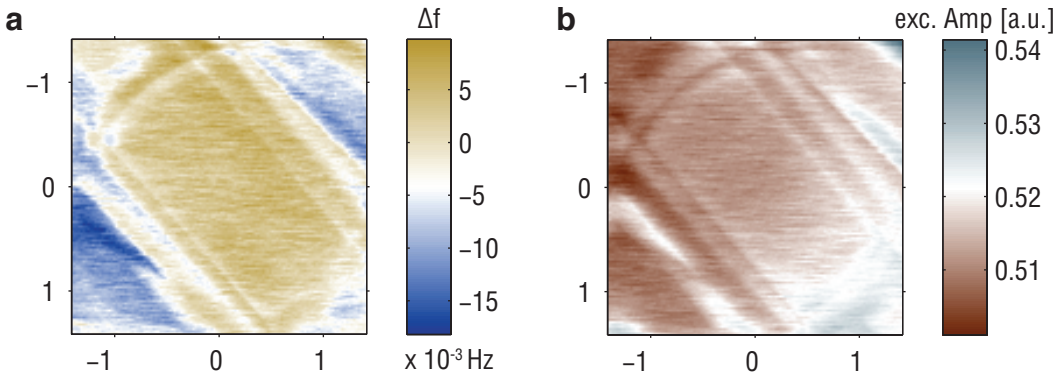

Figure 2.9: **a**: The frequency shift, Δf, of the tuning fork resonance based on the voltage on the piezo tube. **b**: Same scan but the excitation is now plotted. If there were no coupling between the tube and the tuning fork, these scans should be featureless.

sitioning at low temperatures was deemed a worthwhile investment for this microscope, since several days are required for a complete cooldown/warmup cycle.

Several designs exist for low-temperature, high-vacuum compatible x-y translation stages, most of which rely on slip-stick motion of piezoelectric actuators.[76, 77] Such systems are generally reliable, low-cost, and can be designed in a number of different geometries depending on the space and layout restrictions. The basic concept is as follows. A sharp, saw-tooth like voltage function is applied to opposite electrodes on a shear piezo unit. (Figure 2.10**b**) A shear piezo crystal will deform as shown in figure 2.10**c** upon the application of a potential (the polarization direction is labeled with a P). Shown in figure 2.10**a**, during the slow, rising section of the waveform, the mass m will translate along with the shearing face of the crystal, since the velocity is slow enough to not overcome the static friction. Then, the sharp decline of the waveform returns to the crystal to the undeformed state, this time at a velocity high enough to overcome the static friction, thereby sliding against the mass. The exact parameters of the waveform can vary for different systems. Suggested values for this system are given in Table 2.1. The plane of contact between the actuator and object undergoing translation is quite important. To ensure repeatable performance of the motors, both surfaces should be made of hard and smooth materials, such as Ruby or Sapphire.[54]

x-y Translation Stage

The above discussion accounts for motion in one dimension. However, for the sample stage, we required motion in both x and y. In a few other instruments, the x and y translation stages are decoupled and assembled in a vertical arrangement. However, due to space constraints,

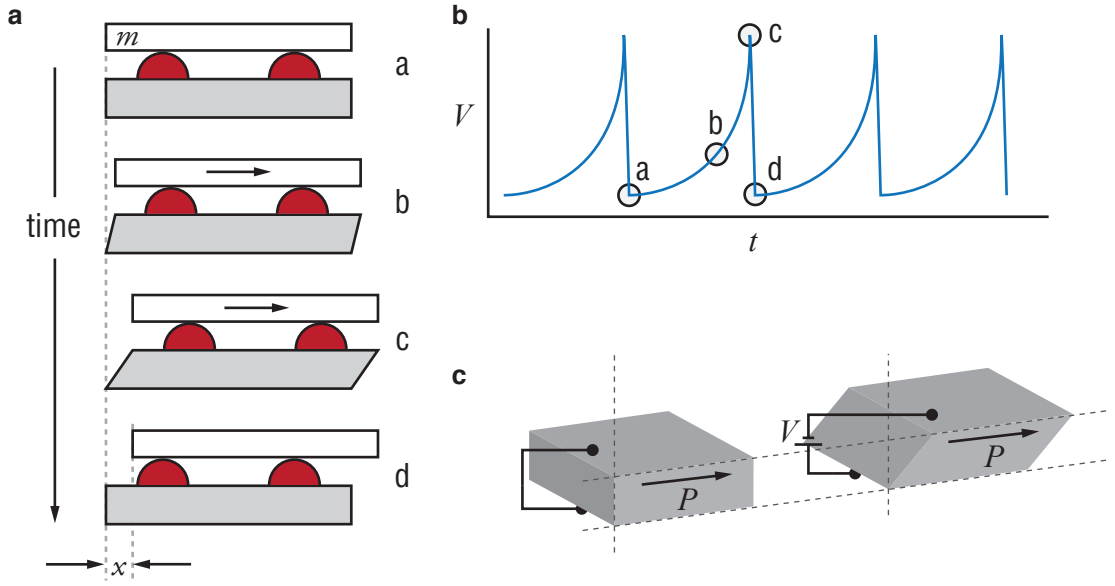

Figure 2.10: **a**: Diagram of a mass m being moved a distance x as a result of slip-stick action of a shear piezo element. **b**: Qualitative plot of the voltage on the actuator as a function of time. Corresponding positions are labeled. **c**: Mechanical deformation of a shear piezo upon application of a bias between the faces.

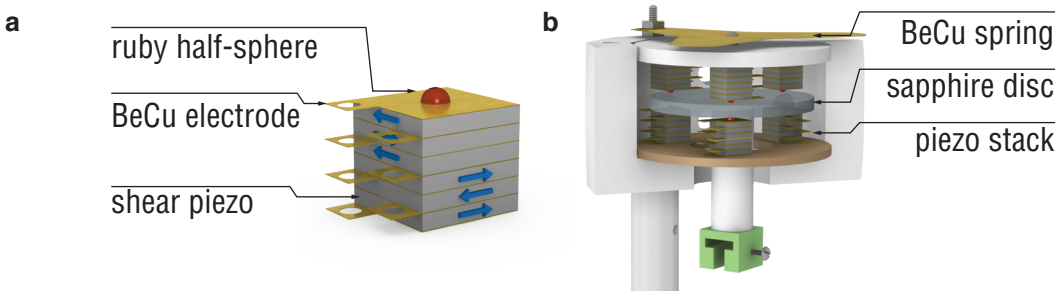

Figure 2.11: **a**: Example of a shear piezo stack orientated for x-y travel. Arrows indicate polarization direction of crystals. **b**: Upper section of AFM responsible for coarse motion in x and y.

the *x*-*y* stage for this microscope had to be designed in a different way. By stacking the piezo elements in such a way, with alternating directions of polarization, we can make vertical pillars which can bend along two orthogonal axes. If several of these stacks are situated in a horizontal plane, and an opposing set of stacks is placed in a mirror-like fashion above, with a smooth disc forming the boundary between the two sets, proper application of a coordinated driving signal to the stacks will result in translation of the disc. This arrangement is shown in figure 2.11**b**. The maximum travel range of this stage is approximately a 1 cm diameter circle.

The main drawback of this design is the possibility for non-orthogonal motion of the stage, meaning, the *x* and *y* axis are not rigidly defined by a constraint. This means that if the opposing sets of motors are not properly aligned, the resulting x and y translation axes might not be orthogonal. Additionally, the stage can also rotate, rather than simply translate in a straight line. However, these effects are generally small enough to not be a considerable burden while undergoing coarse motion. Figure 2.12 shows a collage of images at low T - high B demonstrating the effective action of the coarse motors.

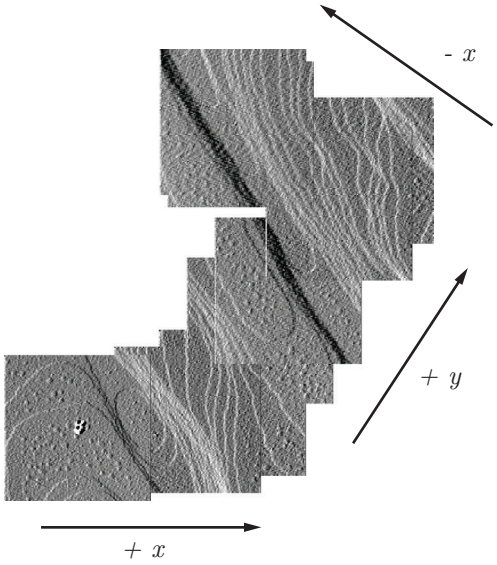

Figure 2.12: Collage showing several scans of KBr crystal terraces (3.3 Å high) taken at 4 T and 4.2 K showing the approximate orthogonality of the translation axis.

z Coarse Motor

A similar set of piezo actuators was designed for the coarse motion in the *z* direction. Such coarse motion is necessary for approaching the surface, as well as for distance dependent investigations that exceed the range of the scan tube. The motor is made by clamping the central

sapphire prism, which contains the scan tube, with 3 sets of piezo actuators, 2 permanently fixed in place, the third being spring loaded. In the z motors, the outer surface of the piezo stacks are Alumina (AlOx) plates. The range of travel for the z coarse motors is approximately 1 cm. Figure 2.13 contains 3D models of these motors and the scanner assembly.

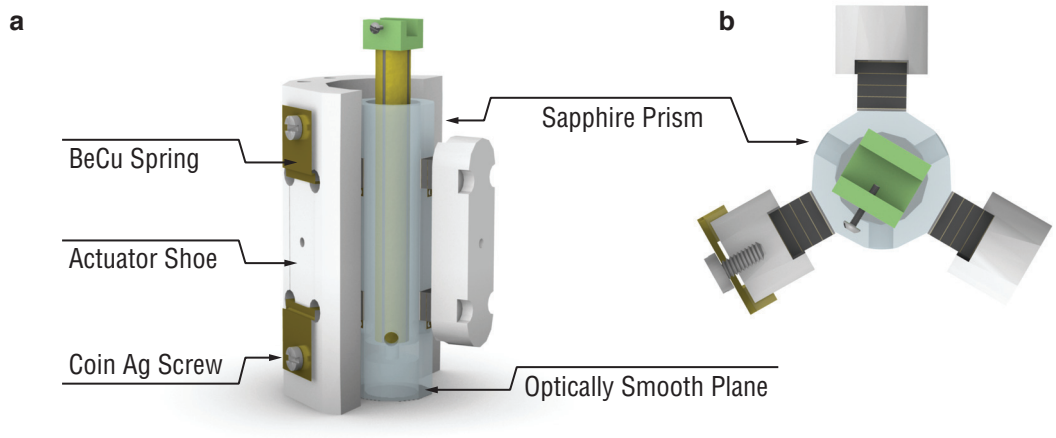

Figure 2.13: **a**: Side view of lower coarse motor section. **b**: Top view of same section, showing the three actuator assembly units situated 120° apart.

Operation Parameters

To generate the required signals, a HP function generator (FG) 33210a was programed with a point-by-point waveform, similar to that shown in figure 2.10**b**, the frequency and amplitude of which can be modulated by the user. The voltage signal from the FG is then fed to a custom step-up transformer which raises the voltage to levels large enough to induce motion ($\sim 300\times$). After the high-voltage (HV) transformer, a switch box was installed to enable convenient switching between the x, y, and z motors (The electrodes of the non-active motor are set to ground to avoid unwanted movement).

Capacitive Position Sensors

Naturally, during an SPM based experiment, the user would like to know where the sample and tip are located, relative to one another. Table top AFMs generally allow for optical access to the tip and sample, making this a trivial feat: just look. However, the low temperature system affords no possibility for visual inspection during operation. Just like a pilot on a cloudy day,

Axis	Temp	Amp (V_{pp}/300)	Freq (Hz)
x-y	Room	.5	300
	4K	2.5	301
z	Room	.8	1k
	4K	2.7	327

Table 2.1: Standard values for the voltage waveform at different temperatures.

the operator must *fly by instrument*. To monitor the coarse motion of the tip and sample, we have installed capacitive position sensors on the x-y stage and scanner assembly.

Principles of Operation

The position sensors rely on changes in capacitance, C, between two parallel plates due to their area of overlap.[78] Since, for an ac signal of frequency ω and voltage V, applied across a capacitor, the current, I, injected into the low side is

$$I = i\omega C V, \tag{2.1}$$

with the capacitance given by

$$C = \frac{\epsilon_0 A}{d}, \tag{2.2}$$

where A is the area of overlap (neglecting fringing effects), ϵ_0 is the electric permittivity of vacuum, and d is the separation, a measurement of the current will be dependent on the area of overlap. Figure 2.14 shows the geometry. Assuming reasonable values for A and d, we expect

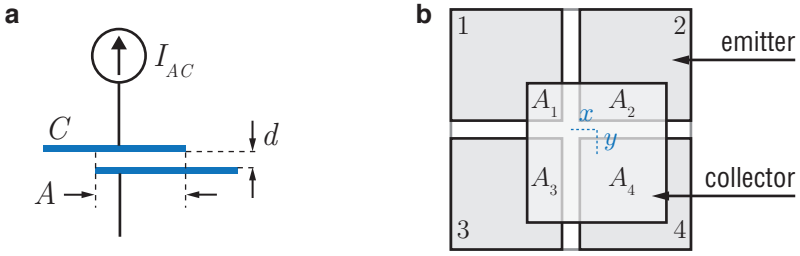

Figure 2.14: **a**: A simple capacitor model. **b**: Geometry of the bi-directional measurement scheme

capacitances in the order of picoFarads. This is the simple version. However, by measuring not only the amplitude of the current, but also the phase of the injected current, this model can be expanded to create a system sensitive to motion in two directions. Essentially, we divide

one side of the capacitor into four isolated units, each one with its own effective area of overlap with the other side of the capacitor. By applying phase shifted signals to each of the quadrants, then monitoring the phase information of the injected current, motion in one dimension can be detected independently from motion in the second dimension. This is expressed by considering the current due to one quadrant, j:

$$I_j = \frac{i\omega\epsilon_0 V_0 A_j e^{i\phi_j}}{d} \tag{2.3}$$

By selecting excitation phases $\pi/2$ apart, changes in the *in-phase* and *out-of-phase* components of the measured current will reflect motion in two orthogonal directions:

$$I = \mathcal{O}(x + iy), \tag{2.4}$$

where $\mathcal{O} = 2\sqrt{2}l\epsilon\omega_0 V_0/d$ is a constant given by the geometry of the capacitor and the frequency and amplitude of the excitation signal.[78] The relation of these axis to the geometry of the electrodes is given by the exact choices of the starting phase.

Implementation

Custom printed circuit boards (PCBs) were designed to create the variable capacitors. In the case of the *x*-*y* stage detectors, one section, the emitter array, was glued to the macor body. The other, the collector electrode, was glued to the macor post that is part of the moving stage. Since the resolution of the sensors is limited by the noise on the capacitive current measurement, the closer the two plates (smaller d), the higher the resolution for position measurements. Due to practical considerations,[7] a gap of 200 μm was chosen as for d (Careful glueing using glass slide cover slips as spacers helped maintain an equal spacing throughout the capacitor; any change in d over the span of the two planes will lead to non-linearities in the measurements). To simplify the required circuitry, the following excitation phases: $0, \pi/2, \pi, 3\pi/2$ were used for the four emitter electrodes.[8] Sine waves with frequency $f \approx 10$ kHz and amplitude $V_{\text{pp}} \approx 20$ V were generated by a custom made rack component. Using a lock-in amplifier with a reference phase set to 45°, we can easily measure the in-phase and out-of-phase components of the injected current.

Based on the geometry and parameters of the setup, a motion of 1μm will change the injected current by ≈ 300 pA. Such a change is well within the capabilities of the standard lock-in amplifier. The measured calibration for the sensors will change slightly due to temperature related geometry distortions. For example, the gap d could easily change by more than 10% due

[7] Smaller gaps make for larger currents, however, they also make for little crevices in which debris can get stuck.

[8] The original analysis in Eq. 2.4 is based on a starting phase of $-45°$. However, simply setting the lock-in reference phase to 45° will allow for the simply series of phases starting with 0°.

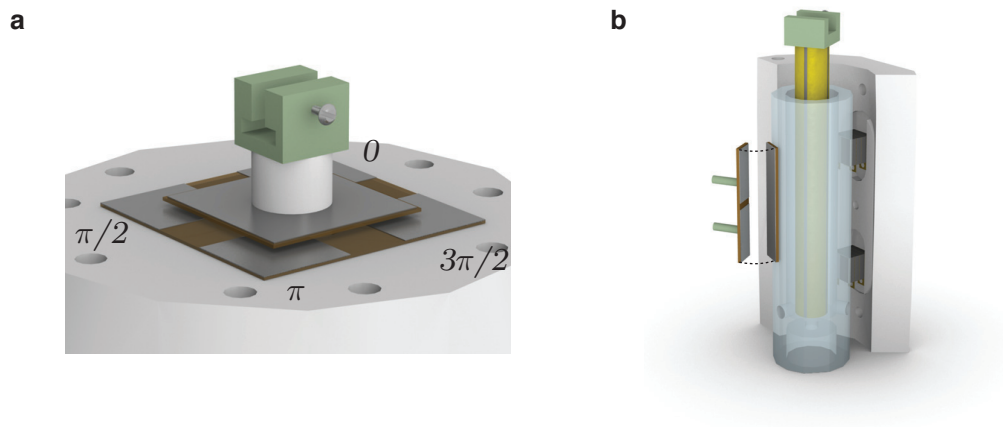

Figure 2.15: **a**: The x-y stage capacitive sensors and **b**: cutaway showing the z axis sensors.

to thermal contraction. At low temperatures we can calibrate the motion by using measured distances on a topography scan. In general, values of ≈ 500 pA/μm are obtained.

For the z direction sensor, we require only two of the four phases, since motion is only in one dimension. This simplifies the design and installation of the sensor. Again, PCBs were designed to fit in the tight spaces of the scanner area and fixed in place with epoxy. Similar values are obtained for the calibrations: at 4 K, we can expect 1 μm of motion to result in a ΔI of ≈ 40 pA.

Sample Holder

Another complication for the ULT-SPM originates in the cross-disciplinary nature of the experiment. Standard probe microscopy usually requires very few electrical contacts to the sample under investigation while low temperature experimental setups require many electrical contacts the sample. Allowing for many contacts is a straightforward task when the sample is stationary; however, mounting upwards of ten leads on a movable sample requires a little more consideration. To this end, we have designed a custom holder that allows for samples approximately 8 mm square, with 9+1 electrical contacts, the tenth contact being used as a ground plane underneath the entire sample. The holder uses a modular design featuring a removable platform to allow for easy exchange of samples. Also, the heat sinking of the sample is accomplished through the leads, which means that they must remain thermally conductive until they are anchored at the mixing chamber.

Care must be taken when mounting the sample to keep the leads away from the area of interest, as it is likely the tip could collide with one of them during the course motion or scanning. For most of the samples mounted, wire bonding using thin gold wire between defined

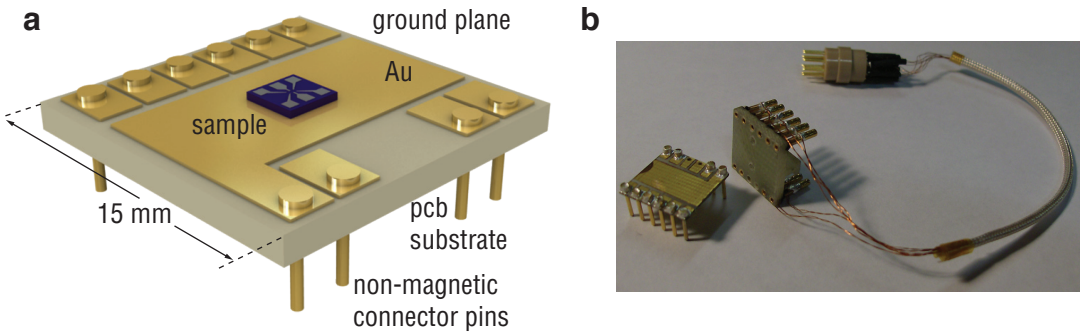

Figure 2.16: **a**: Model of the sample holder platform. Non-magnetic connectors are used to join the upper and lower sections. **b**: Photograph of the holder showing the leads.

pads on the sample surface and the gold surface of the sample platform suffices. Figure 2.16 shows the pcb component as well as a photograph of the entire sample holder.

2.3 Force Sensor - The Tuning Fork

Introduction to the Quartz Tuning Fork

The first documented use of a quartz body as an electronic frequency control dates back to 1920, when Walter Cady filed patents entitled Piezo Electric Resonator (1920) and Method of Maintaining Electric Currents of Constant Frequency (1921). Prior to these patents, the only proven application of quartz and piezoelectricity was as an ultrasonic generator for underwater echolocation, that is, SONAR. However, the qualitative similarity between the resonance peaks of a quartz crystal and the well known acoustic response of metal tuning forks, prompted Cady to apply the quartz crystal as a frequency control element. However, unlike the metal tuning fork, the quartz crystal could be used in frequency ranges much higher than the audible acoustic frequencies and the piezoelectric nature of the crystal made its integration into electronic circuitry almost trivial. Radio technology was just beginning to fill the air with megahertz transmissions and the need for high-frequency time standards was about to explode.

As electronic equipment decreased in size, loosening the shackles of vacuum tube infrastructures, and portability became desirable, the geometries of the standard quartz resonators were found to be unsuitable for the instabilities associated with mobile units. Thus, the quartz tuning fork was developed. The first reports from 1972 indicated that even after "the watch is dropped face downwards onto an oak plank" from a meter high, the observed frequency deviation $\Delta f/f$ is less than 0.2×10^{-6}.[79] Aging tests also showed an annual stability of $\pm 2 \times 10^{-6}$, making the common quartz wrist watch an exceedingly reliable time piece. The end result be-

ing that the use of quartz tuning forks became pervasive in modern electronics, thereby driving production rates up and costs down. Currently, quartz tuning forks generally cost less than 1$ and are available in a myriad of geometries and packaging configurations.

Electromechanics of the Tuning Fork

As we saw earlier in the introductory section, the heart of the AFM relies on the interaction between a sharp tip and the sample under investigation. A relevant question is therefore: how can we measure this interaction. Fortunately, the quartz tuning fork offers a convenient method. The standard approach for monitoring the interaction between the tip and sample involves attaching the tip to an oscillating beam, and detecting the modulations in the dynamics of the oscillator resulting from the tip-sample interactions. The piezoelectric properties of quartz tuning forks make this detection possible, if not straightforward. The measurable signal from the tuning fork is the current generated in proportion to its amplitude of oscillation. From this, we can obtain other quantities of interest, ie. resonant frequency and quality factor.

Let's consider a bending beam, anchored on one side. (See figure 2.17**a**) An elementary analysis of a bending beam begins by considering the deformation of the constituent materials upon application of an external force and the resulting stress.[80] Bending about the z axis will lead to a dilation above the center of the beam, the so called neutral axis, and a compression below, as seen in figure 2.17**b**. The strain, ϵ, on the bent body due to the change in length, l, can be found from the geometrical layout shown in figure 2.17**c**:

$$\epsilon = \frac{\Delta l}{l} = -\frac{dy}{ds} = -\frac{x d\phi}{R d\phi} = -\frac{x}{R}. \tag{2.5}$$

Since in the elastic regime, stress, σ, and strain are related in a linear fashion:

$$\sigma = \mathrm{E}\epsilon \tag{2.6}$$

where E is Young's Modulus. If we let the bending moment be defined by M:

$$M = \int_A x\sigma dA \tag{2.7}$$

and the moment of inertia, I, by:

$$I = \int_A x^2 dA, \tag{2.8}$$

we can combine equations 2.5 - 2.8 to arrive at:

$$\frac{1}{R} = \frac{M}{\mathrm{E}I}, \tag{2.9}$$

which will be useful in calculating the spring constant and resonant frequencies of a bending beam, or tuning fork (TF) tine in our case.

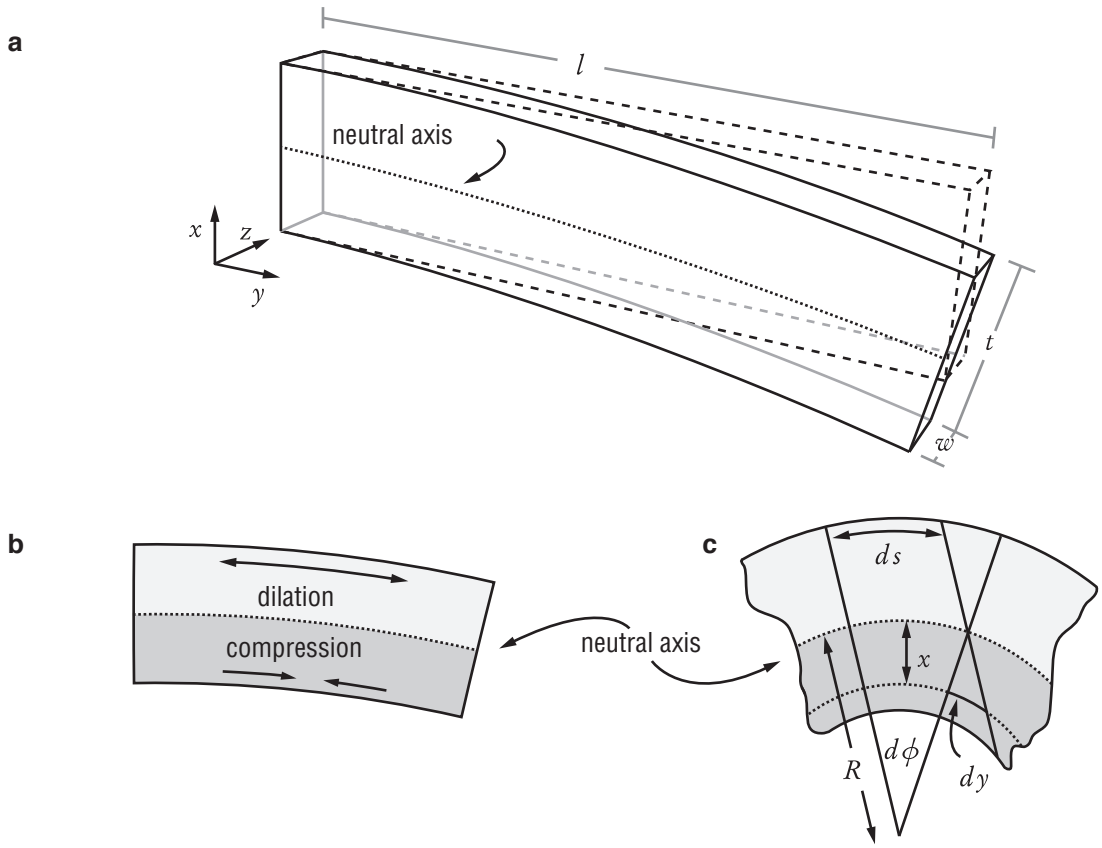

Figure 2.17: **a**: A bending beam showing the neutral axis. **b**: The two zones of dilation and compression. **c**: Elements for the calculus of bending beams.

Analytical Expectations

Spring Constant

The curvature of a 2D curve is found from geometrical analysis to be:

$$\varkappa = \frac{1}{R} = \frac{\frac{d^2x}{dy^2}}{\left[1+\left(\frac{dx}{dy}\right)^2\right]^{3/2}} \ . \tag{2.10}$$

Using the expression above, 2.9, and assuming a small angle of oscillation, (thus considering the denominator in 2.10 to be ~ 1) we arrive at:

$$\frac{d^2x}{dy^2} = \frac{M}{\mathrm{E}I} \, . \tag{2.11}$$

Since the torque, τ, on a lever from a force, F, applied at position a is given by:

$$\tau = F\,(y - a)\,, \tag{2.12}$$

and is equated with the bending moment which appears in equation 2.11, we can obtain the equations of motion for the TF by integration:

$$x = \frac{Fy^2}{6\mathrm{E}I}\,(y - 3a)\,. \tag{2.13}$$

If the point of applied force is at the far end of the level, making $y = a = l$, we obtain:

$$x = -\frac{l^3}{3\mathrm{E}I}F\,. \tag{2.14}$$

This is nothing more than Hooke's law with a spring constant k given by,

$$k = 3\frac{\mathrm{E}I}{l^3} = \frac{Ew}{4}\left(\frac{t}{l}\right)^3\,, \tag{2.15}$$

where the moment of inertia is given by $I = wt^3/12$. Using the measured values for the geometry of the TF and the Young's Modulus of quartz (78.7 GPa), we can expect a spring constant of ~ 1919 N/m. The spring constant is an important figure of merit for the TF force sensor, as it has deep implications regarding the achievable sensitivities, as will be discussed below.

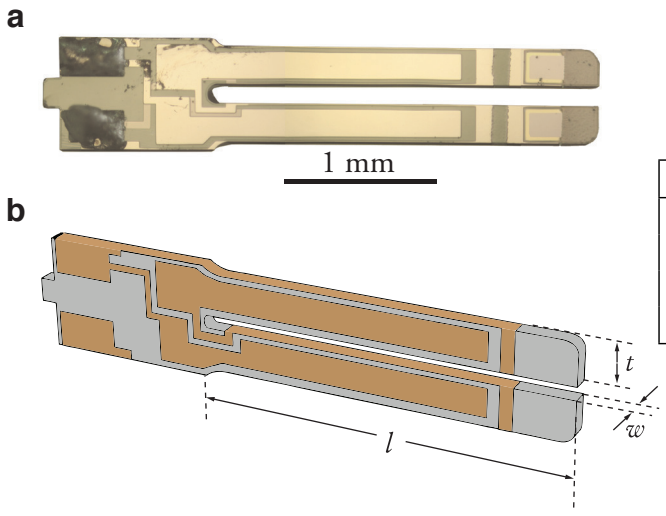

Tuning Fork Geometry	
t	242 μm
w	100 μm
l	2.44 mm
E	78.7 GPa

Figure 2.18: **a**: Photo of a standard quartz tuning fork removed from the packaging. **b**: The tuning fork geometry and important specifications.

Resonant Frequency

Other easily calculated parameters of the oscillating beam are the eigenvalues of its oscillation modes.

The equation of motion for an oscillating beam, of density ρ with cross-sectional area A, can be given by: [80]

$$EI\frac{d^4x(y,t)}{dy^4} = -\rho A\frac{d^2x(y,t)}{dt^2}\,, \tag{2.16}$$

which can be made easier to deal with if $x(y,t) = x(y)\cos(\omega t + a)$:

$$EI\frac{d^4x(y)}{dy^4} = \rho A\omega^2 x(y)\,. \tag{2.17}$$

If

$$\kappa_n^4 = \frac{\omega_n^2 \rho A}{\mathrm{E}I}\,, \tag{2.18}$$

we arrive at a standard differential equation:

$$\frac{d^4x(y)}{dy^4} = \kappa^4 x\,. \tag{2.19}$$

Considering the boundary conditions of beam clamped at one end, and solving, we obtain the following:

$$\cos(\kappa l)\cosh(\kappa l) + 1 = 0\,. \tag{2.20}$$

The first three roots of which are found to be:

$$\kappa_n l = 1.875, 4.694, 7.855 = r_n\,. \tag{2.21}$$

Thus, from 2.18, and $\omega = 2\pi f$, the resonant frequencies of the oscillating beam are:

$$f_n = \frac{r_n^2}{2\pi l^2}\sqrt{\frac{I\mathrm{E}}{\rho A}}\,. \tag{2.22}$$

Using the density of quartz, $\rho = 2650$ kg/m^3, and the values from figure 2.18, we can predict a fundamental resonant frequency for the tuning fork of $\sim$35 kHz. The actual f_0 of the standard tuning fork is designed to be $2^{15} = 32.768$ kHz; during the manufacturing process, laser trimming is employed to guarantee this value.

Piezoelectric effect in Tuning forks

It was shown above how the oscillations of the tuning fork tine can be expressed in terms of stress and strain. Since the piezoelectric framework is also expressed in the same terms, a quick correlation between the beam dynamics and the induced piezoelectric signals will be helpful.

The piezoelectric constant, d_{ij} describes the ratio of the strain in the j-axis to the electric field applied along the i-axis, if all external stresses are held constant.[9] From the symmetries of the α-quartz crystal, this piezoelectric constant is reduced to two independent values[81]:

$$d_{11} = -d_{12} = d_{26}/2 \text{ and } d_{14} = -d_{25} \,. \tag{2.23}$$

(Here, the subscripts are defined as $\hat{x},\hat{y},\hat{z} \Rightarrow$ 1,2,3 and shear around $\hat{x},\hat{y},\hat{z} \Rightarrow$ 4,5,6.)

Quartz tuning forks are fabricated from a specific *cut* of the quartz crystal, indicated in figure 2.19.[10] Based on the geometry of the bending beam shown in figure 2.17, internal strains

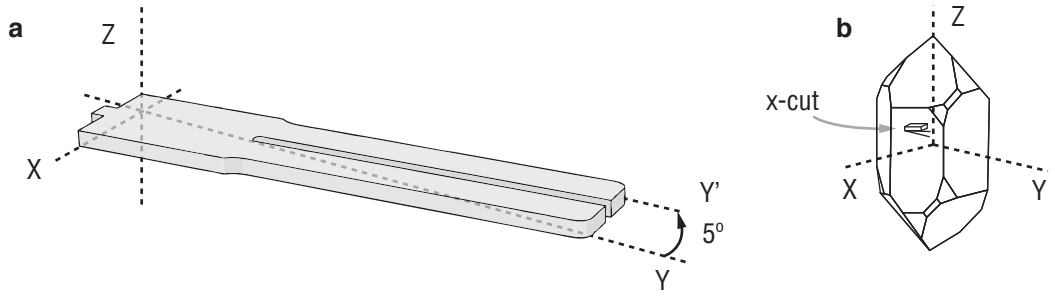

Figure 2.19: **a** :The relation between the quartz tuning fork and the crystal axes and **b**: The position of the x-cut within the bulk quartz crystal

in the +/- y direction are required to generate motion in the x axis. From the electrode configuration shown in figure 2.20**a**, we can model the internal electric fields of the tuning fork arm when the upper and side electrodes are electrically isolated from each other. The dominant field vectors are shown to be in the +/- x direction. From the piezoelectric constants, we can see that a field in the x direction will lead to strains in the y axis, the direction of which will switch based on which side of the neutral axis we are considering. These anti-parallel strains result in the flexing of the beam in the desired mode, as seen in figure 2.20**c**. Conversely, strains in y due to bending, lead to potential differences between the electrodes. Thus, the tuning fork is both sensor and actuator simultaneously. This captures the essential piezoelectric nature of the quartz tuning fork; more details regarding the piezoelectric effect can found in Appendix A.

[9] Appendix A contains more on piezoelectric principles.

[10] This cut was chosen by the time-keeping industry due to the flat temperature dependence of x-cut quartz at and around room temperatures.

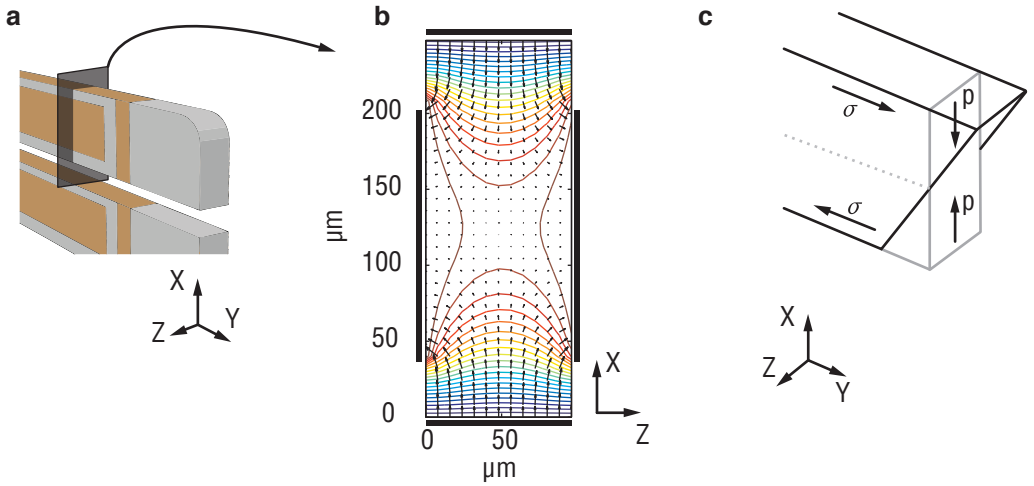

Figure 2.20: **a**: The electrode configuration on the upper tine of the tuning fork. **b**: Electric field lines and potentials inside the quartz tine as calculated from electrostatics. **c**: Schematic showing the internal strains of the tuning fork tine.

qPlus

The above analysis is based on a single oscillating beam. However, the quartz tuning fork is clearly a system comprised of two such oscillating beams. Additionally, we focused on one particular eigenmode of the structure, when in reality, an oscillating beam can have many different modes of vibration: flexural, torsional, longitudinal etc. The tuning fork geometry, i.e. two coupled beams, adds additional complications since the two tines may oscillate symmetrically or asymmetrically. To avoid these complications, the tuning fork electrodes are usually arranged in such a manner as to detect only oscillations of a particular mode, usually the symmetric mode shown in figure 2.21. Oscillations in this mode demand no motion of the center of mass of the fork, and thus generally have the highest quality factors, another critical parameter describing the TF. However, this advantage of the tuning fork is quickly negated when for whatever reason, the tines become asymmetric in some manner. Also, with two unequal coupled oscillators, the standard electrode configuration will no longer suffice for eliminating signals from unwanted eigenmodes. In the case of the probe microscope, an asymmetry is created as soon a tip is attached to one of the tines, creating an additional mass. One approach to circumventing this problem involves counterbalancing the tip-less tine with an equal mass. [82] Threefold improvements in quality factor have been demonstrated by carefully balancing the tines; however, this presents a drastic complication to the already difficult process of adding a tip to a TF tine. Alternatively, Rychen et al. have used very thin wires as tips in order to reduce

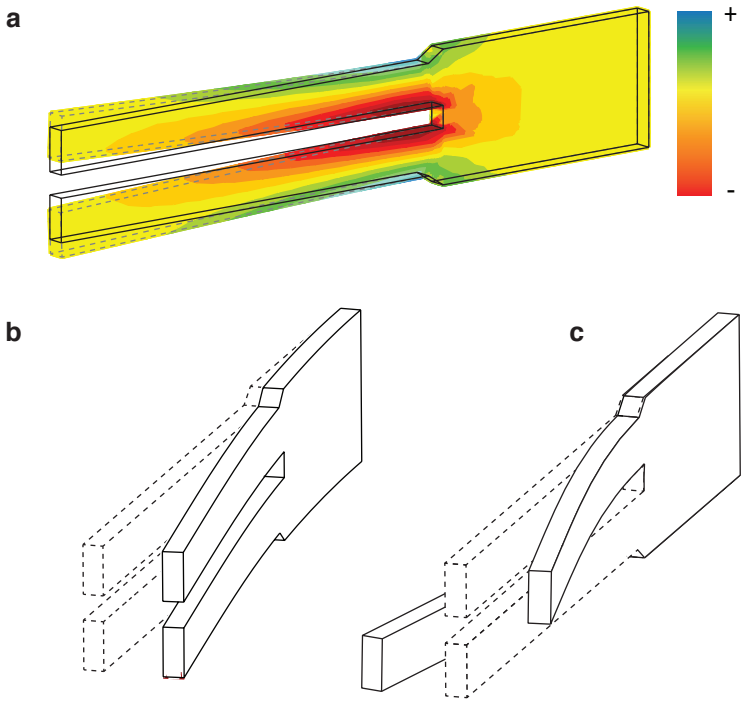

Figure 2.21: Oscillation modes of a quartz tuning fork: **a**: The symmetric mode generally used by the quartz tuning fork in many applications. The color bar shows the position of maximum strain in the material. **b** and **c**: two other modes ($f_0 = 6$ and 11 kHz respectively) which are undesirable in the current SPM application. (Simulations performed by ProMechanica)

the added mass on the tine to a negligible amount.[47] In this case, the tip wire is exceedingly small in diameter, adding additional hurdles during the construction phase.

Another solution was presented by Giessbl in 1998,[83], now known as the qPlus sensor. By clamping the tine without the tip to a firm base, the oscillating system becomes simpler: it is essentially a single quartz beam. Although, a stationary center of mass is sacrificed, quality factors of the qPlus sensor are still significantly high, especially at low temperatures. The qPlus sensor was chosen for this microscope since it was deemed most compatible with all the requirements of the instrument. See Appendix C.1 for details regarding the construction of a qPlus sensor.

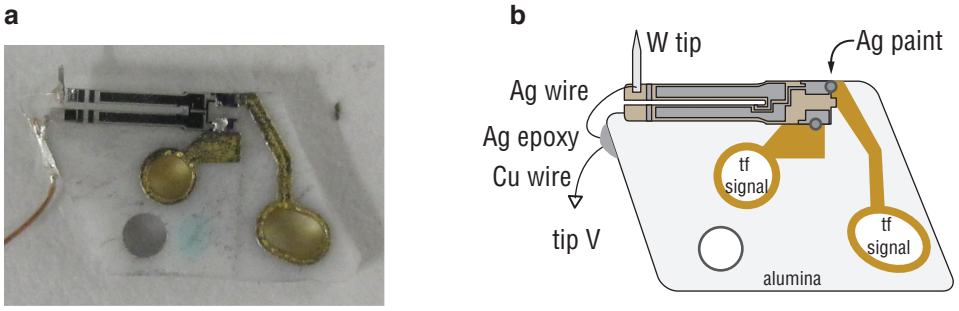

Figure 2.22: **a**: A photo of tuning fork shown with tungsten tip attached and the silver tip wire in place on an alumina substrate. **b**: Schematic representation of the same showing the important joints and electrical connections.

Tip Etching

Introduction to tip etching

Standard AFM tips are comprised of microfabricated Si cantilevers, with etched tip structures at the free end. While entirely suitable for most AFM applications, difficulties emerged when attempting to use such tips for low temperature systems. In particular, making electrical contact to a Si cantilever was found to add unwanted complications to the set up. Thus, a custom tip fabrication process was developed for the ULT-SPM experiment.

Since many potential experiments involve biases between the tip and the sample, the tips used should be electrically conductive. Doped Si cantilevers, while conductive at room temperatures, become insulating at low temperatures, and must therefore be coated with a thin film of a conducting metal such as gold. However, the problem remains of how to electrically contact the tip after it is installed on the tuning fork. Our initial procedures relied on attaching one of these coated cantilevers to the tuning fork.[84] This method was later exchanged for a more reliable and cost effective operation involving standard electrochemical etching of tungsten wire.

The etching of tungsten wire to create nanoscale sharp tips has been used since the early efforts in scanned probe microscopy.[85] Many researchers have elaborated on the procedures, however, they usually rely on the same principles. The tungsten wire to be etched serves as one electrode in an electrochemical cell. Applying a potential between this wire and another counter electrode leads to etching of the wire. At a critical point, the lower section of the wire falls and the current is cut-off via a control circuit.

Since the goal of the ULT-SPM project is not focused on ultra high resolution topography images, we are not so concerned with obtaining the sharpest tips possible. Instead, reproducibility of the etching process is more relevant. Since preparing a tuning fork and tip unit requires

many hours of time, and the final stage is the etching process, it is beneficial to have a reliable method for etching. To this end, we have developed our own procedure based on the principles mentioned above. If carried out properly, the yield of usable tips is quite high (≈ 75 %).

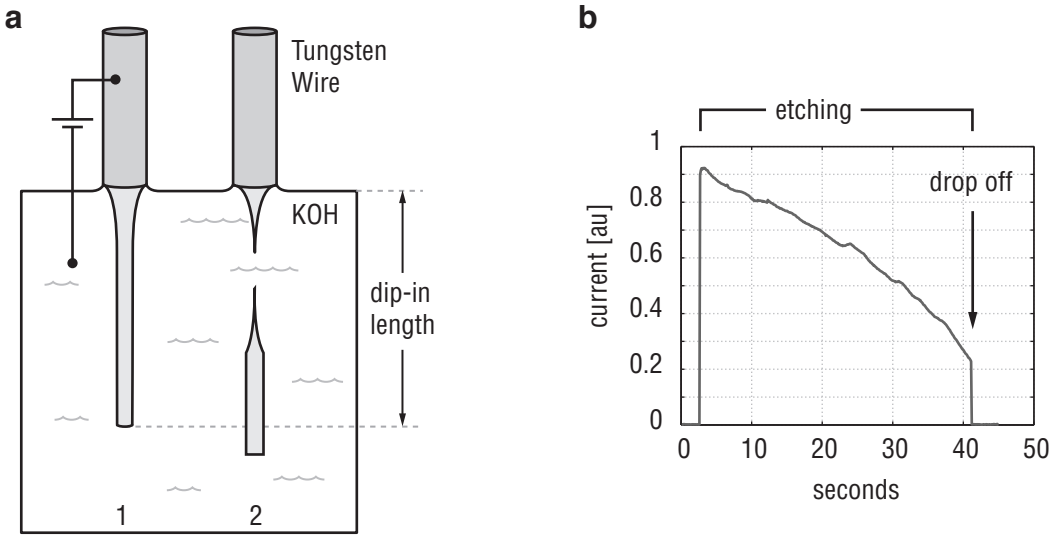

Figure 2.23: **a**: Schematic of tip etching principle: Phase 1 shows the constant etching of the cylinder until phase 2, when the weight of the lower section is heavy enough to cause it to separate from the upper section, forming a sharp tip. **b**: A plot of the current decay during the etching process showing a smooth decline followed by a rapid cut off when the current is ceased.

ULT-SPM tip etching parameters

In general, we follow the procedure laid out by Hagedorn et al.[86] However, we have adjusted a few parameters to suit the specific needs of the qPlus sensor. Notably, during the fabrication process of the sensor, the epoxy used to mount the tungsten wire to the tuning fork was found to migrate from the area of the joint, onto the shaft of the tip, most likely due to capillary forces. This wayward epoxy can complicate the etching process, leaving contaminations near the sensitive meniscus region of the bath. It may also form a transparent straw-like wrapper around the tungsten, usually resulting in a malformed tip and a wasted sensor. Thus, a thorough pre-etch step wherein the tip is uniformly etched for a short while until a fresh tungsten surface becomes exposed is necessary to ensure stable etching.

Usually, the success of the tip etching can be observed in the current plots recorded during the etching process, as shown in figure 2.23**b**. Qualitatively, there should be a smooth, gradual decline of the current as the surface area of the submerged tungsten diminishes. This decline is

Table 2.2: Standard etching parameters

KOH concentration	8.33 M
dip-in length	3 mm
approx. etching time	1 minute

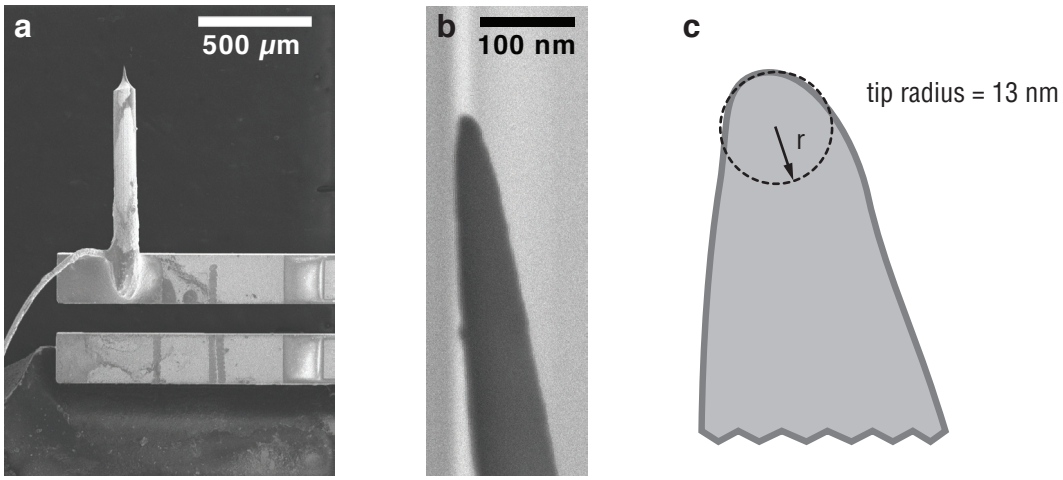

Figure 2.24: **a**: Scanning electron microscope image of an etched tungsten tip glued to the free tine of a tuning fork. The silver wire electrically connected to the tip is also visible. **b**: A close up of the tip used to measure the approximate tip radius as shown in **c**.

terminated by a sharp drop when the drop-off phase is reached. However, it is still necessary to examine the etched tips in a scanning electron microscope to verify the successful formation of a tip, and to measure an approximate tip radius. Such images and measurements are shown in figure 2.24.

2.4 AFM - electronics

Introduction to AFM electronics

From the previous discussions regarding the oscillations of a cantilever as it interacts locally with a sample, it is clear that the performance and abilities of the instrument depend significantly on our ability to accurately measure the dynamics of those oscillations. Thus, careful attention should be paid to exactly how the oscillations of the little quartz tuning fork become the pixels of varying shades in a standard AFM image.

Since the first AFM that used the distance dependent tunneling signal between the force

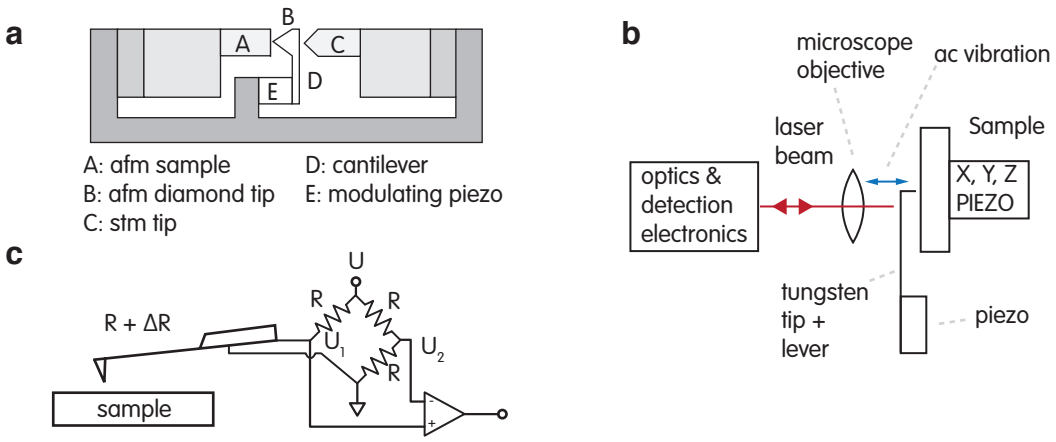

Figure 2.25: **a**: The original detection scheme involving both the force sensor and the tunneling detector which used the distance dependent tunneling to monitor the position of the foil beam (after [3]). **b**: Interferometer setup (after [7]). **c**: The first piezoresistive cantilever as force detector. Difficulty obtaining the sensors has made their use inconvenient (after [87]).

sensing cantilever and a nearby tunneling microscope probe,[3] many advances have been made in the detection schemes. Notably, laser detection schemes have become the most common means for measuring the deflection of a cantilever. Using interferometric techniques, very accurate position sensing can be achieved with the laser schemes. Cantilevers made from piezoresistive materials have also been used in low temperature AFMs.[87] Sensitive resistance bridges are used to monitor changes in resistance due to cantilever stresses. Figure 2.25 recreates some of the original schematics for these designs. However, such methods were not considered for this microscope due to either restrictions regarding light sensitive samples or the larger power dissipation known to occur in piezoresistive cantilevers. Instead, we can rely on the piezoelectric effects of the quartz tuning fork to monitor the dynamics.

As noted during the discussion on the force affecting the cantilever, the quantities of interest in the tuning fork are its oscillation amplitude and resonant frequency. Changes in these two parameters are indicative of tip-sample interactions. Fortunately for the field of probe microscopy, the telecommunications industry is also interested in tracking the modulations of ac signals, and has therefore developed many relevant tools and methods.

In addition to measuring the cantilever dynamics, the AFM must respond to the dynamics, i.e. feedback schemes are integral components. High voltage signals need to be generated and applied to the scanner assembly, while recording in a usable format the data collected from the microscope. This is the role of the AFM controller unit. Thus, there are two connected yet distinct electronic components needed to operate this microscope. Both will be discussed in

this section.

Cantilever Excitation

Prior to measuring the oscillator, it first needs to be oscillating. While thermal oscillations will always be present, their amplitudes are too small to be useful for this work. The cantilever therefore needs to be excited by an external source. Additionally, the excitation signal becomes an integral part of the feedback mechanism described below.

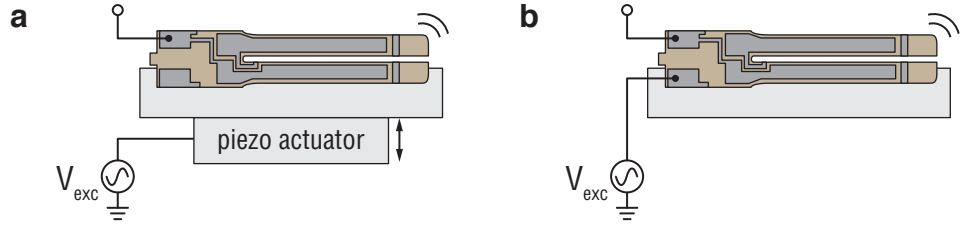

Figure 2.26: The two standard methods for exciting a cantilever: **a**: mechanical excitation wherein the tuning fork is excited via the vibrations of its base, either through the piezo tube, or a secondary dither piezo and **b**: electrical excitation using an ac signal applied directly to one electrode of the tuning fork.

At the most basic level, there are two means available for exciting a quartz tuning fork: mechanical and electrical, portrayed schematically in figure 2.26. Mechanical excitation involves shaking the whole tuning fork via an ac signal applied to nearby piezo actuator. Electrical excitation requires a similar ac signal to be fed to the electrodes of the tuning fork and inducing motion via the converse piezoelectric effect. The mechanical method is more straightforward from an electronics standpoint, while the electrical excitation simplifies the construction of the sensor.

Electrical Excitation

Either way, the signal used to excite the tuning fork is generated by the control instrumentation. However, for the electrical excitation method, complications arise due to the capacitance of the cabling and the resonator. Considering the equivalent circuit of a quartz resonator[88], [89], as shown in figure 2.27, it is clear that a time varying voltage applied to the input node will result in a capacitive current contribution to the total current:

$$I_{\text{total}} = I_{\text{mechanical}} + I_{\text{capacitive}}, \tag{2.24}$$

due to the parasitic capacitance of the electrodes of the tuning fork. This results in asymmetric resonance peaks and errors in the phase. However, such effects can be negated by including a compensation scheme in the detection electronics.

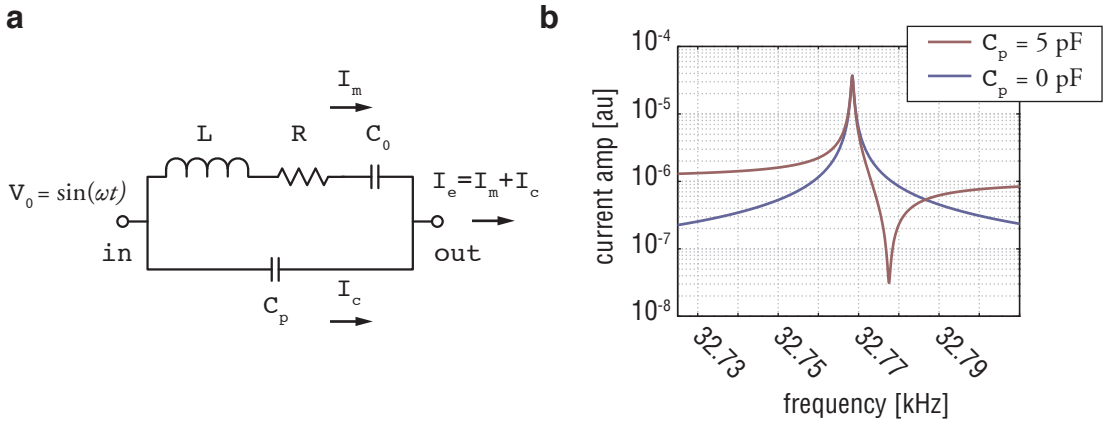

Figure 2.27: **a**: The tuning fork equivalent circuit and **b**: modeled admittance of the circuit showing the effects of the shunt capacitance.

The basic compensation scheme is shown in figure 2.28. Essentially, the excitation signal is inverted using an inverting amplifier, then added to the current generated from the tuning fork. Careful adjustment of the gain of the compensation stage enables cancellation of the capacitively generated current from the quartz crystal resonator. Using an inverting op-amp allows for a more compact electronics package as opposed to a transformer based system as used in other systems.[90]

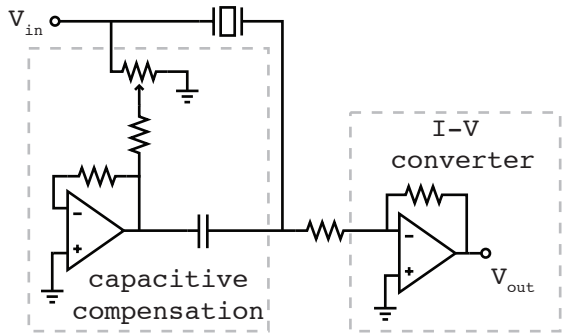

Figure 2.28: Schematic for the capacitive compensation scheme.

Mechanical Excitation

Mechanical excitation can be achieved quite easily by adding an ac component to the piezotube Z voltage. A simple rackmount summation box is used to add the signals. Approximately 10 mV applied to the piezotube is enough to significantly excite the tuning fork; this corresponds to about a 90 pm extension variation, small enough to be lower than the noise floor during most modes of operation and well above the cutoff frequency of the feedback loops. However, as noted earlier, we have found more reliable operation with the force sensor not mounted on the scan tube. Thus, our latest qPlus sensor mount has a small piezo actuator built into it which serves to excite the tuning fork.

Tuning Fork Signal Measurement

As seen in the discussion above, section 2.3, the oscillations of the tuning fork will lead to a piezoelectrically induced current. For many modes of operation, this current serves as the input signal for the control electronics. On its own, however, the tuning fork can only generate small signals which must be amplified to a more manageable level to be used by the feedback loops. For example, a 1 nm oscillation amplitude will result in a current of ∼80 pA. Such a signal, while measurable, is not an ideal input source. Therefore, we have developed custom electronics to deal with the tuning fork signal.

I-V converter

The most basic module is a standard current to voltage (I-V) converter (Figure 2.29**a**). A standard transimpedance amplifier in the inverting configuration will provide a voltage output, V_{out} based on the input current, I_{in} and the gain determined by the feedback resistor, R_{fb},

$$\frac{V_{\text{out}}}{I_{\text{in}}} = R_{\text{fb}} \tag{2.25}$$

Choosing an appropriate op-amp for the I-V converter can make a large impact on performance. A standard option is the OPA-627, chosen for its low noise, 4 nV/$\sqrt{\text{Hz}}$, in the 10 kHz frequency range. We tested other components but the OPA-627 offered the best performance. While developing the electronics for the system, it is usually helpful to check for agreement between the expected noise characteristics for a given circuit and the actual values as measured. This helps us optimize the detection circuits and can highlight weak links in the instrumentation. For example, the quality of the power supply for the I-V converter can have a drastic effect on the noise of the circuit. Figure 2.29**b** shows two noise spectrums taken using different power supplies. Almost an order of magnitude improvement in the signal to noise ratio (S/N) is achieved.

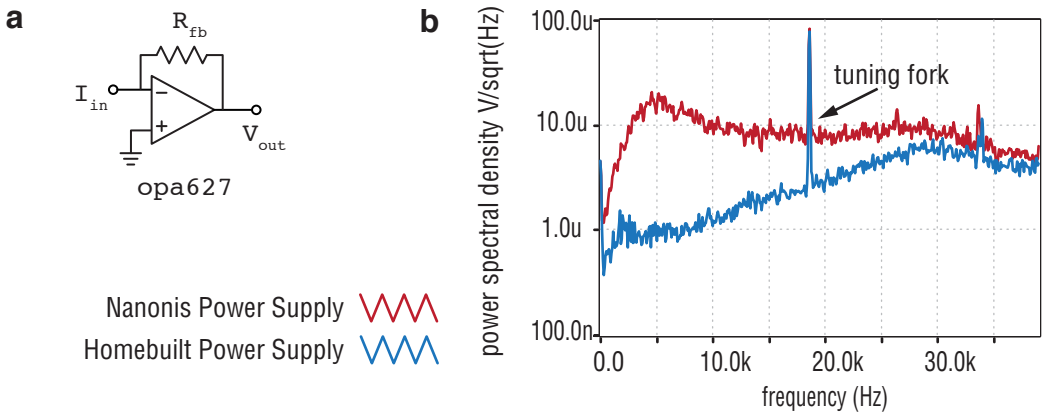

Figure 2.29: **a**: A standard inverting amplifier. **b**: The power supply included with the expensive SPM hardware turns out to be much more noisy than the homebuilt one.

Improvements to the I-V converter

Initial tests of the instrument involved a simple set up like this, and for many applications, such a unit would suffice. However, with some adjustments and additions, we can easily improve the measurement capabilities. For example, just the addition of a second amplification stage after the IV converter will:

- increase the signal level to better utilize the full input range of the PLL,
- decrease unwanted influence from triboelectric noise sources in the cabling,
- can be designed to help in driving the high capacitive loads to the PLL input terminal.

Thus, an additional stage was added after the IV converter consisting of an AD817 op-amp with a gain of 10.

Additionally, we can use the geometry of the tuning fork electrodes to our advantage by measuring the difference between the signals on each electrode, as opposed to grounding one and measuring the current through the other. Although this differential measurement adds another feedback resistor to the circuit, and therefore the corresponding amount of Johnson noise (Eq. (1.5)), there is still an overall increase in the signal to noise (S/N) by the amount of

$$\frac{(S/N)_{\text{diffAmp}}}{(S/N)_{\text{IVconv}}} \propto \frac{2S/\sqrt{2R_{\text{fb}}}}{S/\sqrt{R_{\text{fb}}}} \approx 1.4\,. \tag{2.26}$$

The major drawback to this approach for a preamp, is its physical distance from the tuning fork. Since the op-amps will not function at low temperature, it needs to be installed at room

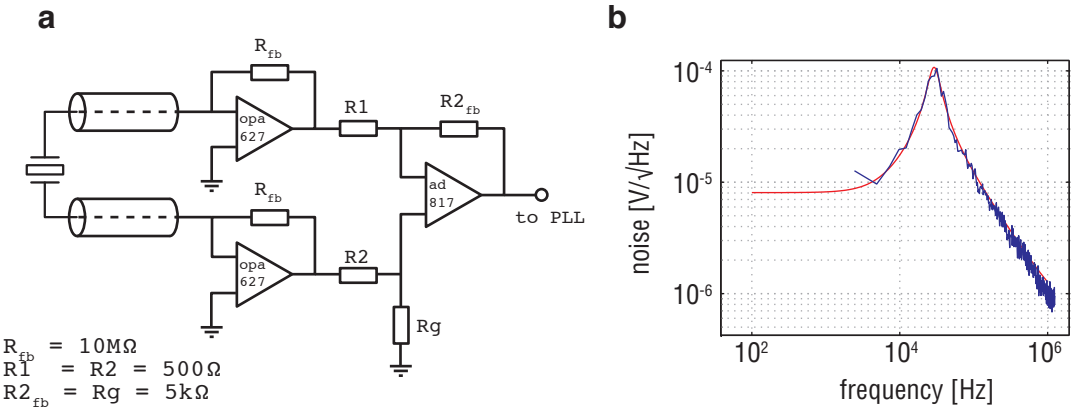

Figure 2.30: **a**: Schematic for the differential amplifier setup and **b**: SPICE simulation, in red, compared to the actual noise measurement, in blue.

temperature. The closest place therefore is on the very top of the cryostat, approximately 2 meters away from the SPM. Thus, several complications arise due to the long cabling required. Most detrimental is the parasitic capacitance of the coaxial cable connected to the input terminal of the IV converter. The effect of this noise can be seen in the S/N ratios from the IV converter. Figure 2.31**a** shows S/N curves taken over the range of the tuning fork with different input capacitances added to the input (accomplished just by using long coax cables). Clearly, a dramatic loss is seen in the frequency range of normal operation, $\sim$ 10 kHz.[11]

Phase Detection

The frequency and amplitude of the tuning fork are the key measurable quantities for many of the applications of the ULT-SPM. Researchers have developed many methods for making such measurements. The most common method currently used for low-temperature, tuning fork based systems involves a phase locked loop (PLL). Recently, commercially available systems designed for scanned probe instruments have eased the incorporation of such schemes while offering high quality performance specifications.

[11] Active shielding was tested as a means of countering this effect, however, no improvements could be found. Thus, a preamp designed for operation at helium temperatures to be mounted much closer to the microscope is currently being developed.

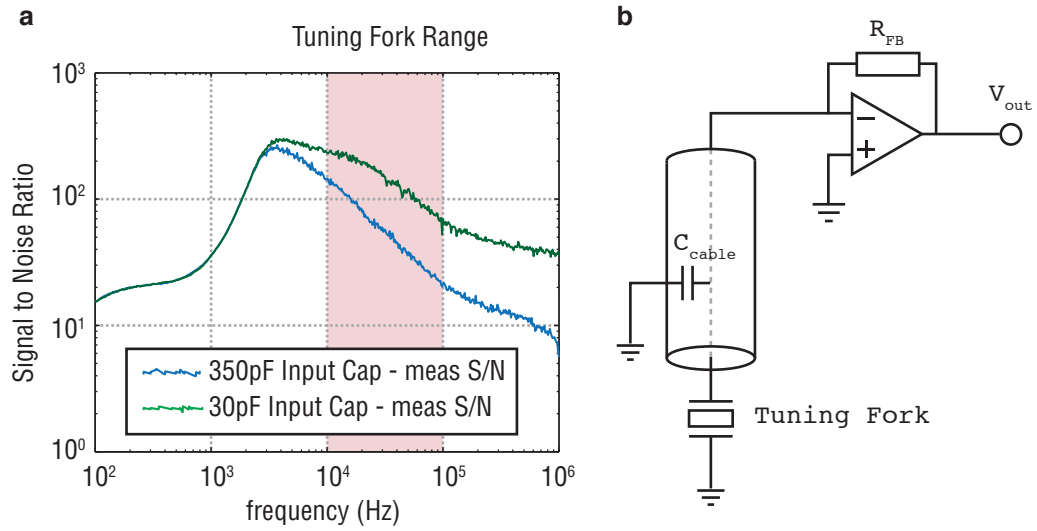

Figure 2.31: **a**: Measured signal to noise ratios for short verses long input cables. **b**: The schematic showing the input cable capacitance.

Phase-Locked Loop

As shown in Fig. 2.32**a**, the heart of the PLL is a phase sensitive detector which measures the discrepancy in phase between two signals: an input signal and the frequency of a voltage controlled oscillator (VCO). Thus, if a phase difference exists, the VCO responds by altering its frequency until the mismatch is reduced to zero, or an arbitrary constant. In the case of the tuning fork based FM-AFM configuration, the VCO is responsible for the excitation signal to the cantilever and the input signal is the piezoelectric current generated by oscillating tuning fork. Thus, deviations in f_0 of the tuning fork due to tip-sample interactions are measured by the Δf of the VCO.

The role of the PLL unit in the FM-AFM mode is to

1. adjust the frequency of the cantilever excitation signal to match a Δf corresponding to tip-sample interaction force,
2. maintain a constant amplitude of oscillation,
3. output the error signals from the two feedback loops to the SPM controller.

The first two goals are accomplished by two feedback loops, the gains of which are determined by the quality factor and f_0 of the oscillator and the demodulation bandwidth of the PLL. The tuning fork parameters are in general not variable and must be determined experimentally,

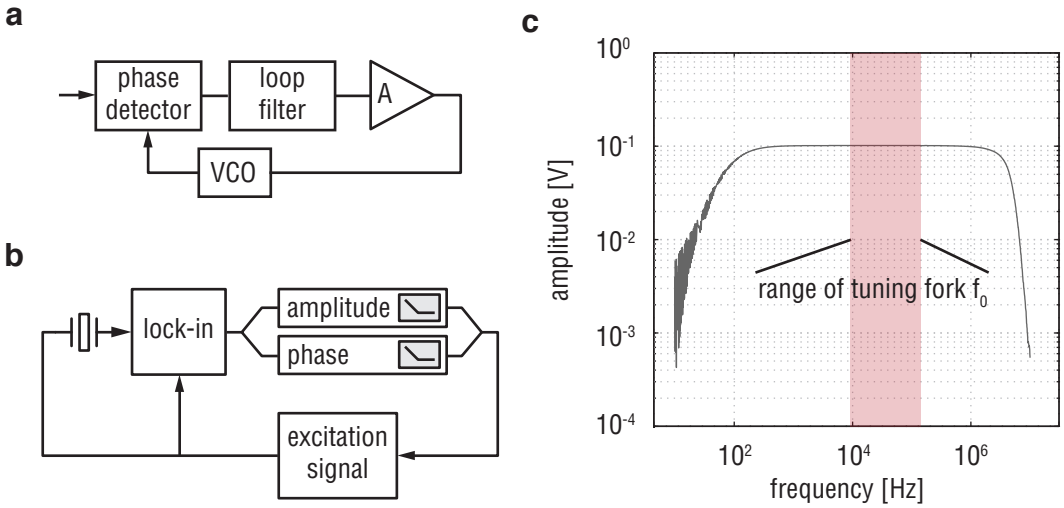

Figure 2.32: **a**: Basic components of an analog PLL. **b**: Application of PLL principle to SPM oscillator. **c**: Transfer function of Nanonis OC4 PLL showing operating range of 100 Hz to 5 MHz while measuring a 100 mV ac signal. The highlighted region shows the standard range in which the tuning fork oscillators operate.

but the demodulation bandwidth is adjustable with obvious tradeoffs between frequency noise and acquisition speed. Effectively, adjusting the bandwidth of the PLL changes the frequency of the loop filter. For fast scanning, a high bandwidth setting (100 Hz) is appropriate, while bandwidths in the order of 1 Hz are more suited for higher resolution, low noise, and slow scans where the Δf modulations are expected to be small.

The PLL chosen for the ULT-SPM experiment is the commercially available Nanonis OC4. It is a standalone unit capable of being integrated into existing instruments. It relies on the LabVIEW platform for the interface to the digital electronics of the hardware.

The Digital PLL

While the above discussion is conceptually valid for the application of PLL technologies to the SPM, the Nanonis OC-4 PLL is based on a digital architecture, rather than an analog one. Thus, the phase detector is not a VCO and does not distribute charges in response to phase errors, but rather a digital number proportional to the error.[91] A key advantage of the digital PLL (DPLL) over its analog cousin is the ability to adjust the parameters of the feedback loop, since they are just numeric coefficients. Thus, by employing a DPLL as the frequency controller, we have a wide range of easily adjustable operational parameters available. Optimization of the PLL parameters is performed automatically by the Nanonis OC-4 software, based on the

quality factor of the cantilever, and the desired bandwidth of the acquisition.[54]

The SPM Controller

Z-feedback - The Controller

In standard FM-AFM, while the PLL tracks and controls the frequency and amplitude of the tuning fork, a third feedback loop is employed to maintain a constant tip-sample distance. The Z feedback loop responds to the frequency shift output of the PLL by applying voltages to the piezo tube. We have adopted the GXSM/Signal Ranger opensource SPM controller for use with the microscope.[92, 93] GXSM offers a customizable, inexpensive, and very flexible controller for custom scan probe systems. Recent improvements in the Signal Ranger hardware have made the package a viable alternative to commercial products.

The hardware involved consists of a digital signal processor, the "Signal Ranger-Mark2" (SRMK2), and a complimentary analog to digital/digital to analog (AD/DA) converter, the "SR2-A810". The SRMK2 is connected to the PC via USB connection. The specifications and schematics are show in figure 2.33. Analog outputs from the SRMK2 are used to control the scanner, sending the scan signals to the piezotube electrodes. The 8 analog inputs of the SRMK2 can be used to record other parameters of interest. For example, the dissipation component of the tuning fork signal can be recorded simultaneously. Or, if an experiment involves correlations between tip position and other events, say changes in resistance measured via a lock-in,

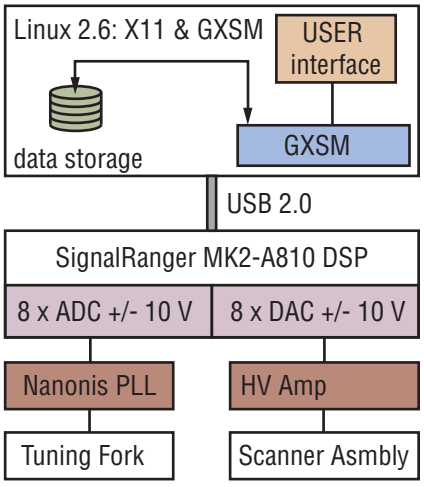

Parameters of GXMS/SRMK2	
analog i/o	8 in, 8 out; +/- 10V
ADC/DAC res.	full 16 bit
data Storage	netCDF
sampling rate	up to 150 kHz
Comp. interface	USB 2.0

Figure 2.33: Chart showing GXSM - SRMK2 interfaces, and table of relevant performance specifications.

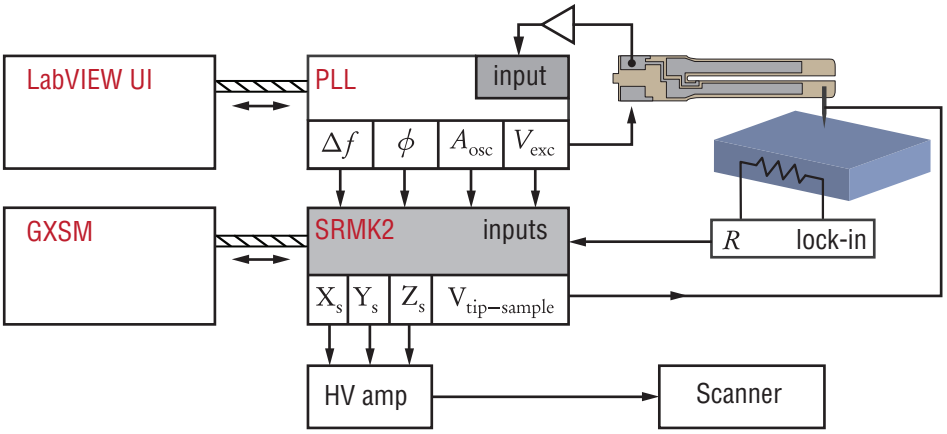

Figure 2.34: General instrument scheme for basic scanning showing the interconnections between the various components.

a voltage output from the instrument performing that measurement can easily be recorded as well. Figure 2.34 shows an instrumentation schematic showing the links between the various components.

Other parts

Also associated with the controller unit is a high voltage amplifier.[12] The high voltage amplifier accepts the +/− 10 V from the SRMK2 and amplifies the signals to the levels appropriate for the scan tube, at gains of either 1×, 4×, 15×, 40×, depending on the desired scan range or resolution.[13]

An additional component in this section is a custom, 4 channel, 3 inputs per channel, summation box used to combine voltage signals before the HV amplifier. For example, for mechanical excitation through the piezo tube, it is necessary to add a small ac component to the *z* piezo driver signal. Or, depending on the configuration of the controller software, x-y offsets can be applied to the piezo tube via the summation box. Tip-sample biases can also be controlled by the GXSM/SRMK2 combination. For example, during spectroscopy or gating experiments, an output from the SRMK2 can be connected to the tungsten tip, and given controlled voltages determined by the GXSM interface.

[12] Nanonis HVA

[13] The SRMK2 analog outputs are 16 bit, thus at T_{room}, the full range of the HV amp, 40×, gives a Z range of 7.4 μm, and will allow for a resolution of 1Å/bit. This resolution improves at low-T, where the range decreases by a factor of 5.5. If this is still insufficient, the gain of the HV amp can be reduced as well.

The controller is also responsible for some of the coarse motion. For example, while approaching the surface, the Z coarse motors move the scanner upward a short distance (< tube piezo extension range), then the piezo is extended until either the sample is detected or it reaches its maximum range. If the feedback signal does not register a significant change, the motors are actuated again and the process repeats until the surface is reached. This action is automated by a GXSM plugin. However, despite the automation, it can be laborious process, sometimes taking the better part of a day.[14]

Finally, GXSM is responsible for the storing of most of the scan information. The network common data format (netCDF) is a machine-independent, self-describing file structure designed for array-orientated scientific data. Generally used for oceanographic and geographic information, it is also well suited for scan probe information structures. Many of the scan parameters can be stored along side the actual scan data. Other scan parameters from the PLL can also be stored in a linked file via a LabVIEW - TCP/IP modules designed for the ULT-SPM project.

2.5 Chapter Conclusion

This chapter has documented most of the pertinent details that guided our decisions regarding the creation of the SPM. It is currently a fully functional instrument with all the various components operating repeatable and within the design parameters. The conclusion of the thesis will explore a few more potential modifications that might be made to the instrument in the future.

[14] While the GXSM/SRMK2 is responsible for coordinating the approach, the frequency resolution of the motor output of GXSM was found to be insufficient for the Z motors at low temperature, where very precise waveforms are needed to generate repeatable motion. Therefore, we use a function generator triggered by the GXSM/SRMK2 unit for the motor signals. Appendix C.3 contains a detailed description of how to operate the motors.

CHAPTER 3

LOW TEMPERATURE EQUIPMENT

3.1 Introduction

While many experimental physics apparatuses come as complete pre-made units, ready to collect data, the ULT-SPM has been devised and assembled from various sources. As shown in the previous chapter, the AFM was entirely constructed from scratch. This chapter deals with the other main pieces of the experiment: the low temperature and high magnetic field (B) systems. The dilution fridge chosen for the project needed many modifications before being able to accept the SPM, and the infrastructure in the lab needed to be built. The following discussions highlight many of the experimental procedures and know-how regarding the low-T/high-B components.

3.2 Dilution Fridge

Proposed by H London, in 1951[94], and first realized in 1965[95], the ^{3}He-^{4}He dilution refrigerator has since been the standard means to reach temperatures in the milliKelvin regime. Essentially nothing more than a series of different diameter pipes, a pump, and a few carefully placed heaters, a dilution fridge relies on the unique properties of ^{3}He and ^{4}He to achieve its cooling power. Of course, the reality of the situation is a bit more complicated than just plumbing, so a brief discourse on the operation and physics of the standard dilution unit will be helpful.

Understanding a dilution fridge begins by considering the phase diagram for mixtures of ^{3}He and ^{4}He, shown in figure 3.1.

^{3}He and ^{4}He and Their Mixing

Below $\approx$ 700 mK, the mixture will form a two phase solution: one phase (dilute) consists of mostly ^{4}He, and the other (rich) is mostly ^{3}He. Due to the quantum properties of the helium atom, these two phases are described by different statistics. The integer spin and resulting Bose liquid properties of the ^{4}He atom allow the dilute phase to make a transition into the superfluid state, while the half-integer and Fermi liquid nature of ^{3}He create a highly viscous fluid.[1] The

[1] This is true of ^{3}He only above 2 mK, where it too forms a superfluid, although for quite different reasons than the bosonic ^{4}He.

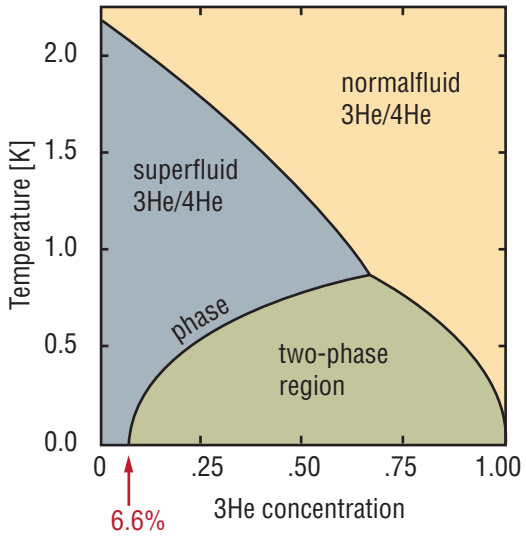

Figure 3.1: The phase diagram of ^{3}He/^{4}He showing the ratio of the two components versus the temperature. (After [101])

critical feature of this phase relation occurs at the bottom left corner of the phase diagram, where it is observed that for concentrations above 6.6% ^{3}He, there is a non-zero minimum for the ^{3}He concentration. Thus, the ^{3}He particles can be effectively *dissolved* into the rich phase to any temperature. The operation of the dilution refrigerator relies on the migration of ^{3}He particles across the boundary separating the rich and dilute phases. This action is accompanied by cooling, since there exists an enthalpy difference between the two phases, as demonstrated by measurements of their specific heats.[96, 97] In the ideal case, the cooling power associated with such a mechanism will be given by the enthalpy difference and the rate of migration:

$$\dot{Q}_m = \dot{n}_3 \cdot \left(H_d(T) - H_c(T)\right) = 84 \cdot \dot{n}_3 \cdot T^2 \frac{\mathrm{J}}{\mathrm{mol} \cdot \mathrm{K}^2} \tag{3.1}$$

where: H_d and H_c are the enthalpies of the dilute and concentrated phases, respectively, $\dot{n}_3$ is the flow rate of ^{3}He across the phase boundary, and T is the temperature of the mixing chamber. This cooling process, neglecting the quantum nature of the helium isotopes, can be compared to the classical action of evaporation. The superfluid ^{4}He bulk liquid acts as a vacuum into which the ^{3}He particles disperse from the concentrated phase, in a process somewhat like water evaporating into steam.

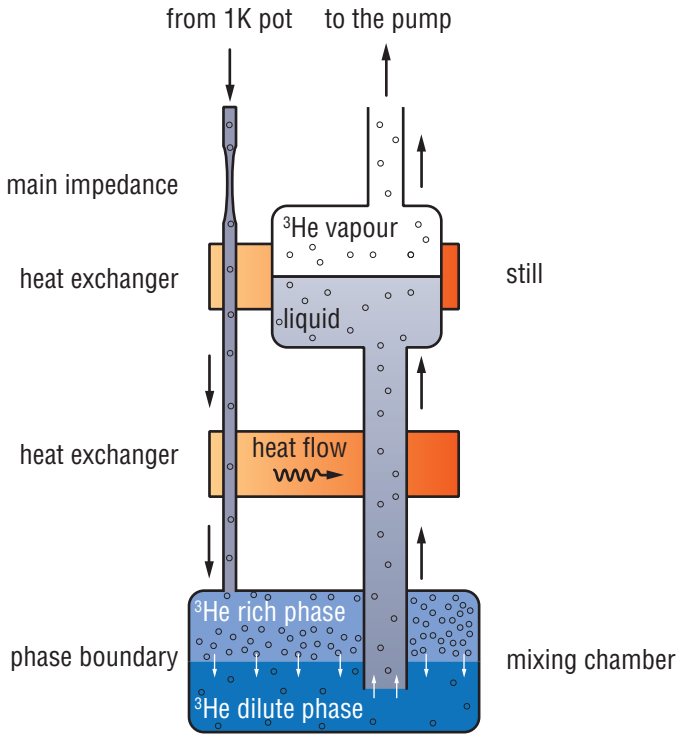

Figure 3.2: A schematic of the dilution unit showing the flow of ^{3}He atoms through the important stages

Realization of the Dilution Unit

A schematic version of the dilution unit, as shown in figure 3.2, shows the critical phase boundaries of the mixture, and the migration of the ^{3}He atoms in the mixing chamber. The mixing chamber is the bottommost section of the fridge, and the component which achieves the lowest temperatures, thus, it is used as the thermal anchor for any materials needing to reach the base temperature, in particular, the sample under investigation.

Circulation System

As seen in Eq. 3.1, the flow rate, $\dot{n}_3$, of ^{3}He through the phase boundary is critical for achieving low temperatures, thus, many of the other components of the dilution fridge are designed to improve this factor. The standard mode of operation for most of the ULT-SPM experiments is the continuous circulation mode. In this mode, the ^{3}He is constantly circulated throughout the closed loop of the fridge: the rich phase is continuously being replenished with the ^{3}He particles after they are removed from the still. However, before they can enter the rich phase, the gas

must be condensed and its temperature decreased. By removing the vapor above liquid ^{4}He, its temperature can be reduced to 1.3 K. This is the role of the 1 K pot, a small vessel filled with ^{4}He from the bath and connected to a mechanical pump. As the incoming ^{3}He passes in thermal contact with the 1 K pot (after previously being cooled to 4.2 K by the liquid helium bath), its temperature is lowered and condensation can begin. Just below the 1 K pot is an impedance which serves to increase the pressure of the incoming mixture and ensures that condensation occurs at the level of the pot and not further down, where the heat from condensation would be detrimental to the lower temperature components. After condensing, the mixture must be cooled further. This is accomplished by the heat exchangers, critical components in the design of a fridge, which use the outgoing mixture from the mixing chamber to cool the incoming helium.

Figure 3.3 shows a schematic of the dilution fridge circulatory system and its major components. The ULT-SPM system has been designed and constructed *in-house* to meet the needs of the fridge without adding any unnecessary complications. The gas handling system (GHS) serves as the main control panel for determining rates of flow for the return mixture. (See Appendix E.1 for details on the GHS)

Many factors combine to determine the value of $\dot{n}_3$ in eq. (3.1), most of which are determined by the internal geometry of the fridge itself, and are therefore not mutable in this experimental apparatus. However, a major component that is under our control is the flow rate allowed by the still line and its pump. As discussed later in 3.6, the pumps have been located far from the dilution unit, to minimize mechanical noise from the motors. This leads to long pumping lines, which, given the typical equations for flow rates, F go inversely as the length, l, and at least as the third power of the pipe radius, a:[98]

$$F \propto \frac{a^3}{l}\,. \tag{3.2}$$

To ensure proper pumping rates along the still line, given its length of approximately 15 meters, we chose an 80 PVC pipe with interior diameter (ID) of 8". The return and bypass lines are 1/4" copper tubing. A 3" ID 80 PVC pipe was used for the 1 K pot lines.

Modifications to the fridge

Mechanical

As delivered, the dilution fridge terminated at the mixing chamber. In order to a) mount the AFM, b) provide a scaffolding for the cabling, and c) ensure the sample is located in the maximum field region, an experimental tail was designed and constructed. (Included in the tail design is a flexible bellows which helps prevent vibrations from reaching the AFM and is discussed further in section 3.6.) The tail is made of coin silver, an alloy of 90% Ag, 10% Cu, often used

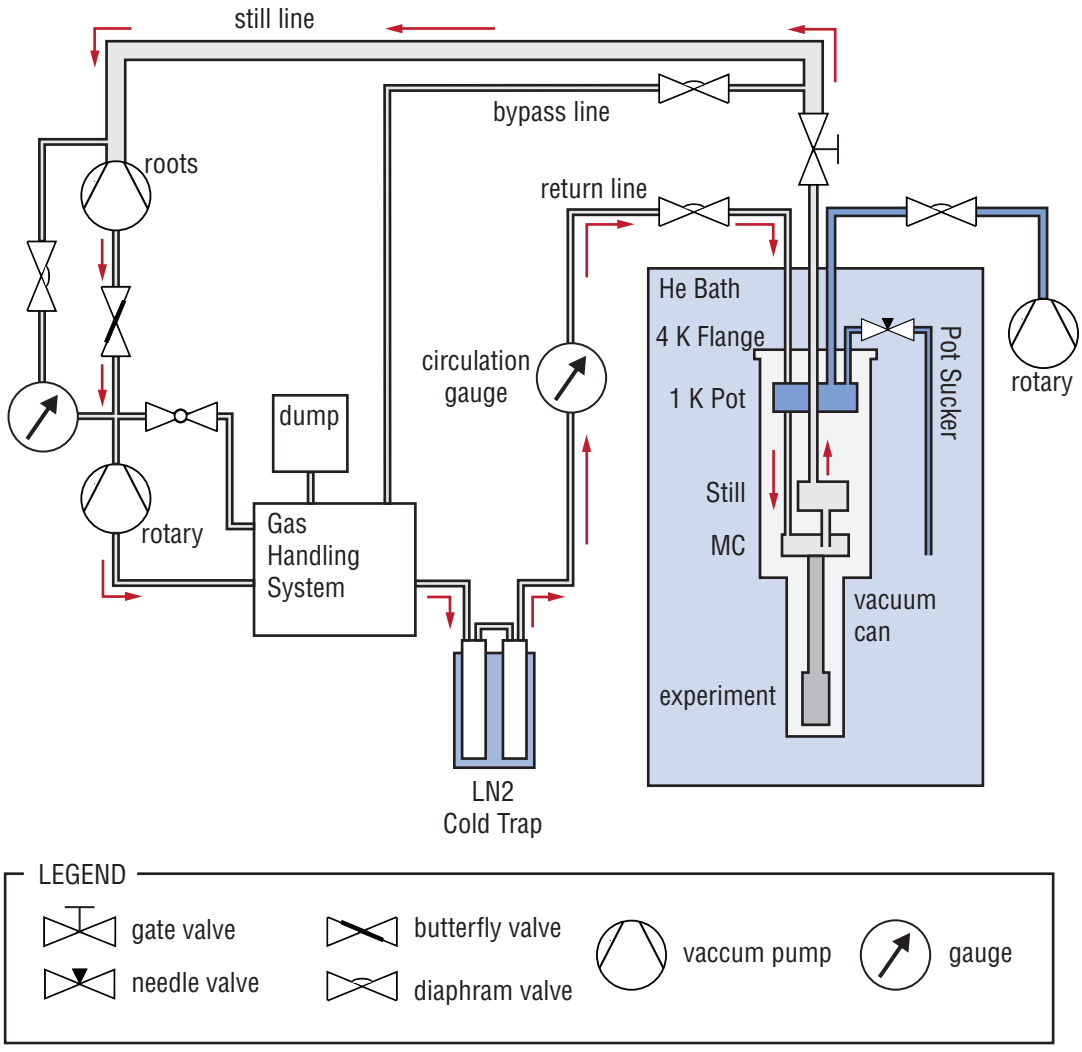

Figure 3.3: Circulation schematic showing the closed system and route for the mixture during normal operation.

in low temperature apparatuses due to its machinability and excellent thermal properties.[99] It is affixed bellow the stainless steel (SS) bellows and thermally connected to the mixing chamber using annealed copper braids (since SS is known not to be a great thermal conductor at low temperatures[100, 101] and also bears a Schottky anomaly in its specific heat below 100 mK which can lead to long thermal relaxation times [102]). This Ag rod terminates in another small Ag flange to which the AFM is affixed.

Also, the electrical feedthroughs at the head of the cryostat had to be significantly expanded from their original design. We added two, hermitically sealed, input/output (i/o) boxes to the room temperature side of the cryostat. One serves as the connector bay for the microscope cables (tuning fork, high-voltage etc.) while the other has the transport and thermometry wires and connectors.[2] Vacuum tight BNC connectors are installed for the coaxial cable, while 32-pin military style connectors are used for the twisted pair bundles.

3.3 Wiring of the Fridge

Basic wiring scheme

Major modifications to the dilution unit's electrical wiring had to be done in order to accommodate the various components of the AFM. The AFM alone requires:

- High-Voltage (< 1000 kV) compatible wiring for driving the piezotube and coarse motors, [5 for the piezotube, 3 for the x-y motors, and 2 for z (twisted pairs)]
- Coaxial cables for the tuning fork signal and the capacitive position sensors [2 coaxes for the tuning fork, and 2 for the sensors],
- Excitation leads for the position sensors [4 for the x-y sensors and 2 for z (twisted pairs)],
- leads for biasing/grounding the tip and exciting the tuning fork [1 for the tip, and 2 for the excitation piezo (twisted pairs)].

This is in addition to the standard transport leads (6×2 twisted pairs) for sample based measurements as well as thermometry and heater connections, and other miscellaneous cables such as an LED for light treatment used in tuning the density of a 2DEG during cooldown.

Installation of these cables is not a trivial matter since they must be thermally anchored in the right places, terminate in a vacuum sealed connector, and be comprised of several different materials depending on the temperature gradient they span. Also, the routing of the cables is an important aspect of the wiring. For example, sample leads, in which capacitively generated

[2] See section 3.3 for more details.

femtoamp signals can interfere with measurements, should be isolated from the high-voltage AFM cables.

Heat sinking the twisted pair wires is achieved by wrapping them around a copper bobbin, as shown in figure 3.4**b**. The wrapping is then sealed with a thermally conductive, low-temperature compatible epoxy[3] and the polished face of the bobbin is pressed into contact with a component of the fridge. Coaxial cables are anchored using tightly clamped metal fittings applied at the metal connectors. These anchors are positioned at the 4K flange, the 1K pot, and below the mixing chamber.

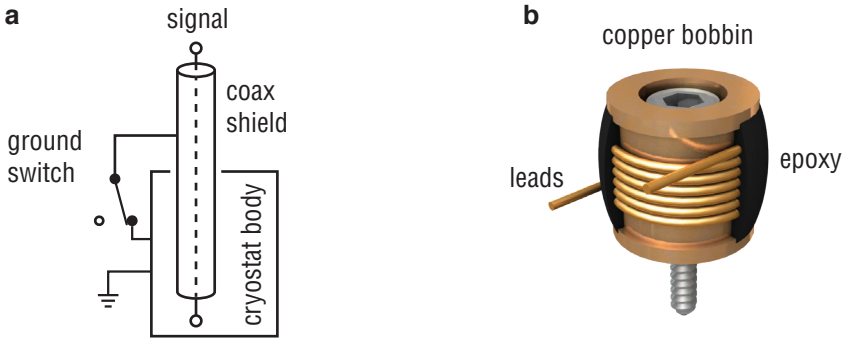

Figure 3.4: **a**: A schematic showing the ground switch at the head of the cryostat. **b**: The standard means of heat sinking cables accomplished by wrapping them around an OFHC copper bobbin which is screwed in place to a section of the fridge.

Of the AFM related cabling, the coaxial cables for the tuning fork signals are the most critical. Since the piezoelectric current from the tuning fork is in the order of picoamps, proper shielding must be in place to guard against external noise. This necessitates the use of coaxial wires in which the outer shield is grounded. Since the configuration of the external microscope circuitry can change, it is beneficial to have the option of either grounding the shields directly to the cryostat, or choosing a grounding point on the instrumentation rack. Therefore, a switching box has been added to the upper vacuum areas which can either connect the coax shields to, or isolate it from the cryostat body. Figure 3.4**a** shows the schematic of the switching element.

Proper filtering of the cabling can prevent heating of the mixing chamber due to high-frequency EM interference, common in today's communication driven environment. Since radio frequency signals are currently not a planned component to any ULT-SPM experiment, pi-filters[4] were installed in all the transport and high voltage lines.[98] These are also contained in the upper vacuum i/o boxes.

[3] e.g. Stycast 2850-FT
[4] Spectrum Control, 56-711-013, 3 MHz cutoff

Power, Grounds, and Ground Loops

A perpetual blight on the fruit of low-level measurements is the dreaded *ground loop*. Careful attention to the wiring schemes are the best defense against this enemy. The basic strategy involves choosing one ground point for the entire experimental apparatus.[98, 103] Figure 3.5 shows the basic idea in which all elements requiring a ground connection make that connection directly to one centralized ground point. A ground loop can be formed when two grounds points which might be at slightly different potentials are used in the instrumentation or infrastructure circuitry. A slight ΔV in the two grounds can cause a current to flow thereby interfering with the measurement. The large amount of cabling and instrumentation components required for the ULT-SPM apparatus demands fastidious attention to the grounding paths. Current flow from ground loops can also be responsible for heat leaks on the fridge, preventing operation at base temperature.

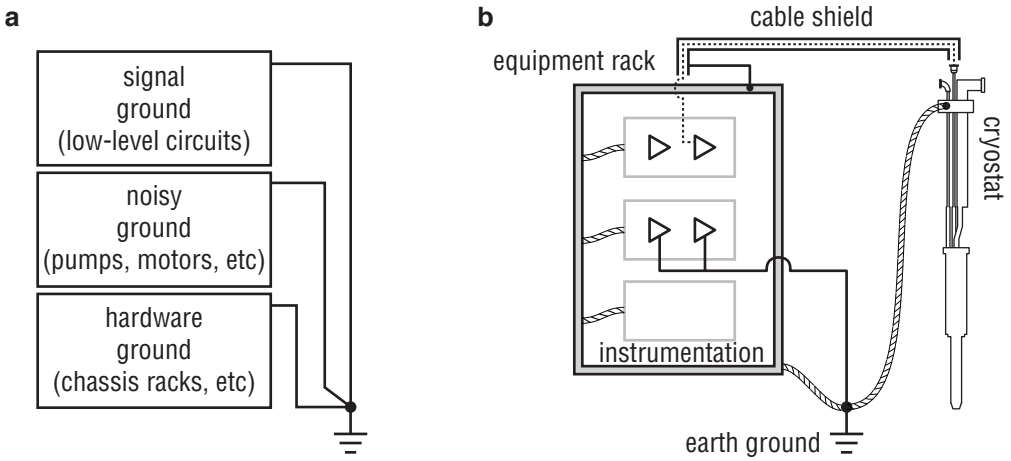

Figure 3.5: **a**: The basic scheme for designing grounding routes showing a central, well-defined ground. Keeping the the low-level measurement signal separate from the noisy motors is helpful. **b**: The general layout of the ULT-SPM grounding routes. Attention must be paid to the shield of the wires leading the fridge to ensure they do not connect the instrumentation panels to the cryostat.

To help keep the sensitive measurement electronics isolated from local sources of electronic noise, isolation transformers were installed for the lab, thus providing a clean power source for the instrumentation components. This prevents electronic noise from building operations such as the ventilation system or elevators as well as the directly connected pumps and computers, from coupling to the measurement electronics.

3.4 Thermometry

Since the ULT-SPM experiment is not intended to reach temperatures below 50 mK, the demands on the thermometry are significantly reduced, as compared to experiments seeking 10 mK measurements. However, accurate assessment of the experimental temperatures is crucial and does merit careful consideration.

The fridge is equipped with 4 resistance thermometers localized at specific points along its length. The ruthenium oxide (RuOx) thermometer relies on the negative temperature dependence of a thin-film, metal-ceramic composite resistor which is thermally anchored to a fridge component, i.e. the still or mixing chamber. They are ideal for measurements down to 50 mK in part because:

- reproducibility in measurements after repeated thermal cycling,
- small changes due to magnetic fields ($\approx$ 2% over 8 T), thus preventing errors in temperature measurements when high B-fields are present,
- small size and mass, making installation easy,
- measurement are fast and require little power or complicated electronics,
- low cost.

Since the RuOx thermometer relies on relative resistance changes, each unit must be calibrated before use at low temperatures. For some of the thermometers on the CF-50 unit, this was performed by the previous owner. For the remaining, a calibrated thermometer was installed to ensure accurate temperature measurements.[5] Figure 3.6 shows the locations of the various resistance thermometers on the fridge.

Measurement is performed by an ac-resistance bridge technique using the Picowatt AVS-47A. This instrument allows for low-excitation levels at low temperatures in order to prevent self-heating of the resistor and contains a convenient computer interface and multiple channels for monitoring several thermometers. Measurements of the MC and AGRod thermometers are taken using a four probe configuration in order to prevent the lead resistance from altering the temperature measurements.

3.5 Magnet

The magnet used in these experiments is an Oxford C16/18L, superconducting solenoid. Capable of continuous 16 T operation (18 T if the bath temperature is reduced to 2.2 K), this magnet

[5] Lakeshore 202A

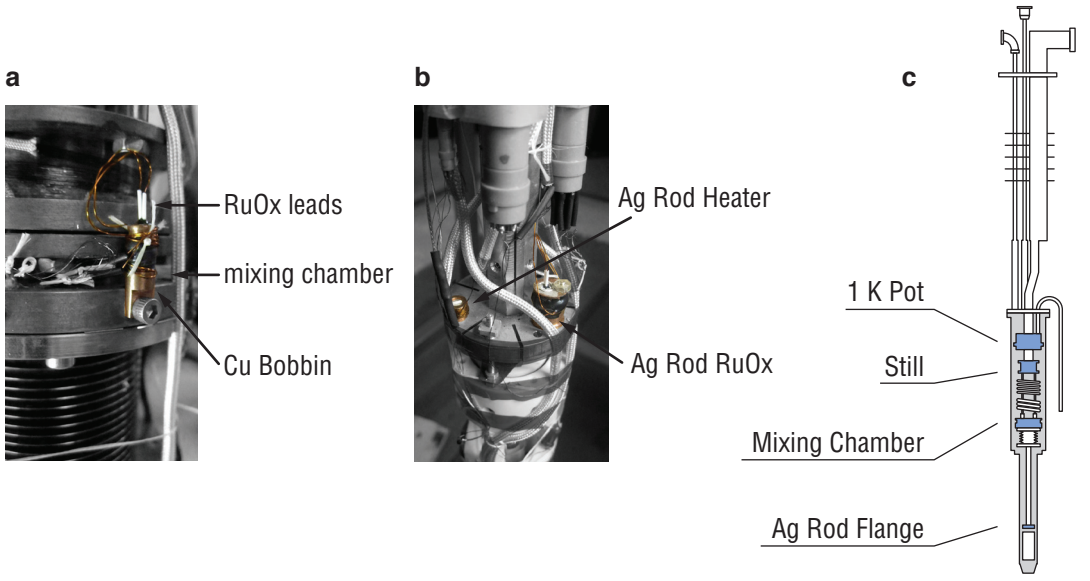

Figure 3.6: **a**: A view of the standard mounting scheme for a RuOx thermometer encased in a Cu bobbin and heat sunk to the mixing chamber. **b**: The Ag Rod tail showing a heater and thermometer. **c**: The locations of the four resistance thermometers on the fridge.

significantly expands the experimental parameter space of the instrument (the average for low-T systems is about 8 - 10 T). It is also equipped with a field cancellation coil which severely reduces the magnetic field in the area of the mixing chamber, thus avoiding heating as a result of ΔB induced currents as well as magnetic field influence on the resistance thermometry.

The magnet is controlled by an Oxford IPS-120-10 power supply which provides an extremely stable current source. It can be operated using the front panel or programmatically using the GPIB/LabView based interface, which allows for integration with the scan probe data acquisition. To set the magnet in persistent mode, a small dedicated current source was built to provide up to 100 mA to the switch heater.

3.6 Vibration/structural

Aside from careless errors, the other major problem for force microscopy is unwanted noise from external vibrations. The ultimate resolution depends in part on the stability of the microscope: how constant can we keep the tip sample separation distance? Also, reaching base temperatures of dilutions refrigerators requires a very still instrument. To address this issue, significant steps were taken to ensure a 'quiet' microscope.

Environmental sources for vibrations include:

Specifications of the Magnet	
Maximum Central field	16 T (4.2K) - 18 T (2.2 K)
Homogeneity	0.1 % in 10 mm D.S.V
Current Decay in Persistence Mode	$< 10^{-4}$ per hour
Magnet Bore Diameter	52 mm
Normal Inductance	76 Henries
Persistent Switch Current	60 mA
Field Cancellation Region	60h x 50d cylinder centered 37 mm above central field
Field/Current Ratio	0.1567 T/A

Table 3.1: Specifications of the superconducting magnet.

Building Vibrations

Typically between 5 and 200 Hz[104], a building will have a resonant frequency and can induce coupled oscillations in equipment located within. This source is significantly attenuated simply by locating the instrument in the basement.[6] Normally, the environmental influences from the building are also reduced by the use of an air table or ceiling mounted suspension springs for example.[105] However, accommodating the dilution fridge and magnet prevents those options, due to its vertical size ($\sim$2 m) and the need for easy raising and lowering of the fridge. Thus, we have also constructed an isolated concrete foundation that extends below the lab floor to support the experiment. Figure 3.7 shows the essential components of the vibration isolation structure. In this way, the experiment is almost completely decoupled from the building and instead rests on the bedrock of Montreal.[7] Additionally, the entire experiment is supported by three air cushions placed between the wooden frame and the concrete foundation.[8] These air cushions can be pressurized during sensitive measurements further isolating the microscope from the building. Figure 3.7**b** shows the power spectral density of the tuning fork signal taken at 4.2 K in feedback on a smooth surface. Employing the air table eliminates one peak at 60 Hz and decreases the low frequency components slightly. The motivation for such a structure is derived from the harmonic response of a series spring-mass-damper systems. Appendix D contains more analytical details of such systems.

[6] A basement lab also discourages unwanted displacements of the experimenters by concealing the presence of sunny skies.

[7] While this design works great for reducing influences from the building, the experiment is still susceptible to disturbances occurring in the substrate of the city, for example, jackhammering at nearby construction sites or even the rare earthquake.

[8] Vibraplane Model 1206, Kinetic Systems

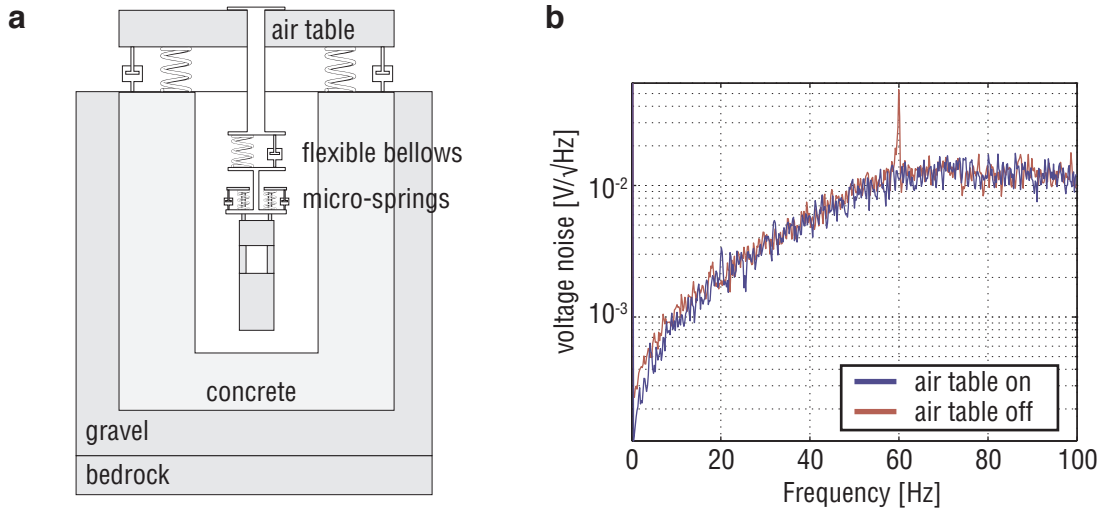

Figure 3.7: **a**: The general scheme for the low-frequency vibration isolation showing the various isolation stages of the support structures. **b**: Noise density of the tuning fork signal in feedback with and without the air table floating.

Vacuum Pumps

Operating a dilution fridge requires the use of up to 3 separate vacuum systems; the 1K pot, circulation system, and the vacuum can all need their own pumps and lines. Since each pump can be a source of mechanical vibrations, it is crucial to isolate them from the experiment. This has been accomplished by locating the pumps far from the experiment in a separate room, at the cost of reduced pumping speeds, as well as by including several vibration suppression devices along the lines themselves. Figure 3.8 contains an overhead view of the ULT-SPM lab space showing the remote location of the pumping room and the vibrational suppression elements along the pumping lines.

At the boundary of the pump room, all the pumping lines are set into a concrete block. This is similar to the sand box technique in which the lines are encased in a box of sand, damping longitudinal vibrations. Using a simple accelerometer (ADX-L05), we can make some qualitative measurements of vibrations occurring in various points in the lab. Figure 3.9**b** shows the spectral analysis of the accelerometer when it is placed directly on the pump verses the pumping lines after leaving the pump room.[9]

Additionally, the still line and the 1K pot pumping line both have short sections of lead pipe spliced into the line near the fridge. These provide impedance mismatch boundaries, effec-

[9]Of course, the AFM would not be installed directly on the pump.

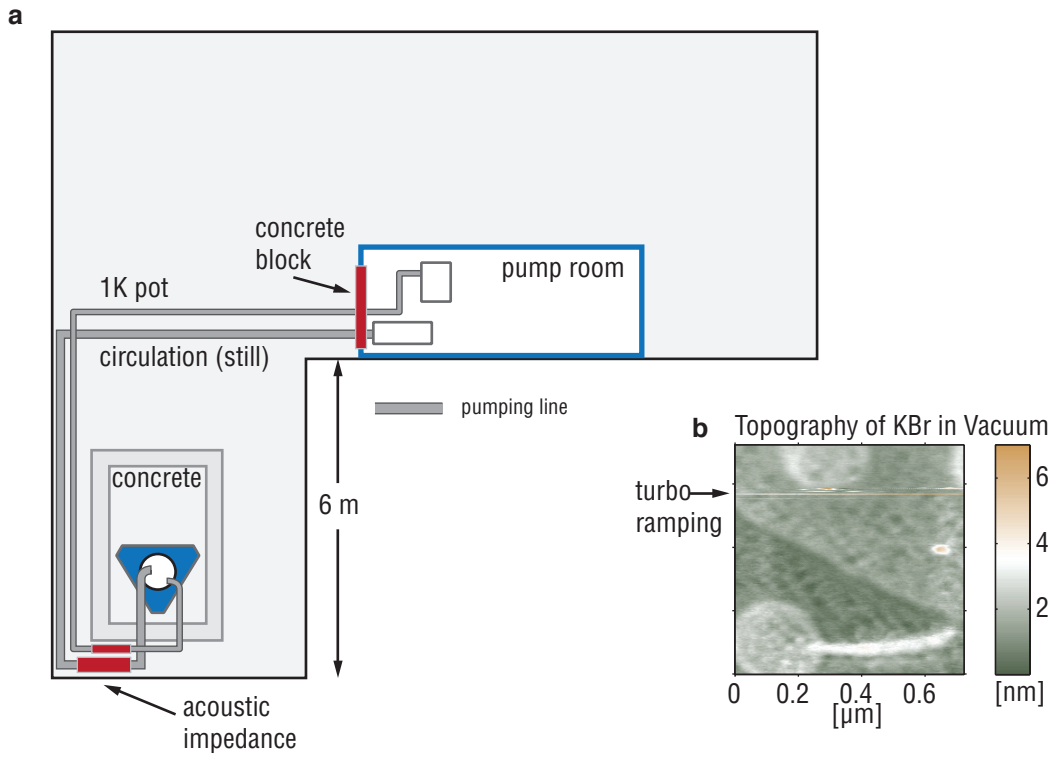

Figure 3.8: **a**: The lab floor plan showing the layout of the pumping lines, pump room, and vibration impedance **b**: A topographic scan of a crystal terrace on KBr taken while the turbo was ramping. Only a minor influence is seen at one particular scan line when the rotation frequency of the pump matched a resonance of the structure.

tively reflecting mechanical vibrations that reach the junction. Finally, a double gimbal bellows connects the last section of stainless steel still line to the top of the cryostat. The double gimbal bellows arrangement has been shown to be a very effective for reducing the vibrations transmitted by large diameter lines such as the still line.[106]

A third pumping line is attached to the cryostat for pumping the vacuum can. This is a turbo pump that is mounted off the structure, but nearby, and connected via flexible bellows to the vacuum can port. Figure 3.8**b** shows a topography scan taken of a KBr surface in vacuum. The turbo pump was powered up during the scan. As a result, a brief period of disturbance is marked in the upper section when the turbo rotation frequency matched the resonance of a component in the SPM or the fridge structure.

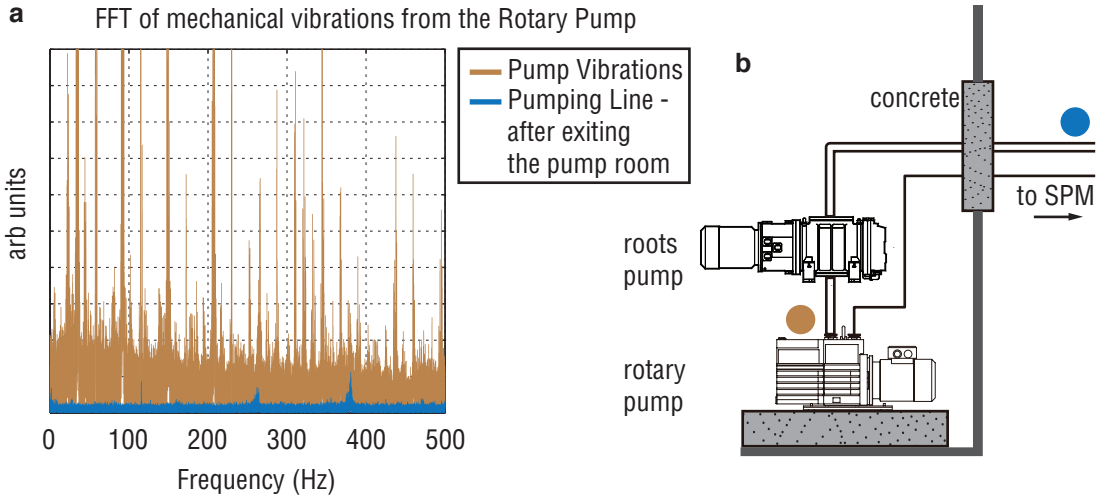

Figure 3.9: **a**: FFT of accelerometer measurements **b**: scheme of the pump room showing the two points of measurement plotted at left.

Cabling Connected to the Cryostat

The ULT-SPM cryostat head has 3 military style, 32-pin connectors, plus 8 coax cable inputs. These wires can also be source of vibration and are therefore separated into more flexible smaller units, rather than large, stiff cables which can easily transmit vibrations to the cryostat body.

Internal Vibrations of the Dilution Unit

It has been well documented in related experiments, most notably the bolometer based measurements of electromagnetic radiation,[107, 108] that the flows of cryogenic fluids within a dilution unit can be source of mechanical noise for various detectors. Tuning fork based force microscopes should also be isolated from these noise sources. Previous schemes for dealing with these vibration in general resort to modifications of the internal fridge components.[109, 110] However, this involves tinkering with the internal plumbing of a dil fridge, an adventure not recommended unless absolutely necessary. Thus, we added an isolation stage beneath the mixing chamber of the fridge consisting of a stainless steel flexible bellows.[75] The bellows were custom made for this application out of 304 stainless steel.[111] Measurements in liquid nitrogen gave a spring constant value of 201 N/m, which assuming an underdamped oscillator behavior and a mass of 2 kg for the AFM and AG rod assembly, results in a transfer function for an oscillatory excitation as shown in figure 3.10. Thus, strong attenuation of unwanted

vibrations from the 1K pot can be expected by the inclusion of the flexible bellows.[10] Images taken below 4 K also display no discernible influence of the 1K pot, or circulation flows, on the resolution of the instrument.[11]

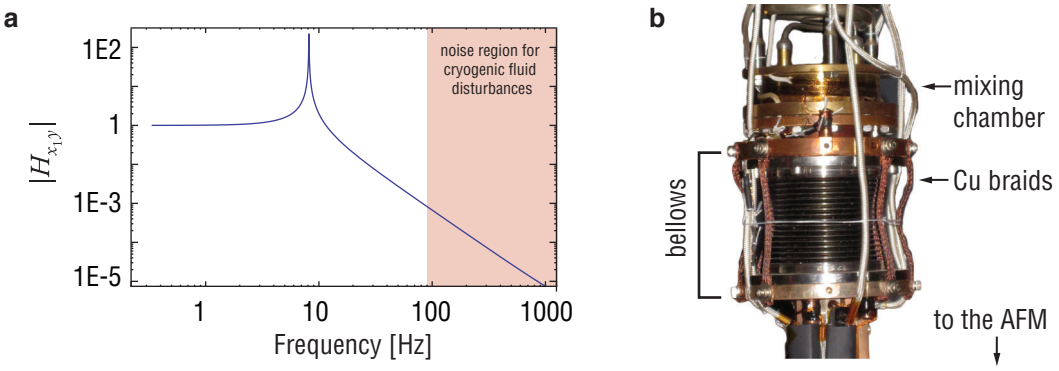

Figure 3.10: **a**: Analytical estimation using methods described in appendix D of the transfer function for the stainless steel bellows with a highlighted region showing the area of concern of 1K pot/bubbling vibration noise. **b**: A photograph of the bellows showing their location directly below the mixing chamber.

3.7 Chapter Conclusions

In this chapter we've discussed the workings of the low-T/high-B environments and systems. The infrastructure required for low vibration milliKelvin experiments was fully documented as were the details of the dilution unit. Figure 3.11 gives an idea of the experimental environment of the ULT-SPM.

[10] See Appendix D for more regarding the analysis of transfer functions for mechanical vibration isolation

[11] Very recent investigations of the system using an amplifier mounted inside the vacuum can have revealed vibrational influences on output of the low temperature transistor. This low-T preamp is mounted above the 1K pot at the 4K flange, with no vibration isolation in between.

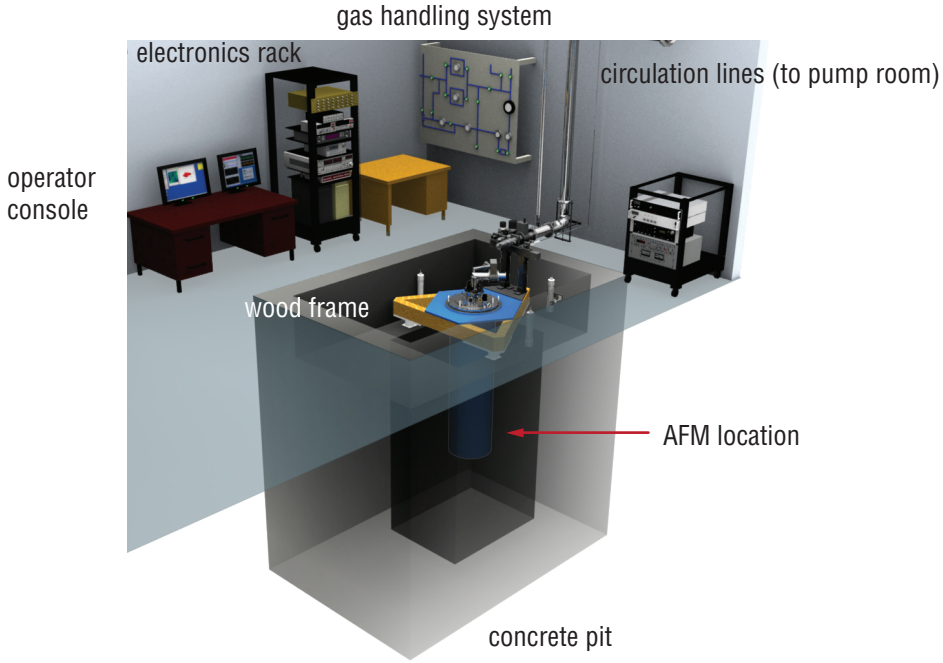

Figure 3.11: A 3D rendering of the ULT-SPM corner of the lab showing the general layout of the experimental space.

CHAPTER 4

CHARACTERIZING THE AFM IN LOW-T, HIGH-B

4.1 Calibrations

Piezo Tube Calibrations at T_{300K}

z calibrations

As seen in the descriptive framework of piezoelectricity (See appendix A), knowing the exact values of the piezoelectric constants is essential to quantifying the displacements of the piezoelectric crystals and their relation to the induced or applied electric potentials. These values are known based on the type of piezoelectric crystal employed and geometrical estimations can be used to achieve a rough calibration. However, for a proper assessment of the actual displacement/field ratios, we must use a calibrated sample with features that are precisely known.

For the z displacements, we can approximate the ratio using[112]:

$$d_{31}\frac{l}{d} = \left(1.73\frac{\text{Å}}{\text{V}}\right)\left(\frac{2''}{.039''}\right) = 89\frac{\text{Å}}{\text{V}}\,. \tag{4.1}$$

Here, l is the length of the piezotube, d is the wall thickness as described in Figure 2.3, and d_{31} is piezoelectric constant of the Lead zirconate titanate (PZT) as described in appendix A.

Using a known calibration grid, as shown in figure 4.1, we can refine the estimation, after which we arrive at 93 Å/V for the z displacement.

x-y calibrations

A similar approach is used to calibrate the displacement of the piezotube in the x-y directions. Using analytical approaches[113], the deflection is related to the applied field as follows:

$$\frac{2\sqrt{2}}{\pi}d_{31}\frac{L^2}{d\cdot R_I\cdot 2} = .9\left(1.73\frac{\text{Å}}{\text{V}}\cdot\frac{2''^2}{.039''\cdot.176''}\right) = 947\frac{\text{Å}}{\text{V}}\,, \tag{4.2}$$

with R_I being the inner radius as shown in figure 2.3. Again, after using a known grid, like the image shown in figure 4.2, we can refine the estimation and arrive at 1126 Å/V for the lateral deflection.

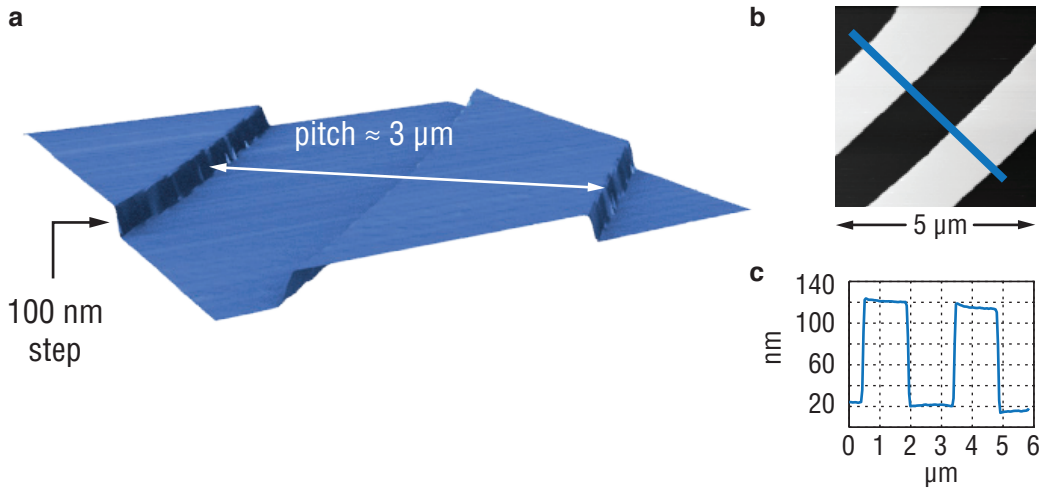

Figure 4.1: **a**: 3D topography of a standard calibration grid (µmash TZ02). Well defined steps are used to calibrate the z piezo coefficients. **b**: The same area as in **a** showing the line profile extracted in **c**.

Temperature Effects on d_{31}

PZT ceramics suffer a decrease of 82% in the piezoelectric response between room temperature and 4.2 K.[114] This decline essentially saturates at around 4 K.[115]. We confirmed this response by measuring the spacing of well-defined atomic terraces in cleaved KBr(001) at low temperatures. A multiplicative factor of $\sim 1/5.5$ converts room temperature distances to 4 K, as seen in figure 4.3.

Tuning Fork Sensitivity

In order to make quantitative assessments of the forces at play during an experiment, we need to have a value for the sensitivity of the quartz tuning fork, that is, a ratio between its amplitude of oscillation and the electrical output generated by the piezoelectric effects as well as the pre-amplification stages (usually expressed in V/nm). In standard Si cantilever based AFMs, this is accomplished automatically since the interferometers used to measure the deflections are well calibrated. Optical methods can be applied to the tuning forks as well, however, such measurements require a custom interferometer setup.[116] Analytic estimations can also be used based on the equations governing the piezoelectric effects as well as the gains of the I-V converter.[117]

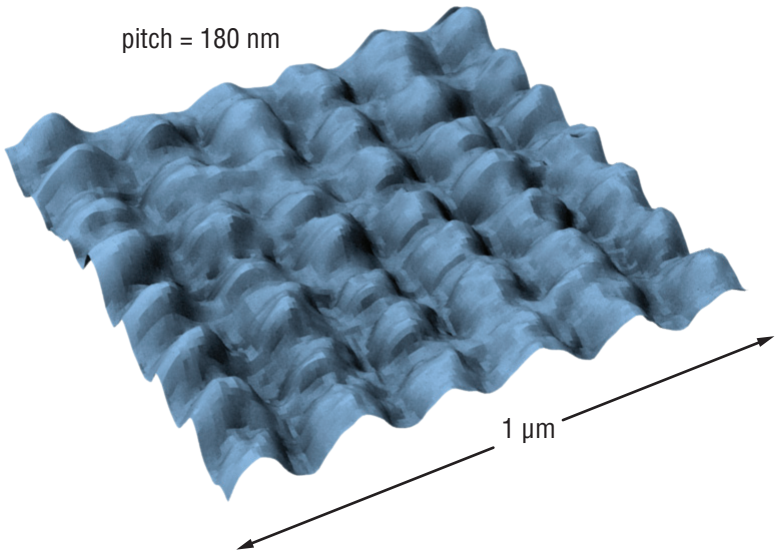

Figure 4.2: A grid used for x-y calibrations

Analytic estimation

Using the the relations derived in section 2.3, we can write for the strain, ϵ, on the upper surface of the beam, where the electrode is situated:

$$\epsilon = \frac{Mx}{EI}\,. \tag{4.3}$$

If $M = F\,(y-a)$, and $F = kx'$, with x' being the displacement of the end of the tine, then

$$\epsilon(y, x = t/2) = \frac{t}{2} \times kx'(y-a) \times \frac{1}{EI}\,. \tag{4.4}$$

Since the strain will cause a stress $\sigma_{\text{mech}} = \epsilon E$, we can expect a surface charge with density σ_{charge} to form at the electrode:

$$\sigma_{\text{charge}} = \sigma_{\text{mech}} d_{12} \tag{4.5}$$

where d_{12} is the piezoelectric constant, in this case representing the ratio of charge per unit area flowing between connected electrodes perpendicular to the x direction to the stress in the y direction.[118]. Integrating from $y = 0$ to $y = l_e$, i.e. the approximate length of the electrodes, as well as across the width of the tuning fork: [119]

$$\int_0^{l_e} \int_{-w/2}^{w/2} \sigma_{\text{charge}}\, dz\, dy = 12 d_{12} kx'[y-l]\frac{1}{t^2} \tag{4.6}$$

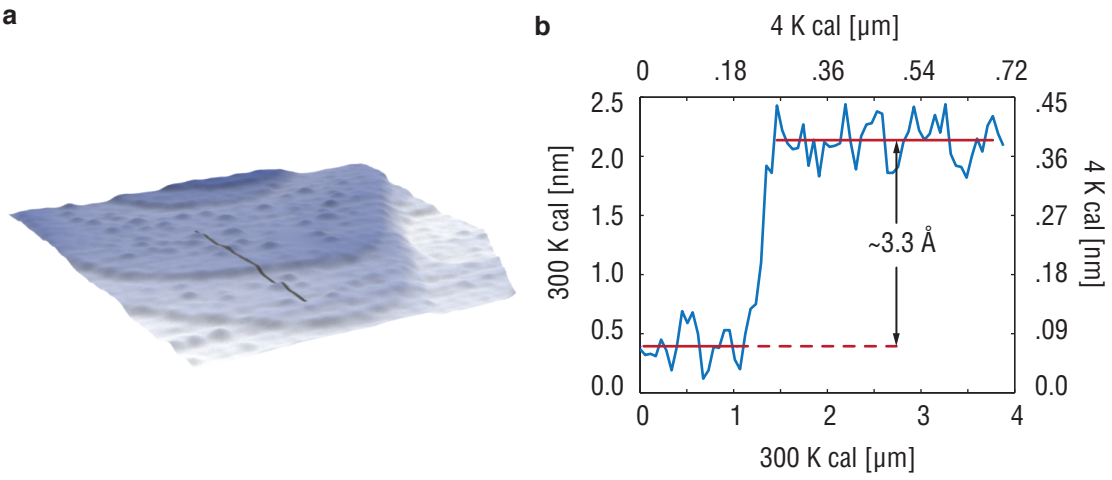

Figure 4.3: **a**: KBr topography at 4K showing the atomic terraces of the KBr crystal structure known to be 3.3 Å. (smoothing has been applied for clarity) **b** Extracted profile from the gray line in **a**. The spacing between the top and bottom terraces is confirmed. Units on the bottom and left axis are for 300 K, while the top and right axes have been converted to 4 K units.

we can then express the ratio of total charge to oscillation amplitude ratio as:

$$\frac{q}{x'} = \frac{12 d_{12} w k l_e}{t^2}\left[\frac{l_e}{2} - l\right] = 2.18 \frac{\mu \mathrm{C}}{\mathrm{m}} \tag{4.7}$$

Using the approximate gain of 2×10^8 from the differential amplifier as described in section 2.4, and the angular frequency $\omega = 2\pi \times 20$ kHz, we can expect a sensitivity of ~ 54 mV/nm.

Experimental measurement

Aside from the interferometric measurement, there are other, and more accurate, options for experimentally determining the sensitivity of the quartz tuning fork forces sensor. One can use the thermal spectrum of the noise from the tuning fork in conjunction with the equipartition theorem, which gives an estimate for the thermally excited amplitude at temperature T:[117]

$$A_{\text{thermal (rms)}} = \sqrt{\frac{k_B T}{k}}\,. \tag{4.8}$$

However, since the thermal oscillation amplitude at helium temperatures is smaller than our current detection scheme, this method will be difficult to employ. Also, methods using the measured quality factor and energy loss of the tuning fork also showed success.[120] However, the method we found easiest and most robust was the *in situ* characterization presented by

Giessibl.[117] This method relies on the relationship between amplitude, A, and frequency-shift, Δf while maintaining a constant distance d between the tip and the sample.

By approximations applied to the force/frequency shift relations, when $A \gg d$, we can establish the proportionality:[6]

$$\Delta f \propto A^{-2/3} \tag{4.9}$$

for constant tip-sample separation d. Thus, by measuring the extension of the piezo tube, ΔZ using two values of Δf and A, and correlating this with the amplitude of the TF signal, ΔV_{TF}, we can arrive at a sensitivity value. For the example case in Figure 4.4, a ΔZ of 6.6 ± 0.3 nm was found to be associated with a ΔV_{TF} of 587 mV, resulting in a sensitivity of 88 ± 4 mV/nm. This value was found to be fairly consistent between different sensors, and shows only a small (< 10%) change between room temperature and 4 K, since the piezoelectric constants of quartz have little temperature based deviations.[121, 122] Nonetheless, it is best to repeat the measurement for each cooldown. The dominant source of error in the measurement will be the accuracy of the piezotube extension measurement which can be improved by adjusting the feedback parameters.

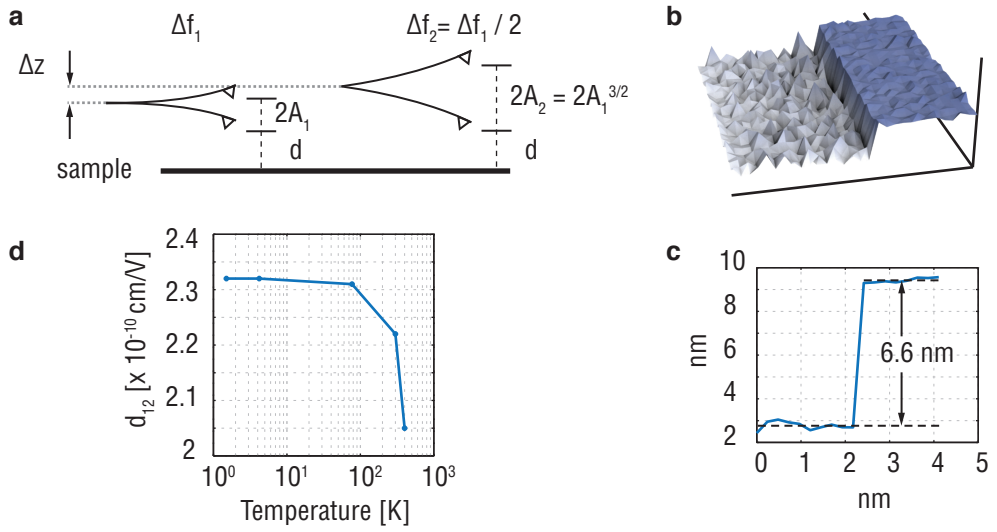

Figure 4.4: **a**: Scheme for calibrating the tuning fork sensitivity. **b**: A nearly-zero area scan showing a step in the piezo tube response as a result of increasing the tuning fork amplitude. The smaller fluctuations present are artifacts from the noise of the TF signal. **c**: A line extraction from the step offering an accurate measurement of the apparent step height in **b**. **d**: Temperature dependence of the piezoelectric constant d_{12} for α-quartz based on data from [121].

4.2 Temperature Effects

Tuning Fork at low-T

The quartz tuning fork sensor undergoes a few changes as the temperature of the microscope is lowered, its resonant frequency and quality factor being the most relevant. As quartz is cooled, the Young's modulus is known to increase by ~ 1 %.[123] From (2.22), this change will lead to an increase in the resonant frequency. For most of the tuning forks tested, this increase is in the order of 100 Hz. After reaching liquid Helium temperatures however, the temperature induced fluctuations are essentially gone. Thus parameters of the tuning fork obtained at 4.2 K are usable upon further cooling to the millikelvin regime. Figure 4.5 shows a few experimental data points for these effects.

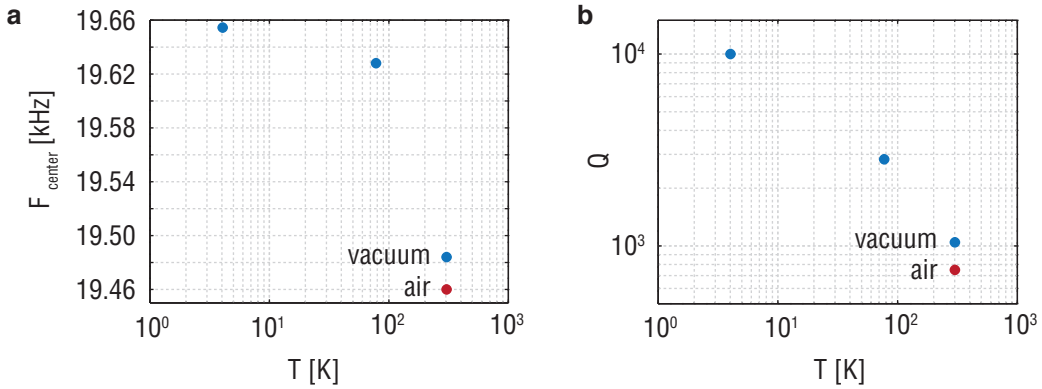

Figure 4.5: **a**: Δf of the tuning fork during a standard cooldown from room temperature to 4.2 K. (The two points at 300 K show the difference between an air environment and a vacuum) **b**: Change in the sensor quality factor due to the temperature. (Just as in **a**, the quality factor also increases in vacuum)

Another major effect due to cooling is the quality factor enhancement. In general, we can expect an increase in the quality factor of at least an order of magnitude, often even more. There are many mechanisms responsible for the increase. General stiffening of the glue joints and structural elements can be an intuitive explanation, however, the problem has also been addressed through more fundamental approaches by the micro and nano oscillator community.[124] Figure 4.5 shows the response of a typical tuning fork sensor during a cool down. The increase in Q is generally a welcome phenomenon, since, in FM-AFM, it improves the signal to noise of the cantilever detection.[8]

4.3 Operating the Microscope

Signal Noise Floor

Since every experiment must combat the same foe, noise, we should devote some time discussing achievable resolutions and noise levels of the microscope in action. As noted in Chapter 1, the signal we are most often concerned with is the frequency shift of the tuning fork sensor, Δf. Thus, the frequency shift noise, δf, plays an important role in determining the experimental parameter space within reach of the ULT-SPM. Most of the measurements discussed in this document are limited primarily by the resolution of the δf measurement.

The general form for the thermally driven frequency noise of an oscillating cantilever follows[8]:

$$\delta f = \sqrt{\frac{k_B T f_0 \mathrm{BW}}{\pi k A^2 Q}}\,, \tag{4.10}$$

where $k_B T$ gives the thermal energy, k and A are the spring constant and oscillation amplitude of the oscillator, Q is the quality factor and BW is the bandwidth of the acquisition. However, in practice, the measurement noise contributed by the detection circuitry is usually much larger than this thermally driven noise. The detector noise was found to be dependent on the amplitude, A, and the measurement bandwidth.[125, 126]:

$$\delta f_{\mathrm{detector}} = \frac{n_x}{\pi A}\mathrm{BW}^{3/2}\,, \tag{4.11}$$

where n_x is the noise density of the cantilever deflection detection, in $\mathrm{m}/\sqrt{\mathrm{Hz}}$. With the differential amplifier setup described in figure 2.30, we can obtain approximately 500 $\mathrm{fm}/\sqrt{\mathrm{Hz}}$. More standard AFM using interferometers can routinely achieve 100 $\mathrm{fm}/\sqrt{\mathrm{Hz}}$. Our increased noise is predominantly due to the distance between the force sensor and the pre-amplification stage, as noted in figure 2.31. The detector noise originates from the ability to measure the zero-crossing of the cantilever amplitude, as shown schematically in figure 4.6**a**. A plot showing the agreement between the measured noise values with the expectations based on these analytical expectations are given in figure 4.6**b**.

From these equations and plots we can see in general that δf from the detector is predominately a function of the measurement bandwidth, BW, and the cantilever oscillation amplitude, A. These two parameters are easily adjustable in the ULT-SPM set up depending on the desired measurement. Of course, compromises must be made. As we decrease BW, the rate of acquisition must also be lowered. This is less of an issue at low-T, since thermal drift is much smaller. Also, if the amplitude of the TF oscillation is increased, the tip will pass through a larger z distance, effectively smearing the measurement over the range of motion and places significant lower bounds on the observable features.[127] In general, for many of our experiments, small oscillation amplitudes are beneficial, if not required.

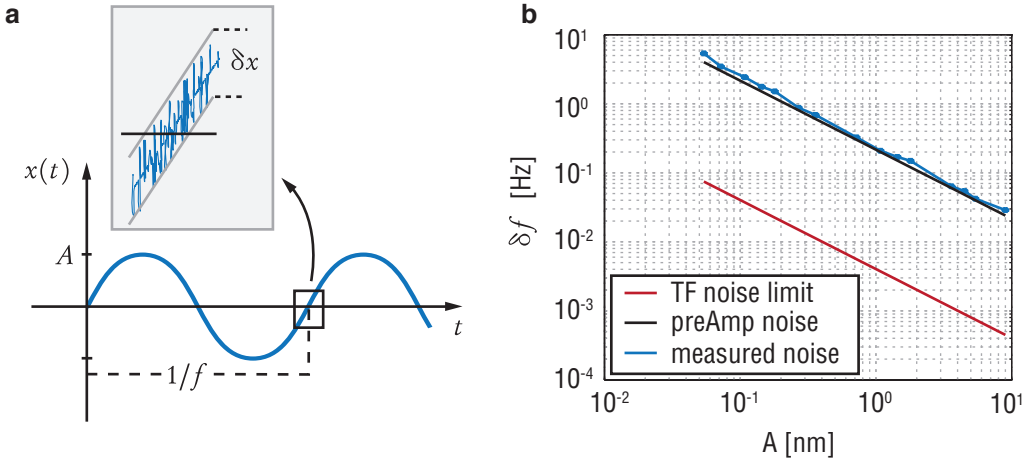

Figure 4.6: **a**: The deflection detection noise originates from the instrumental ability to measure the zero-crossing of the cantilever's amplitude. **b**: Amplitude dependence of δf at a constant bandwidth of 10 Hz. (Measurements taken at room temperature in air.)

Modes of Operation

Z-Spectroscopy

Much information can be obtained by performing *approach curves* on a sample. Simply by slowly approaching the surface with the tip, and monitoring various dynamics of the tuning fork, we can determine the force sensitivity, the general quality of the tip and sample surface, and the stability of the microscope.

Figure 4.7 shows various approach curves, each with different TF oscillation amplitudes, taken at low temperature on the GaAs sample discussed in greater detail in chapter 5. As expected from (4.9) and (4.10), decreasing the TF amplitude results in a larger frequency shift, as well as an increase in the Δf noise.

These approach curves can be analyzed further by employing a frequency shift to force integration method. We must however, reformulate the connection between force and frequency shift originally approximated by (1.2) to account for arbitrary oscillation amplitudes. In the case of small amplitude oscillations, where the tip's motion is small compared to the force gradient the following relation holds:

$$\frac{\Delta f}{f_o} = \frac{k_{\text{t-s}}}{2k}, \tag{4.12}$$

where $k_{\text{t-s}}$ is the effective spring constant between for the tip sample interaction system. In the case where the amplitude of oscillation, A, is large, implying that the tip experiences a non-

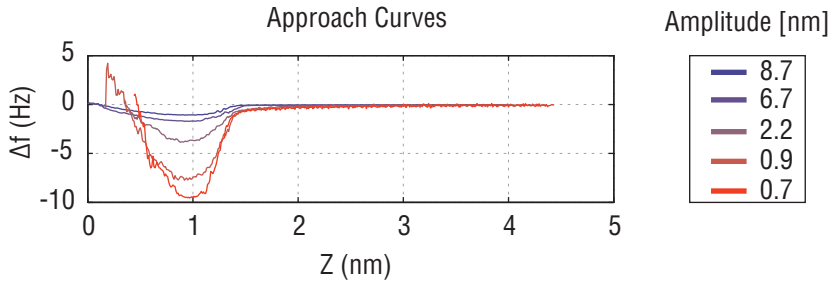

Figure 4.7: Several approach curves at 4 K showing the deepening of the frequency response curve as the oscillation amplitudes is decreased.

uniform $k_{\text{t-s}}$ during its travel, the relation must be modified to account for the changing $k_{\text{t-s}}$. Accounting for this has been shown to yield the following relation:[128]

$$\frac{\Delta f}{f_0} = \frac{1}{\pi k A^2} \int_{-A}^{A} k_{\text{t-s}}(z - q')\sqrt{A^2 - q'^2}\, dq' \,, \tag{4.13}$$

where $q' = -A\cos(2\pi f_0 t)$ and z describes the tip-sample separation. The Sader-Jarvis method describes a numerical integration technique to obtain the interaction force from the measured frequency shifts using (4.13), in addition to the mechanical parameters of the cantilever.[129] Figure 4.8 shows the results of the transformation from which we can get a rough idea of the force sensitivity of the microscope at low temperatures. Force resolution in the order of 100 piconewtons is easily available and can be improved by feedback optimization in many circumstances. This is much higher than the thermally limited force sensitivity given by:[130]

$$\frac{F_{\text{min}}}{\sqrt{\text{Hz}}} = \sqrt{\frac{wt^2}{lQ}}\,(E\rho)^{\frac{1}{4}}\,\sqrt{k_B T} \,. \tag{4.14}$$

Using the physical and geometrical constants given in figure 2.18, we can expect approximately 10 fN/$\sqrt{\text{Hz}}$ in the thermally limited case. Comparing similar instruments, it's clear that achieving thermally limited sensitivities in these configurations is not generally possible, since detector contributions to the signal noise prevail.[1]

Topographic Imaging

As an example of z noise during routine, low-T operation, figure 4.9 shows a topographic scan of self-assembled quantum dots acquired at 500 mK. After extracting the real surface features from a line trace, we can obtain a figure for the δz fluctuations during a topographic scan. The

[1] The introduction contains references for other tuning fork based low temperature AFMs.

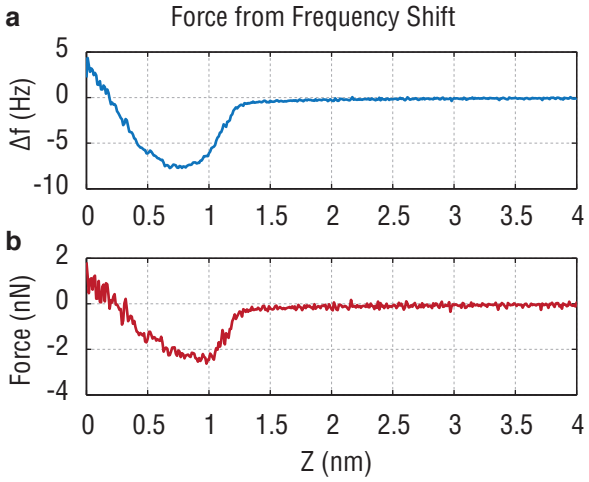

Figure 4.8: **a**: Small amplitude (9 Å) approach curve and **b**: the results of numerical integration to obtain a force distance curve, $T = 4$ K

extracted line shown in part **c** has an rms amplitude of 79 pm. This value is certainly within the range of acceptability for most AFMs.[2]

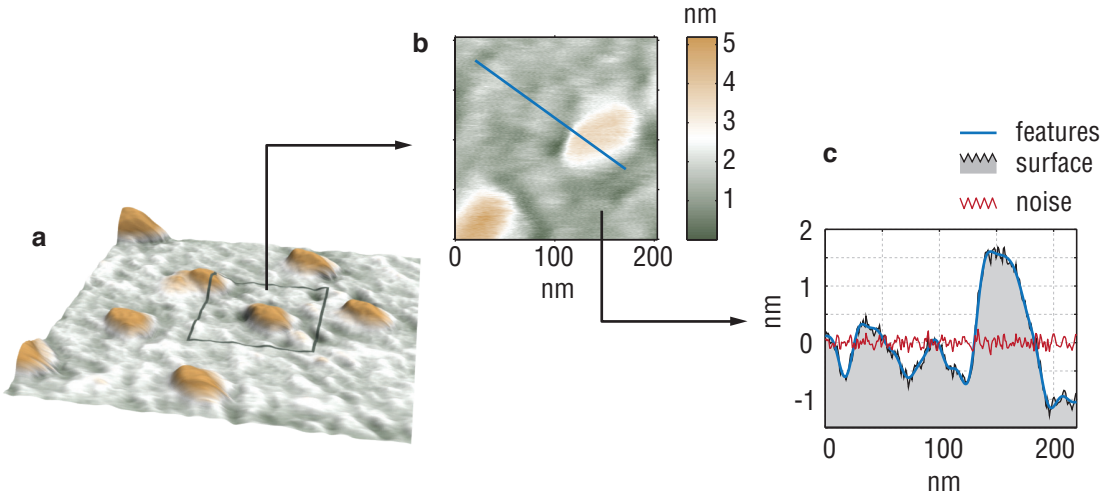

Figure 4.9: **a**: A 500 nm topography scan showing the InAs quantum dots. **b**: Smaller area scan from which the line trace (blue line) in **c** was taken. Parameters: 500 mK , 0 T.

[2]Of course, this noise is dependent on many parameters, some of which are variable depending on the nature of the experiment at hand. This value quoted above can be considered a representative example for low-T, high quality imaging.

Another important feature of the AFM is the ability to scan large areas at low temperatures, as described in the design chapters. Finding the area of interest, for example, a device structure, is a component of many experiments thus a larger field of view is helpful. Also, many of the planned experiments, contacted graphene for example, will have micron size features that the microscope needs to be able to deal with. Thus, a wide range range of operational parameters is an advantage with a low-T SPM. While the scope of the ULT-SPM project does not include much high-resolution topography, it is crucial to be able to correlate topography with any of the experiments discussed below. Figure 4.10 shows a 4.5 μm topographic scan taken at LHe temperatures. This image represents about half the maximum scan range expected for the scan tube.

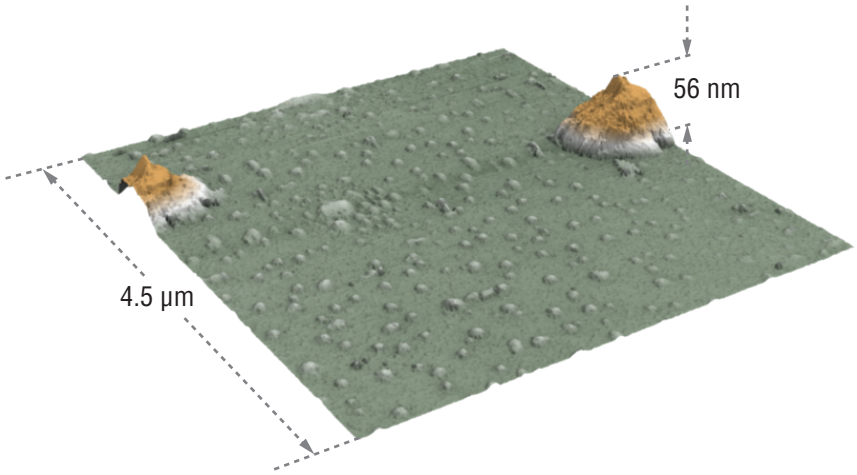

Figure 4.10: A large area scan at 4 K showing a plethora of quantum dots, smaller white features, as well as two larger, unidentified features.

Electrostatic Force Microscopy

Sensitivity of the SPM to electrostatic forces is a necessary functionality that must be available. The standard means of measuring this response is to simply apply a time varying bias between the conductive tip and the sample, and monitor the resulting frequency shift, as predicted by (1.3):

$$F_{\mathrm{ES}} = \frac{1}{2} C'_{\mathrm{t\text{-}s}} V^2_{\mathrm{t\text{-}s}}\,, \tag{4.15}$$

where the tip-sample capacitance derivative, $C'_{\mathrm{t\text{-}s}}$, is given by the exact geometry of the tip and sample, but should depend inversely on the tip sample separation: $d_{\mathrm{t\text{-}s}}$. Since Δf depends on $\mathrm{V}^2_{\mathrm{t\text{-}s}}$, and inversely on $d_{\mathrm{t\text{-}s}}$, by adjusting these two variables, we can assess this mode of operation.

Figure 4.11**a** shows the parabolic dependency of the Δf as the bias is swept between -10 and +10 volts. The process is repeated for increasing tip sample separation values. Fitting each curve to a standard x^2 form allows us to extract the curvature parameter as shown in 4.11**b**.

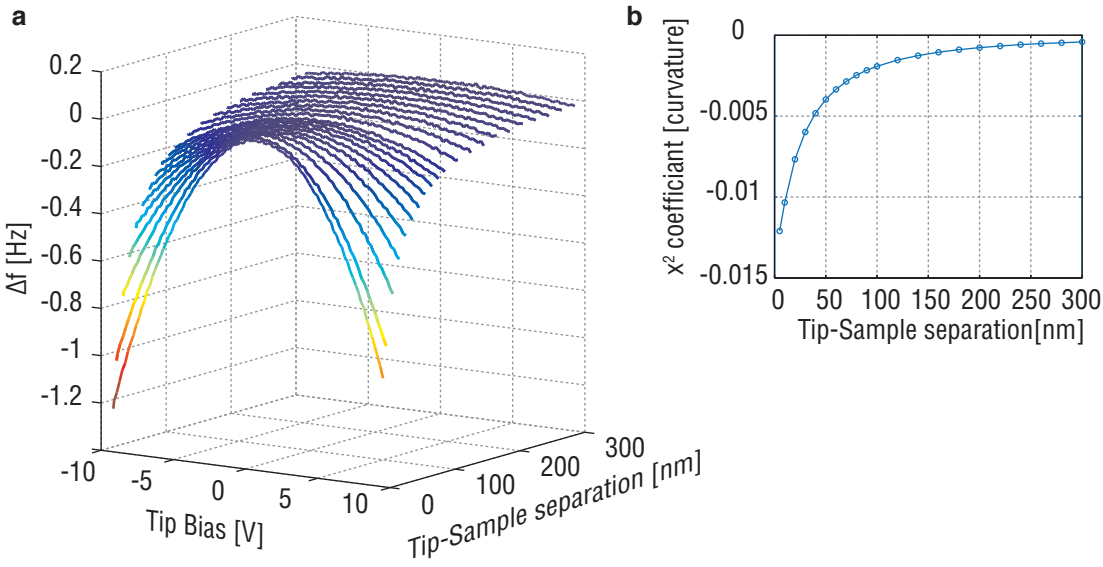

Figure 4.11: **a**: A waterfall plot showing many bias sweeps at different tip-sample separations. **b**: The fitted curvature coefficients for each sweep. The data was recorded at 4 K using the buried 2DEG sample discussed later in chapter 5.

Also, the bias can be held constant while the tip is scanned over the surface at a given height, with the z-feedback loop disengaged. Topological features will appear in the Δf signal since their presence alters the $d_{\text{t-s}}$. Figure 4.12 shows an example scan of this method. As the scan height is increased, the features visible in the electrostatic signal become reduced, as expected.

Since the tuning fork is not locked in a z feedback loop during EFM scans, the Δf noise is essentially given by the noise from the oscillation detection circuit. As we mentioned above, this is almost invariably much larger than the thermal noise from the cantilever itself. Figure 4.12**b** shows a section of the frequency shift measured at constant height far above a relatively featureless section of an insulating sample. Acquired with an oscillation amplitude of 10 nm at a demodulation bandwidth of 50 Hz, the thermal noise on the cantilever should be 85 μHz, based on equation (4.10). Due to the contribution from the sensor electronics, the actual measurement noise is 4.5 mHz. The more than 50 fold increase is expected from analysis of the preamp noise contributions as demonstrated in figure 4.6.

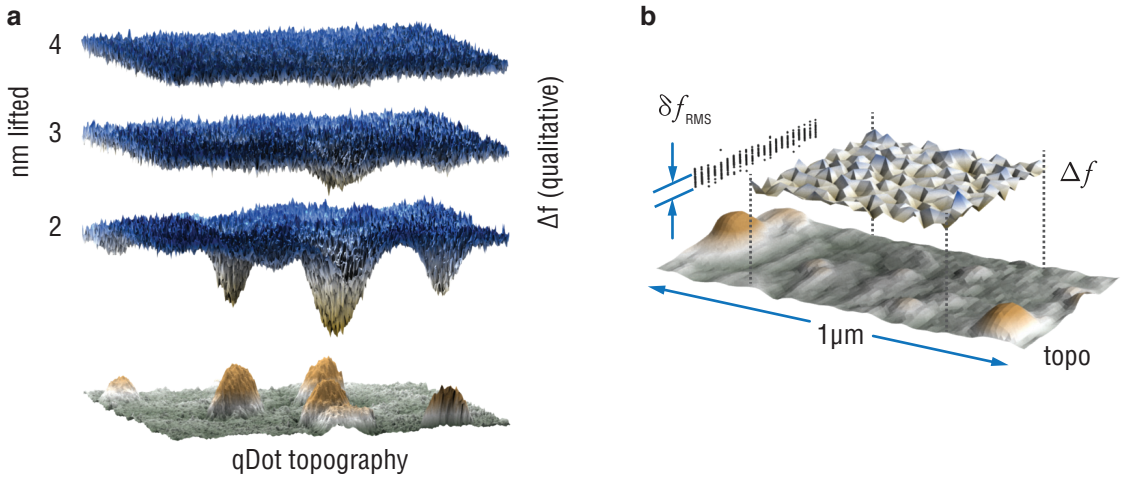

Figure 4.12: **a**: Qualitative EFM over InAs quantum dots. $V_{t\text{-}s} = 10V$. **b**: Noise in the frequency shift measurement during EFM while scanning 80 nm above a smooth region of an insulating sample at 4 K. The rms noise is measured to be 4.5 mHz.

Scanning Gate Microscopy

While scanning gate microscopy (SGM) has not been employed in any of the experiments performed so far in the ULT-SPM, it is nonetheless a mode of microscopy employed to great success elsewhere. [131, 132] Thus, it is worth noting its applicability here. In essence, the tip acts as a movable gate. Since the electrostatic fields produced by a biased tip are local and well-defined, a sample sensitive to external electric fields will respond to changes in the tip position and its bias. Unlike the modes discussed above, SGM does not record the dynamics of the tip, since it is usually not excited into vibration from this process, but only its position and bias. This information is then correlated with, in most cases, transport measurements of a sample taken simultaneously. The salient point here is that we are now using the microscope not as an external observer, but as an active component in the investigation of a sample.

A gated transistor offers the easiest explanation of the SGM principle, as shown schematically in figure 4.13. Many configurations of SGM have shown to be useful, but they can all be reduced to the following. The tip, which moves in relation to a feature on the sample, is given a static, or time-varying potential with respect to an element of the system under investigation. While changing the relative positions of the tip and sample, or simply varying the potential difference, some component of the device is monitored simultaneously. The two measurements are then spatially correlated.

To verify the possibility for scanned gate experiments in the future, we have tested for a de-

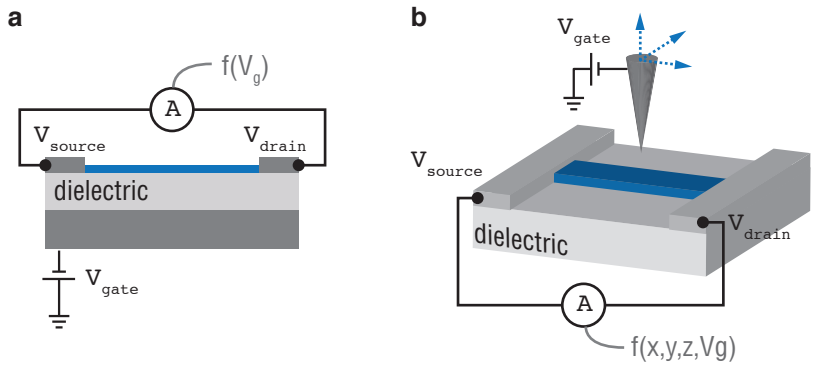

Figure 4.13: **a**: The standard gated device (DUT in blue) scheme in which the gate is fixed in its position with respect to the sample and **b**: the scanning gate setup where the gate, i.e. the SPM tip, is free to travel thereby localizing the gate induced potentials.

pendence on the local electron density of a shallow 2DEG.[3] The self-assembled quantum dots shown above in figures 4.10 and 4.12 have a 2DEG located 20 nm below the surface. Applying a negative bias to the tip will enhance the local density of the 2DEG.[53] And conversely, a positive bias in the tip will reduce the local density. However, the reduction of the electron density under the tip will modify the tip-sample capacitance, by effectively creating a hole in the lower half of the plate capacitor directly beneath the tip. This distortion of the electrostatic geometry of the tip-sample system in turn alters the functional form of the tip-sample capacitance by forcing the inclusion of a voltage dependence capacitance.

$$C(z) \Rightarrow C(z, V) \tag{4.16}$$

We can see the consequences of this by performing a Δf versus tip bias scan, as shown in figure 4.14. The scan shows an asymmetric parabola indicating a departure from the typical V^2 dependency shown in figure 4.11. Thus by the demonstrating the density shift induced by a tip-sample bias, it is fair to say that with the proper sample in place, the microscope would be well-suited for many exciting SGM based experiments.

4.4 Magnetic Field Operation

The primary concern of the high-field SPM is to minimize, if not entirely exclude any distortions to the measurements caused by the applied magnetic field, i.e. to make sure that any

[3]The fabrication of an appropriate SGM sensitive sample is not a trivial feat, otherwise, more extensive testing of this method would have been performed.

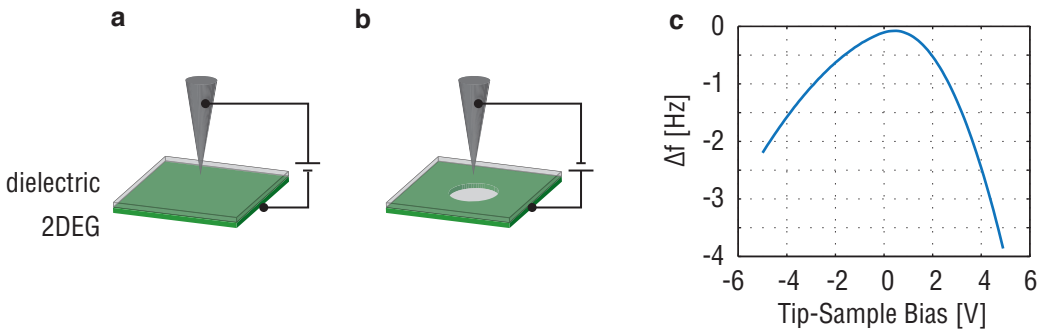

Figure 4.14: **a** and **b**: Effect of enhanced enhanced and reduced local electron density on the capacitor geometry based on tip-sample bias. **c**: The asymmetric parabola as a result of the density shifts.

deviations recorded are indeed from the sample under investigation and *not* artifacts from the scan probe. The easiest way to test the high field performance is by simply using a non-magnetic sample and ramping the field as high as we can.

The SPM

To test for spatial translocations due to the perpendicular magnetic field, topographic images of KBr were acquired between 0 and 15 T, as shown in figure 4.15. From these images, it is clear that any lateral displacement between the tip and sample is negligible.[4] Although some smoothing of the features occurs throughout the series, this is not attributable to the magnetic field and is likely due to a dulling of the tip over the course of many scans.[5] A nanoindentation is also visible in the center of the scan. This feature is a helpful reference for observing any lateral motion, as shown in figure 4.16 which highlights the exact superposition of the indent between 0 and 15 T. It was shown earlier, in figure 2.12, that the more utilitarian features of the SPM, such as the coarse motors, also performed as expected in high magnetic fields.

The Tuning Fork

The quartz tuning fork presents a more challenging problem as far as its interaction with the magnetic field. A brief collection of recent quotes from the literature should help illustrate the

[4] A small shift is visible between **a** and **b**. This is a result of reproaching the surface between scans using the coarse z motor, an action which usually causes small, $\sim$ 20 nm lateral displacement. Also, no drift is observed between **h** and **i**.

[5] In the last few images, a diagonal line can be seen between the center of the scan and the upper left corner indicating a strong tip-sample interaction.

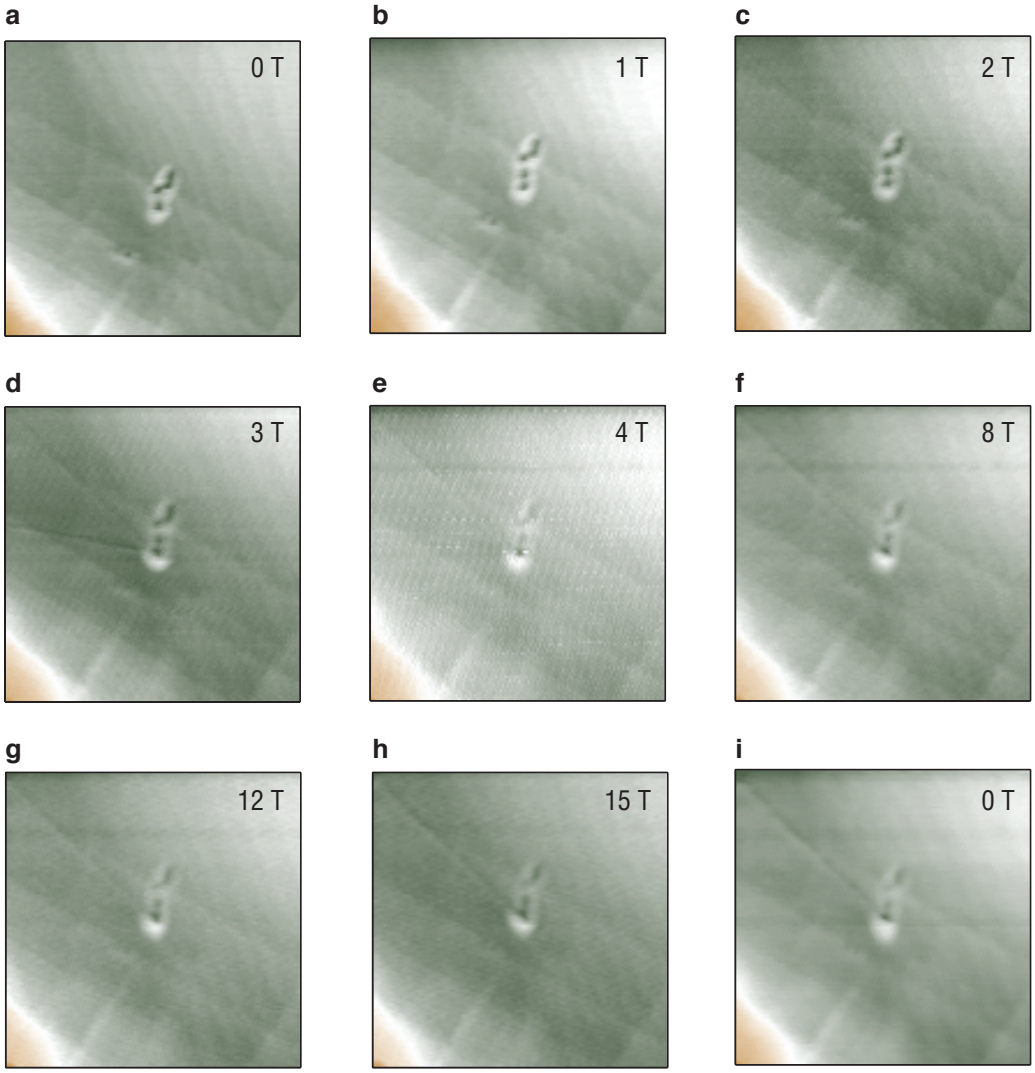

Figure 4.15: An array of topographic images of a KBr surface taken at increasing magnetic field strengths. The width of each scan is 745 nm in x and y and the z range is in the order of 10 nm.

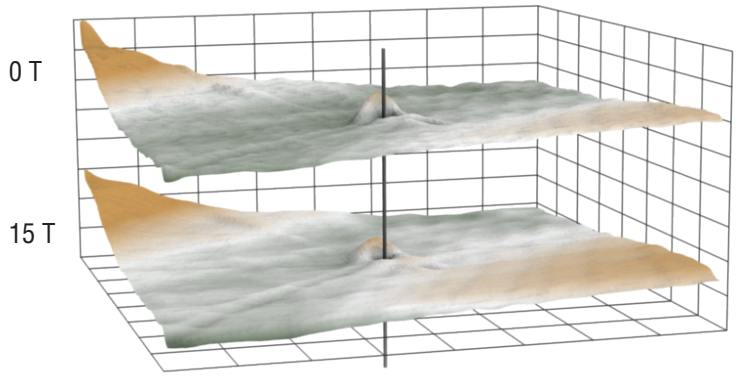

Figure 4.16: A vertically aligned pointer sits in the center of both indents at 15 T and 0 T

state of the question.

1. In addition, we measured the dependence of the resonance frequency on an external magnetic field in the range of 0 - 8 T. The frequency shift detected was smaller than 100 mHz.[133]

2. With increasing magnetic field the general trend is an increase in resonant frequency and a decrease in quality factor. Sensors typically show a linear increase in frequency of between 0.1 and 0.5 Hz/T at high field. The low field behavior varies between sensors and can show increasing and decreasing frequency as a function of field. The quality factor falls by approximately an order of magnitude between 0 and 10 T. Again, the low field behavior can be more unpredictable. It might be that ferrous material in the contacts or tuning fork leads is responsible for the behavior at low field.[134]

3. Since the vibrating element is a quartz crystal we might expect Eddy-current effects to be absent. However, the electrodes on the sides of the tuning fork tines probably account for the additional damping we see when a high magnetic field is applied in vacuum, although the damping does not quite vary as B^2 as one would expect for Eddy-currents.[135]

4. We have also performed preliminary measurements in a magnetic field of 1 T without noticing any change in the piezo-electric signal. Ramping the magnetic field creates however eddy currents in the contact pads. For this reason tip-sample distance control should be done at constant magnetic fields.[136]

5. Spectroscopy at a fixed point of the surface with sweeping magnetic field is difficult. The resonance frequency of the tuning fork is not found to shift significantly when the magnetic field is altered.[47]

6. They have the added advantage that they are very simple to use, they operate over the entire temperature range (from room temperature), and they are quite insensitive to magnetic fields.[137]

Clearly, there exists some differences in opinion regarding the performance of tuning forks in high magnetic fields. In general, reports seem to agree that there is some interaction between the magnetic field and the oscillating quartz tuning fork. Our experiments performed with the ULT-SPM show that is indeed the case, and will suggest a few possible explanations for this interaction.

The basic problem is the following. As the oscillating tuning fork is subjected to magnetic fields in z, both the resonant frequency and its quality factor shift with field strength. Figure 4.17 illustrates this between 0 and 15 T. Since the excitation voltage V_{exc} needed to maintain a constant amplitude will vary inversely with the quality factor, $Q^{-1} \propto V_{\text{exc}}$, we simply use V_{exc} when the amplitude controller is on as a measure of tuning fork dissipation, without having to take frequency sweeps and fit Lorentzian line shapes at each magnetic field value. Over the full range of the ULT-SPM magnet, these effects become considerable. A strong quadratic dependence is noted.

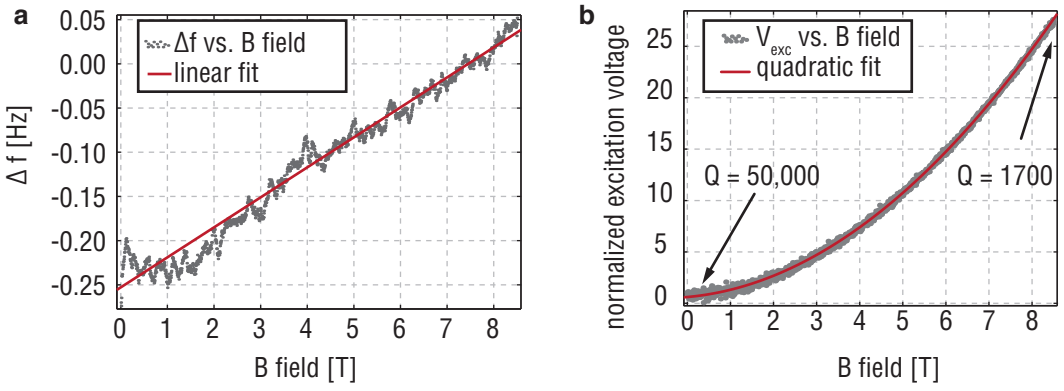

Figure 4.17: **a**: The resonant frequency of an oscillating tuning fork in the qPlus configuration when exposed to a magnetic field and **b**: the voltage excitation needed to maintain a constant oscillation amplitude, upon which the quality factors depends linearly, during the same ramping of the magnetic field. The circles are measured data points and the lines are quadratic fits to the data.

Several causes for this behavior have been proposed:

1. (Anti)Ferromagnetic metals in the tuning fork electrodes
2. Eddy currents in the tuning fork electrodes
3. Eddy currents in the Tungsten tip
4. Intrinsic dissipation of the quartz crystal

The first consideration requires analysis of the chemical content of the tuning fork, since the manufacturing details are not released to the consumer. Using x-ray analysis (EDX), on several different tuning fork models, we were able to ascertain the metal in the electrodes. Several types of metallic depositions were found, as described in table 4.1. We should not use TFs with a chromium adhesion layer, since the antiferromagnetism of chromium would certainly cause problems with the applied fields. However, despite restricting ourselves to non-magnetic materials, we still observe severe quality factor losses in the magnetic fields, as can be seen in the traces in figure 4.18, which were acquired with the Citizen CFS145 tuning fork which showed no chromium in the EDX spectra. Also of note in both **a** and **b** of figure 4.18 are the deviations from either linear or quadric form in the field dependencies, as seen by the features between 1 and 2 T. These features suggest a more complicated analysis of the damping is required.

Example Tuning Fork Electrodes		
Brand/Model Number	**Conduction Metal**	**Adhesion Layer**
Citizen American CFS145	Pd	Ti
Seiko VT 200F	Au	Cr
Citizen American CFV206	Ag	Cr
ECS INC 327-8-14	Pd	Ti

Table 4.1: A sample of the various metals found in the tuning fork electrodes.

Though not directly related to tuning forks, we can borrow from the work done on micro/nanomechanical resonators, since the material dimensions are close in scale and the materials are similar in class. Referred to as the magnetomotive [138] detection scheme, applying an ac current to the resonator in a constant magnetic field allows for actuation of the resonator, via the Lorentz force on the moving charges, as shown in figure 4.19. A consequence of this tactic is a noticeable damping of the resonator due to the moving charges in a magnetic field. While the piezoelectric properties of the tuning fork preclude the need for magnetomotive actuation or detection, there still exists an ac current on the tine while it is in motion, thus a related analysis could be applied to the tuning fork losses, especially since the magnetomotive scheme is found to lead to increased dissipation quadratic in B.

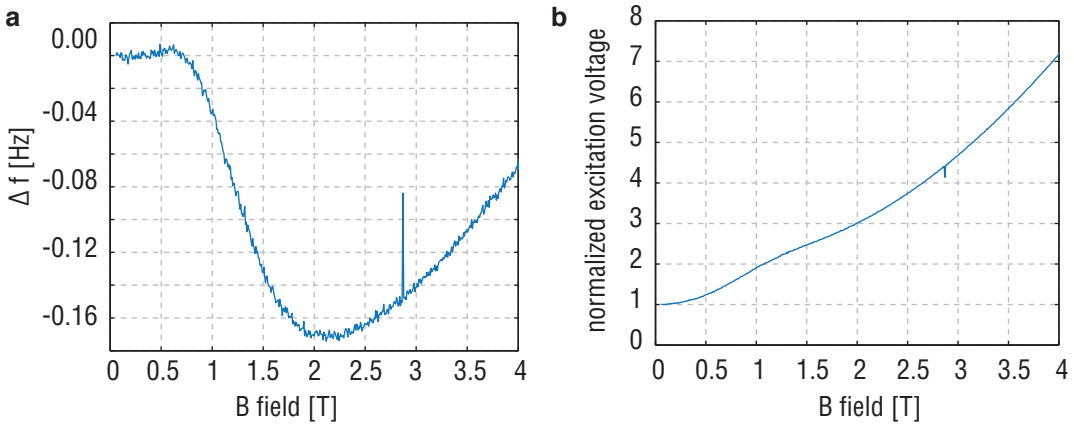

Figure 4.18: **a**: The frequency shift from a CFS145 tuning fork in a magnetic field. **b**: The corresponding excitation voltage needed to maintain a constant amplitude of oscillation.

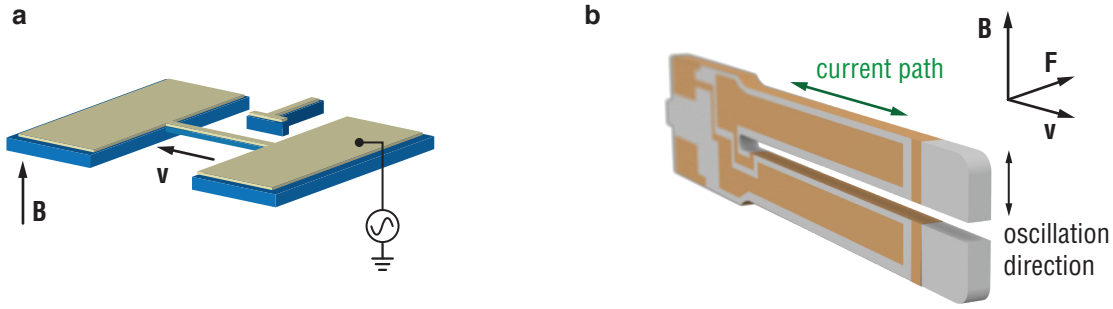

Figure 4.19: **a**: A nanomechanical resonator in the style of [139] wherein magnetomotive effects have been observed. **b**: A quartz tuning fork oscillator with a similar configuration making possible magnetomotive damping effects.

If we consider the various sources of dissipation for a resonator, we expect a combinational form that follows:

$$\frac{1}{Q_{\text{total}}} = \frac{1}{Q_1} + \frac{1}{Q_2} + \frac{1}{Q_{\text{L}}} + \ldots \tag{4.17}$$

Thus, the observed quality factor, Q_{total}, will be limited by the smallest Q in the summed terms. Essentially, there will exist a dominant dissipation cause that provides a lower limit, Q_{L}, on the quality factor of the resonator. The magnetomotive effect in the resonators discussed above has been shown to lead to a Q_{L} quadratically dependent on B, which will place a limit on the Q_{total} for the oscillator. However, the analogy to the magnetomotive scheme is not entirely appropriate for the quartz tuning fork, since the displacement vectors of the two oscillators are not in the same direction relative the magnetic field. The mode of excitation for the tuning fork is parallel to the magnetic field, as seen in figure 4.19, while the usual magnetomotive scheme requires oscillations perpendicular to the applied field. It is possible that some losses do occur through this mechanism, since the tuning fork is free to oscillate in the perpendicular direction, however, the are likely small since the two modes are well separated. Thus, we cannot directly apply the same formulation.

Another possibility for the damping arises from the piezoelectric effect itself. Since the tuning fork can be thought of as a current source, any resistance seen by the generated currents will create a dissipative component to the system. This is related to the concept of piezoelectric shunt damping in which either passive or active components modify the response of the crystals. As seen in figure 4.20, adding a series resistor can modify the quality factor. Thus, if the resistance of the tuning fork electrodes were to change as a function of the magnetic field, then this modulation should manifest in the measured Q. Since the electrodes on the tuning fork are thin-film metals, there exist several possible mechanisms for a magnetic field dependent resistivity in the films. These include consequences of the classical Hall effect or more intricate electron interactions. However, most of the documented resistance changes for the appropriate films are small, usually less than 1%.[140, 141] Thus it is unlikely that the change in resistance of the tuning fork electrodes in a magnetic field is the main source of field dependent dissipation observed in the tuning fork.

Eddy current losses are another likely candidate for loss in the oscillating cantilever. In this case, currents could be generated by the change in flux as the tip or tuning fork electrodes rotate slightly in the magnetic fields. Dissipation due to this mechanism will depend on the geometry and resistivity of the etched tips.

Given the confusion and mixed results shown in the quotations above, it seems that further investigation of this phenomenon would yield useful results for the tuning fork based scan probe community. It has also been shown elsewhere that nanomechanical oscillators being developed for other applications suffer from similar damping in magnetic fields, perhaps due to

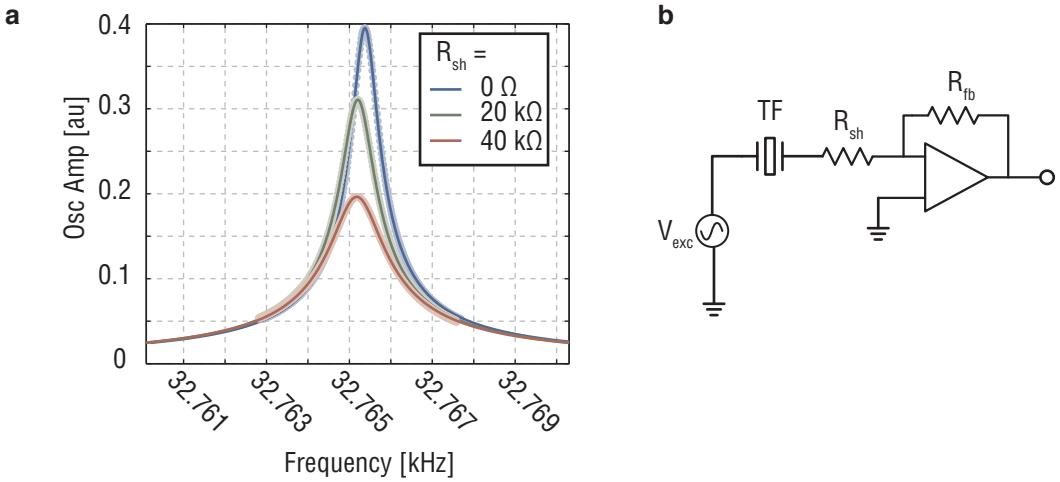

Figure 4.20: **a**: Effect on Q after adding a series resistor to the tuning fork electrode. The quality factors obtained from the the fitted Lorentzians indicated a decreased from 51000 to 40000 to 25000 for the three curves shown. **b**: Schematic showing the location of the resistor, R_{sh}.

charged two level systems or dipoles inherent in the oscillating material.[124] Thus, it is likely that a combination of these factors plays a role in the damping of the tuning fork. Further work will be needed which focuses on these issues.

4.5 Chapter Conclusions

Thus we have documented the operating characteristics of the microscope. The scans at 15 T represent the highest field force microscopy images to date, and inspire many possible experiments for the future of the ULT-SPM. We have shown several different modes of operation for the microscope, indicating its versatile application. The microscope has not quite reached base temperature, 50 mK, yet, however, a few modifications are underway at the present time which should help us reach it. Additionally, the magnetic field induced effects on the quartz tuning fork were discussed and compared with results from micro and nanomechanical oscillators.

CHAPTER 5

CLEAVED EDGE OVERGROWTH

This chapter follows our investigations of a specialized condensed matter system in which we marry the low temperature capabilities of the apparatus with the scanning probe, thereby demonstrating its effectiveness as a tool for further explorations of related structures. We'll discuss the nature of the sample in depth and show a unique characterization of it performed by the tuning fork based force sensor, highlighting the extreme sensitivity of the instrument.

5.1 Sample Growth

The cleaved edge overgrowth (CEO) method was developed in 1990 at Bell Labs.[142] Using molecular beam epitaxy (MBE) techniques established over the preceding three decades, the CEO offers a new playground for low dimensional transport measurements.

Molecular Beam Epitaxy

MBE allows for the creation of custom nanostructures via the deposition of layered crystal planes of specific materials. The layers are chosen to engineer a custom crystal with desired electrical properties. In the case of low-dimensional nanostructures, specifically the two-dimensional electron gas (2DEG), the MBE approach has been found to be exceedingly useful.[143]

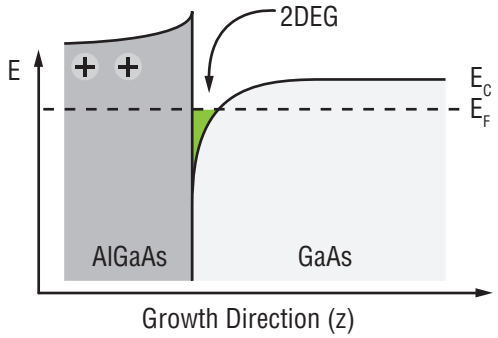

Figure 5.1: Energy diagram of the modulation doped AlGaAs/GaAs heterojunction showing the region where the 2DEG forms as the conduction band, E_C bends below the Fermi level, E_F.

Briefly, the 2DEG is created in these samples by energetically confining electrons to a planar region which is smaller than the wavelength of the electron.[1] Thus, motion is restricted in the narrow dimension, z in this case (see figures 5.1 or 5.3 for coordinate axes). The confinement is due to the modulation doping in which Si donor atoms are added to the AlGaAs side of the heterojunction during growth, approximately 100 nm away from the juncture.[144] Electrons from the dopant ions will transfer from the AlGaAs to the GaAs. The electric fields associated with this process are strong enough to cause band bending on the GaAs side of the junction, as seen in figure 5.1. At low temperatures, the triangular shaped potential shown becomes the confining region for the electrons, which is very small in the z axis, but limited in x and y only by the sample edges.[143] The exact details of each 2DEG will depend on the specifics of the growth parameters and can vary significantly between samples.

The Cleaved Edge Overgrowth

The preparation of the CEO sample involves two distinct phases of MBE deposition.[145, 142] Schematically shown in figure 5.2, the sample consists of the heterojunction described above, which creates the two dimensional electron gas (2DEG) with a MBE defined electrode opposing one edge of the original sample. Figure 5.2**a-c** highlights the essential growth steps, from the original 2DEG to the final growth of the tunneling barrier and edge electrode.

The notable feature of the CEO sample is the barrier/electrode system that now addresses one edge of the 2DEG. In general, electrically contacting a 2DEG involves diffusing metal from the surface of the sample into the GaAs layer. Such contacts create Ohmic contact to the 2DEG and are indispensable for the standard transport measurements used in most Quantum Hall investigations. However, we can also address the 2DEG via a tunneling current. This is the purpose of the edge electrode.

5.2 Why the edge?

Quantum Hall Overview

To appreciate the specific geometry of the CEO sample, we should come to an understanding of what makes the sample edge special in the context of quantum Hall physics. Recalling the classical formulation for charged particles moving with velocity v_{drift} in a magnetic field, B, the classical Hall effect[146] arrises when the charge carriers, (with charge q) in a rectangular sample deviate from their longitudinal motion along the length, x, due to a perpendicular force as expected from the Lorentz force law:

$$\mathbf{F} = q\mathbf{E} + q(v_{\text{drift}} \times \mathbf{B})\,. \tag{5.1}$$

[1] This value is dependent on the electron density, but can be estimated to be in the order of 100 nm.

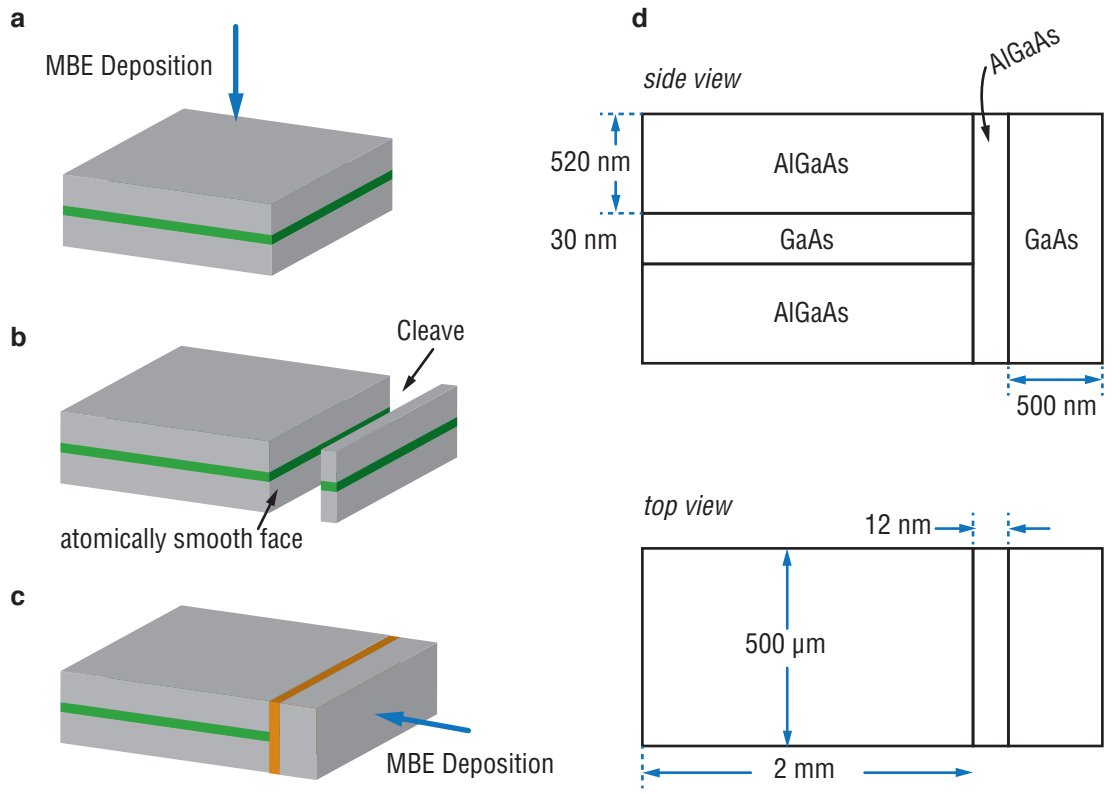

Figure 5.2: Schematic illustrating the two primary phases of the sample growth. **a** shows the preliminary deposition scheme in which the 2DEG is created. This is followed by **b**, wherein a cleave is introduced on one side, creating an atomically defined edge to the 2DEG. **c** shows the subsequent growth of the edge electrode by performing the MBE deposition perpendicular to the original deposition vector. **d**: Top and side views clarifying the dimensions of the sample and major material differences within.

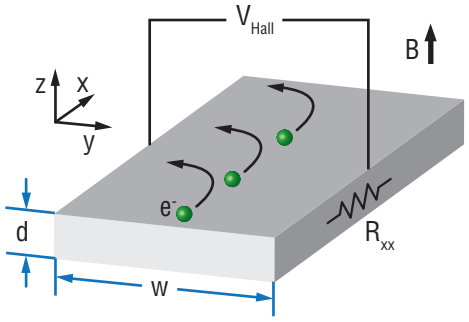

Figure 5.3: The classical Hall effect geometry of a conductor and currents in a magnetic field

This deviation in turn creates a potential difference in the y direction, V_{Hall}. An equilibrium will be established when the force from this potential equals the Lorentz force, or:

$$F_B = F_E \;\Rightarrow\; e v_{\text{drift}} B = e V_{\text{Hall}}/w \,. \tag{5.2}$$

The current through the sample will be given by the number of electrons per unit volume, N, passing through the area $w \times d$, per second:

$$I = N e v_{\text{drift}} d w \,, \tag{5.3}$$

which in combination with (5.2), gives for the Hall Voltage:

$$V_{\text{Hall}} = \frac{IB}{Nde} = \frac{IB}{ne} \,, \tag{5.4}$$

where we have now used the 2D density $n = Nd$. From Ohm's law, $V_{\text{Hall}} = IR_{\text{xy}}$ we can establish the Hall Resistance, R_{xy}:

$$R_{\text{xy}} = \frac{B}{ne} \,, \tag{5.5}$$

which we can see is only a function of the elemental charge, e, the 2D charge density, n, and the applied magnetic field.[2] This captures the essence of the classical Hall effect. However, at low temperatures and magnetic high fields, experimental observations showed there was more involved.[20]

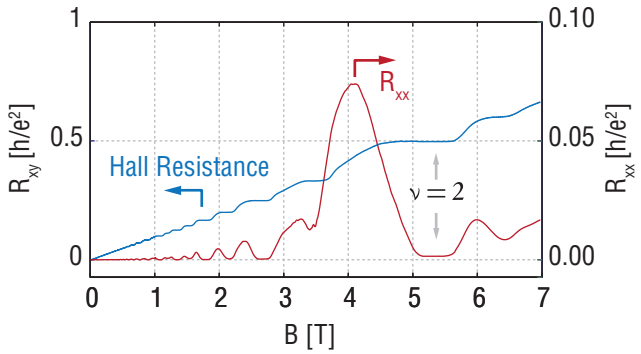

Figure 5.4: A Hall trace taken on the ULT-SPM fridge at 300 mK on a standard 2DEG sample, without the cleaved edge overgrowth.

The Hall resistance was experimentally found to contain plateaus which appeared at quantized values while the longitudinal resistance, R_{xx} showed peaks and valleys, with zero resis-

[2]Regarding the subscripts: R_{xy} denotes the Hall resistances, sometimes labeled as R_{Hall}. The longitudinal resistance is labeled as R_{xx}.

tance regions corresponding to the plateau positions, as seen in an example transport measurement shown in figure 5.4. These features are due in part to the quantized energy levels of electrons in magnetic fields. The energy levels, Landau Levels (LL) are given by:

$$E_N = (N + 1/2)\hbar\frac{eB}{m^*} = (N + 1/2)\hbar\omega_c \,, \tag{5.6}$$

where m^* is the effective mass of the electron. We can describe the degeneracy of the LLs by considering the number of available states per LL as:[147]

$$n_B = \frac{eB}{h} \,. \tag{5.7}$$

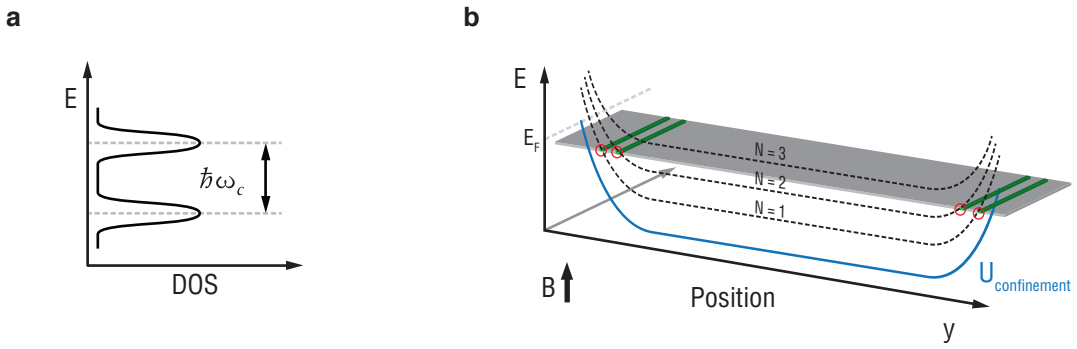

Figure 5.5: **a**: Landau Levels in B field. **b**: Schematic showing the orientation of the confinement potential and its influence on the Landau Levels. The red circles indicate crossing of the LLs with the E_F and the resulting quasi-1D conduction channels.

When the ratio between the number of available electrons n and n_B is an integer value, the Fermi energy, E_F, will be located in between two levels, and the Hall plateaus will be visible and the R_{xx} will vanish. This ratio is referred to as the filling factor, $\nu = n/n_B$. We can express (5.5) in terms of ν and arrive at:

$$R_{xy} = \frac{1}{\nu}\frac{h}{e^2} \,. \tag{5.8}$$

The values of the plateaus in R_{xy} were found to correspond to field strengths where ν took on whole number values. This in part characterizes the integer quantum Hall effect. A fuller treatment would introduction the effects of disorder induced scatterers to account for the extended widths of the plateaus.

While much has been left out of this explanation (electron spin for example), it does offer enough to help highlight what is interesting about the edge. If we consider several of the lowest

LLs, as in figure 5.5**b**, this time shown as a function of position, y, we can observe that at the edges of the sample, there will be a confinement potential which bends the energy bands upward near the edge. Thus, due to the upward bending, the E_F will cross the LLs, giving rise to conduction channels, or edge states.[23] For each crossing of a LL with the E_F, a conduction channel will be formed. These channels can be treated as a 1D conductors which adhere to the Landauer-Büttiker formulation for conduction in one dimension. For each conduction channel, there will be a e^2/h increase in the conductance.

The above discussion forms the basis for what can be called the *edge state* explanation of the QHE. It is widely used as the conceptual framework for many quantum Hall related investigations since its introduction almost 30 years ago.[23] Yet, it does fail to take into account several other aspects of the QHE. For example, electron screening is not present in this description. It has been shown that screening will lead to a more complicated picture of the edge currents in which alternating strips of incompressible and compressible fluids will form at the edges.[148]

The electron density will vary with position in the region of the edge of the 2DEG, as seen in figure 5.6**a**. As the magnetic field varies, so will the electronic density of states (DOS). Thus, regions of local filling factors with integer values will form. In these regions the electron screening will be absent. These are the incompressible regions, or strips. In between the incompressible strips are the regions of non-integer local filling factor regarded as metallic, or compressible, where screening leads to a uniform potential across the region. In figure 5.6**b** and **c**, a schematic representation of incompressible strip view is shown. The orange strips are termed incompressible, (inC), as their density is fixed. The green, labeled C, are the compressible strips. The bending of the electrostatic potential is thus a consequence of the edge electrostatics and adds features to the current distributions at the edge.

Experimental approaches attempting to verify the existence of incompressible strips have been demonstrated recently. In particular, with low temperature scanning probes, potential profiles of narrow 2DEGs in high fields have been shown to exhibit structures that would correspond to the incompressible/compressible strip analysis.[149, 150] By measuring the potential drops in proximity to the edge, spatial information about the distribution of the currents can be obtained. Alternative methods of probing the edge, for example using many diffused contacts along the edge to reveal thermodynamic properties, are currently being developed as well.[151]

The general picture presented in figure 5.6 is based on 2DEG edges which are formed via gate induced depletion regions. As was observed earlier, the CEO sample is somewhat different in that the edge, or boundary of the 2DEG, is defined via an atomically precise cleavage line. It has been proposed that the sharpness of the cleaved edge could lead to a different view of the edge current structure, since the changes in the density near the boundary will be much more abrupt.[152]

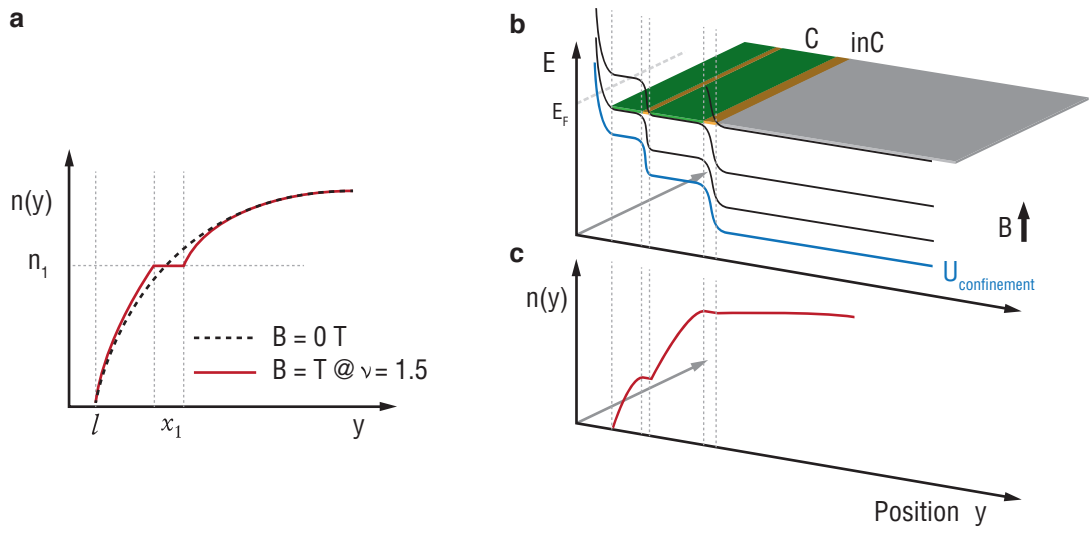

Figure 5.6: **a**: Electron density as a function of position away from the edge in zero magnetic field (dashed line) and with a field corresponding to a bulk filling factor of 1.5 (solid line). **b**: Schematic of the strip formation near the sample boundaries. **c**: Electron density $n(y)$ near the edge showing the corresponding incompressible regions. (Adopted from [148])

Edge Tunneling

The above discussion has been limited to the integer quantum Hall effect (IQHE), and in doing so has left out the more complicated fractional quantum Hall effect (FQHE), where states at non-integer filling factors lead to even more exciting features in magnetotransport measurements. Still a much studied condensed matter system, the FQHE requires the inclusion of many-body interactions to explain its departure from the above discussion.[143] The cleaved edge sample was designed for studying the richer physics of the FQHE edge states by allowing a tunneling current between the edge electrode and the edge of the 2DEG.

Other devices have been conceived in which tunneling events between two edge states were permitted via a lithographically defined gate induced constriction.[153, 154] However, since a gate defined constriction inherently suffers from smooth potential barriers, shown conceptually in figure 5.7, as a result of the distance between the 2DEG and the gate, inconsistent results were reported.[155] And so the cleaved edge sample was developed, offering an atomically defined edge where the confinement potential was much sharper.[152] Many interesting results have been reported using the CEO sample and thus prompted our investigations with the SPM, to which we now turn. [156, 155, 157, 158]

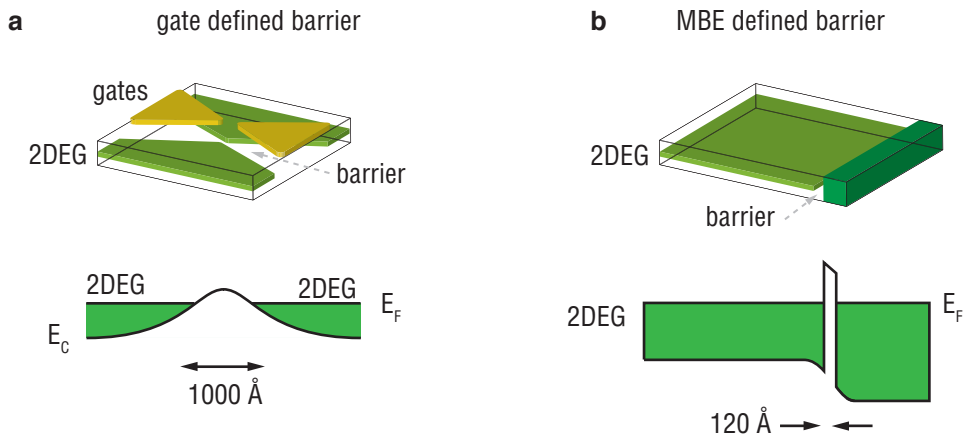

Figure 5.7: **a**: A gate defined tunneling barrier and potential profile showing the wide width of the barrier. **b**: The MBE method in which the barrier is defined atomically. After [159]

5.3 Initial Characterization

Physical Characterization

Unlike tabletop AFM systems, just finding the area of interest in a sample can be difficult in low temperature instruments. Figure 5.8 shows a representative view of the optical access to the scanner and sample area *before* cooldown. Even at this point, orientation of the tip and sample relative to each other is difficult, due mostly to the geometry of the AFM which offers little direct line of sight access by optical means.

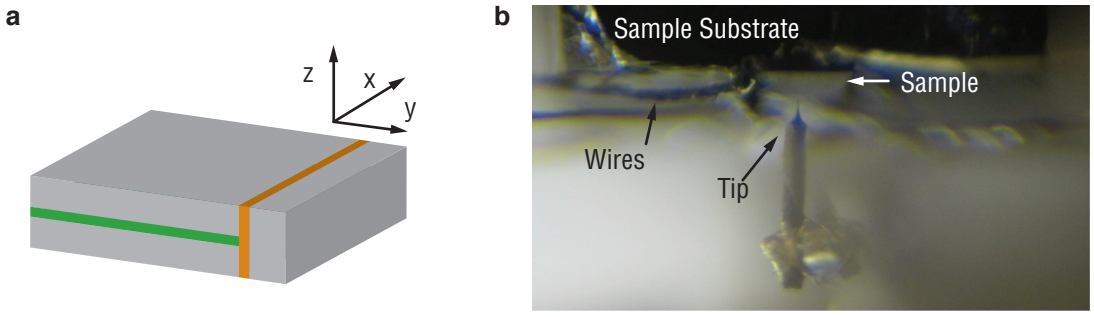

Figure 5.8: **a**: The coordinate axes for the cleaved edge sample. **b**: The optical view available before cool down showing the tip and the sample.

Once the positions are satisfactory at room temperatures, the cooldown commences. After

which, we must again confirm that no major dislocations have occurred.[3] While spatially uniform samples like the InAs quantum dots are much easier to deal with in this regard, samples like the CEO provide logistical challenges. Since our area of interest is in fact the very edge of the sample, we must be certain that the tip is indeed over the sample, rather than just a few microns away over the abyss. Here we must rely heavily on the capacitive position sensors to help guide the exploration.

Thus the first step towards any investigation of the edge in this system will naturally be to *find the edge*. (The coordinate system used for the CEO sample is defined in figure 5.8.) AFM topography is not really the best way to accomplish this, since the settings of the feedback loop will cause the tip to extend until it reaches the surface, which is fine when there is a surface, but will lead to problems in the region past the edge, where there is no surface. We instead rely on EFM techniques outlined in section 4.3. By keeping the tip fixed above the surface and applying a dc bias (∼10 V) between tip and sample, we can search for the edge by looking for an abrupt change in the Δf signal that occurs when the tip is no longer above the surface. This change should be uniform in the x axis since the edge is very well defined line extending for 500 μm. Figure 5.9 shows an example of this technique where the edge location is assessed via the EFM signal, thus preventing the tip from extending far past the edge.[4]

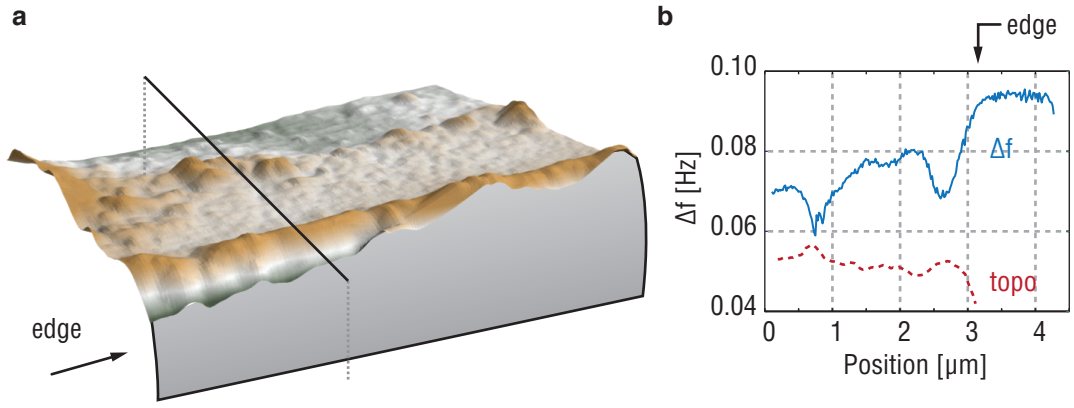

Figure 5.9: **a**: Topographic image of the area *near* the edge, taken in standard NC-AFM mode, without actually going over the edge. The black line shows the approximate line the tip traveled to obtain the electrostatic information shown in **b**: A line trace of the same region taken using the EFM technique. Note the flat section of the curve at the right side of the plot where there is little coupling between the tip and the sample, since the tip has gone over the edge.

[3] In depth measurements of such dislocations have not yet been performed, yet preliminary findings suggest that thermally related position deviations are in the order of 10 μm.

[4] While it is possible to let the tip pass over the edge and continue in feedback, it would be considered a risky maneuver since it drastically increases the likely hood of a tip-crash or a bent probe.

Also of interest in the preliminary investigations is the perpetual appearance of a slight ridge just near the edge. This feature is visible in nearly every scan taken over the edge. Its existence was confirmed using scanning electron microscopy (SEM) of the edge, after the experiments were concluded. Figure 5.10 shows an SEM image of the edge in which the roughness near the edge is visible. While this feature only makes characterization via AFM more involved, it might be of interest from a materials standpoint.

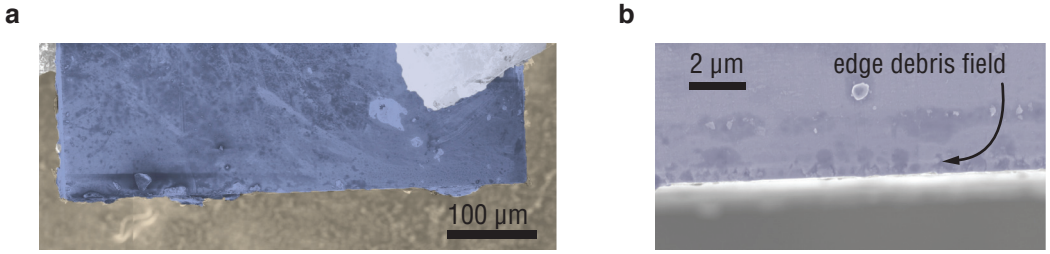

Figure 5.10: False color SEM images of the edge region. **a**: Large area view of the edge. **b**: Smaller range area showing the roughness near the edge.

Electrical Characterization

Electrical characterization of the 2DEG and tunneling barrier is another prerequisite to performing any further investigation. The indium contacts used to characterize the transport properties of the 2DEG are usually robust, however, since the AFM contains many moving parts which might dislodge a small wire, we must verify their integrity before proceeding. Parameters such as the electron density should also be determined.

To test the edge electrode and tunneling barrier, we performed a standard dV/dI trace to measure the resistance between the 2DEG and the edge as a function of magnetic field.[5] As seen in figure 5.11**a**, the edge resistance, R_{tun}, increases exponentially with magnetic field. This is a result of the magnetic length, l_B, of the electrons:

$$l_B = \sqrt{\frac{\hbar}{eB}}, \tag{5.9}$$

which in high fields will limit the conductance when this length becomes smaller than the barrier width.[159]

To measure the electron density, we can rely on the relationship between the filling factor and magnetic field:

$$B_\nu = \frac{1}{\nu}\frac{nh}{e}, \tag{5.10}$$

[5] Appendix C.2 contains details of these and other measurement schemes.

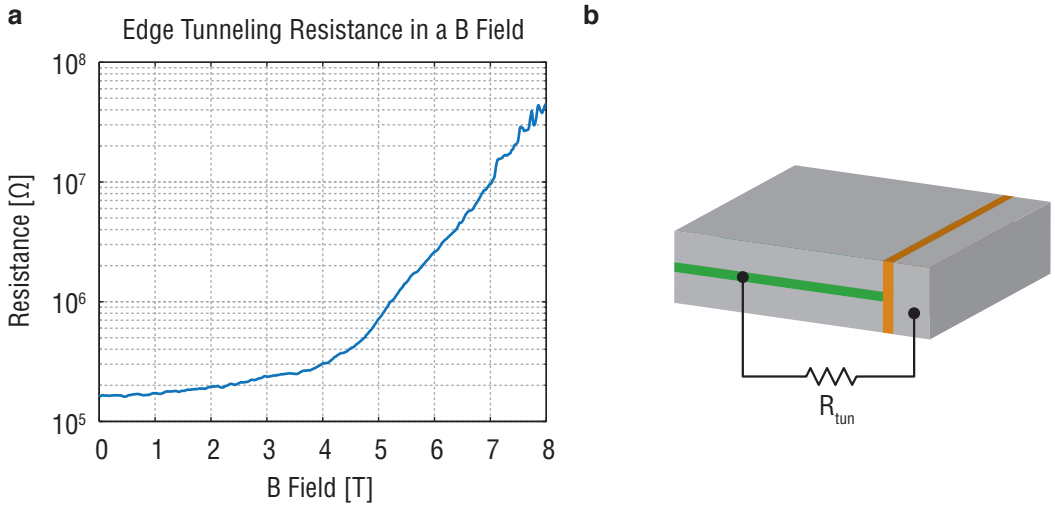

Figure 5.11: **a**: The tunneling resistance between the edge and the 2DEG in a magnetic field. **b**: The schematic of the measurement.

which we see contains only fundamental constants, e, the charge of the electron, and h, Planck's Constant in addition to the filling factor ν, the electron density n and the magnetic field B_ν. Thus, using a trace of the Hall Resistance from which we can obtain the filling factors, we can arrive at an estimate of the electron density. Figure 5.12 shows a Hall Resistance trace in **a**, and the corresponding plot of the filling factors plotted against the inverse magnetic field. Extracting the slope and using (5.10) provides an estimate of $1.03 \pm .02 \times 10^{11}$ cm^{-1}. As this value can change between cooldowns, we are only concerned with obtaining a rough estimation to ensure we are within the expected experimental parameters.

5.4 Scanning Potential

Exciting the Tuning Fork via the 2DEG

To further characterize the CEO sample, in a novel manner, we applied the technique of ac-Electrostatic Force Microscopy (ac-EFM), historically referred to occasionally as *Scanning Potential Microscopy*. This extension of the more standard EFM technique involves using ac signals applied to the 2DEG to excite the tuning fork, rather than mechanically via the scan piezotube or electrical via the TF electrodes. Combining this excitation method with the scanning probe makes for an exciting and powerful alternative microscopy technique.[63, 160]

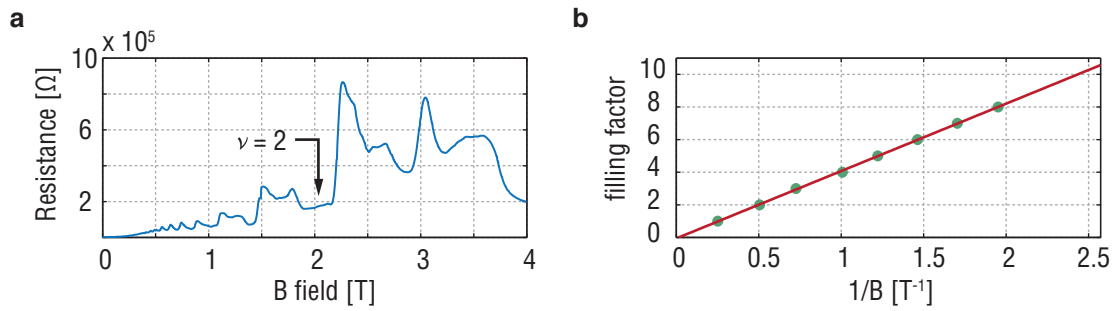

Figure 5.12: **a**: A two terminal Hall resistance measurement verses magnetic field. **b**: The extracted filling factors plotted against inverse magnetic field.

Origins of ac-EFM

Considering the tip and sample as a capacitor, we can formulate some expectations for the behavior of the tip in relation to the electrostatics of the system. The energy stored in a capacitor is given by

$$U_{\text{cap}} = \frac{1}{2} C V^2 \tag{5.11}$$

where C is its capacitance and V the potential difference.[161] Together, the tip and sample form a capacitive system with a capacitance given by their geometry. The voltage term in (5.11) accounts for the tip and sample biases and can be replaced with $V_{\text{t-s}}$.

The force on the tip can be expressed generally as the spatial derivative of the potential:

$$F = -\frac{d U_{\text{tot}}}{dz}, \tag{5.12}$$

which in the case of this capacitive model will lead to an electrostatic force:

$$F_{\text{ES}} = \frac{1}{2} \frac{dC}{dz} V_{\text{t-s}}^2 . \tag{5.13}$$

While the capacitance,C, and its derivative are given by the geometries of the system and material considerations, and are therefore not readily changed, the $V_{\text{t-s}}$ is easily modified. It is this term that we exploit in the techniques that follow.

Known as ac-electrostatic force microscopy (ac-EFM), this technique allows for the extraction of local electrostatic potential via the dynamics of the cantilever. To understand the origins of this measurement technique, consider the components of the $V_{\text{t-s}}$ term:

$$V_{\text{t-s}} = V_{\text{ac}} + V_{\text{dc}} + V_{\text{CPD}} . \tag{5.14}$$

V_{dc} and V_{ac} are applied voltages between the tip and sample, which are either constant, dc, or modulated, ac. V_{CPD}, the contact potential difference (Φ henceforth), is the potential given by the difference in work functions between the tip material and the sample. Expansion of $V_{t\text{-}s}$ in (5.13) will lead to several components summing to give the total force, which can be grouped by their respective frequencies. If $V_{ac} = V_{exc}\cos(\omega t)$, we'll obtain a force acting at three frequencies: dc, ω, and $2\times\omega$:

$$F_{dc} = \frac{1}{2}\frac{dC}{dz}\left[(V_{dc}+\Phi)^2 + \frac{V_{exc}^2}{2}\right] \tag{5.15a}$$

$$F_{ac} = \frac{dC}{dz}\left(V_{dc}+\Phi\right)V_{exc} \tag{5.15b}$$

$$F_{2ac} = \frac{1}{4}\frac{dC}{dz}V_{exc}^2 \tag{5.15c}$$

The force given in (5.15b) is the key to ac-EFM. If we choose ω to be equal to the resonance frequency of the cantilever, ω_0, this force will induce oscillatory motion in the cantilever, the amplitude of which will be given in part by the force applied. Local deviations in the potential will therefore be apparent in the amplitude response of the cantilever (provided the Φ and dC/dz terms are constant or accounted for). We can ignore the component given in (5.15c), since it acts at twice the resonance of the cantilever which will produce negligible effects on the tuning fork dynamics.

Figure 5.13**a** shows the basic scheme for ac-EFM. Usually the tip is held a short distance away from the surface, ~10 nm, while the excitation voltage, V_{exc} is applied to an electrode on the sample. The PLL or a lock-in amplifier is used to detect the induced oscillations in the tuning fork. As expected the tuning forks responds with a Lorentzian line shape if the excitation frequency is swept through the resonance, as shown in figure 5.13**b**.

To verify that this signal is indeed originating from the buried 2DEG, the force should be distance dependent. That is, increasing the tip-sample separation should result in a decrease in oscillation amplitude. We confirmed this by simply repeating the above measurement at many lift heights, as shown in figure 5.14.

We should also note an important term in (5.15b), V_{dc}. By adding a dc voltage to the ac excitation signal, we can increase the force on the tuning fork, and thereby increase the oscillation amplitude. The above plots in figure 5.14 were acquired with a 10 V dc potential applied in addition to the ac excitation signal. We can further verify (5.15b) by examining the effect of the dc potential applied between the tip and sample. Shown in figure 5.15 is the tuning fork response to a large range of tip-sample biases. The V shape is given by the inclusion of the linear $V_{t\text{-}s}$ term in (5.15b). The minimum could not be recorded clearly since the tuning fork response was too small without the dc bias. However, extrapolating the two arms of the V affords us an estimate of approximately 3 V. A quick comparison with the maximum of the

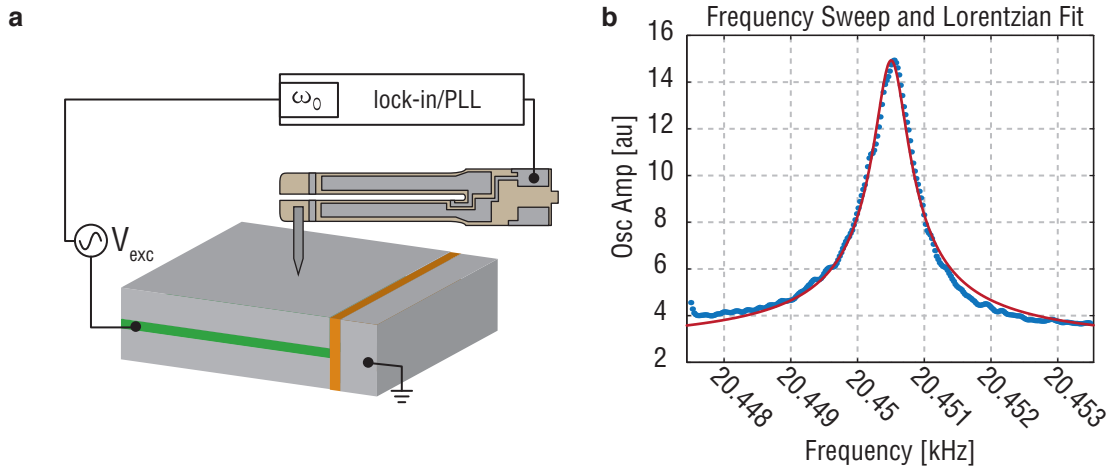

Figure 5.13: **a**: The essential ac-EFM excitation scheme in which an ac potential is applied to the sample and through capacitive coupling excites the tuning fork. **b**: An example frequency sweep taken via this method showing the expected Lorentzian line shape of the resonator response. The slight deviation from the fit is likely due to a small parasitic capacitance coupling between the tuning fork electrodes and the excitation signal.

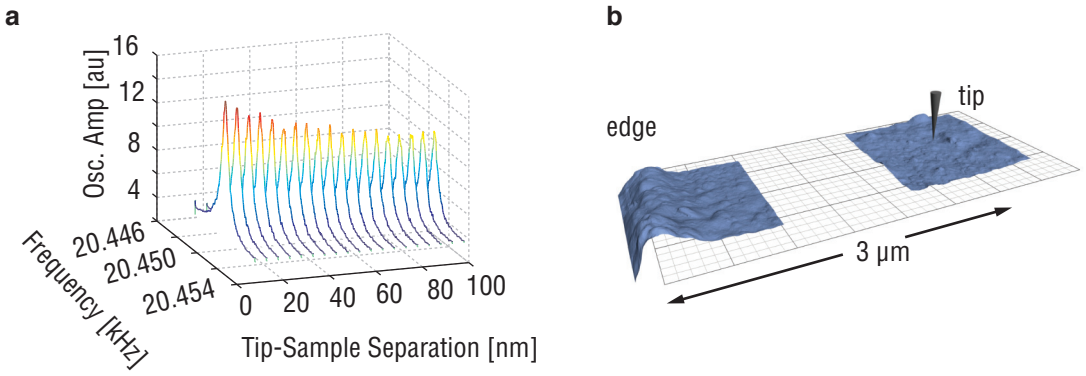

Figure 5.14: **a**: Waterfall plot showing the distance dependence of the cantilever response. **b**: The position of the tip with respect to the edge, assuring us that we are indeed over the 2DEG and not suffering from complications due to the location of the edge.

force gradient signal, the Δf of the cantilever due to changing the tip-sample bias, also plotted in figure 5.15, indicates a discrepancy. The CPD, Φ, is measured by the maximum of the parabola acquired from a tip-sample bias sweep. From the data shown in figure 5.15, this corresponds to about 1 V. Mismatches between these values have been reported elsewhere and are likely attributable to free charges on the surface.[162] This is entirely plausible in our case, since the surface was often found to be contaminated with unknown debris left over from the sample preparation process.

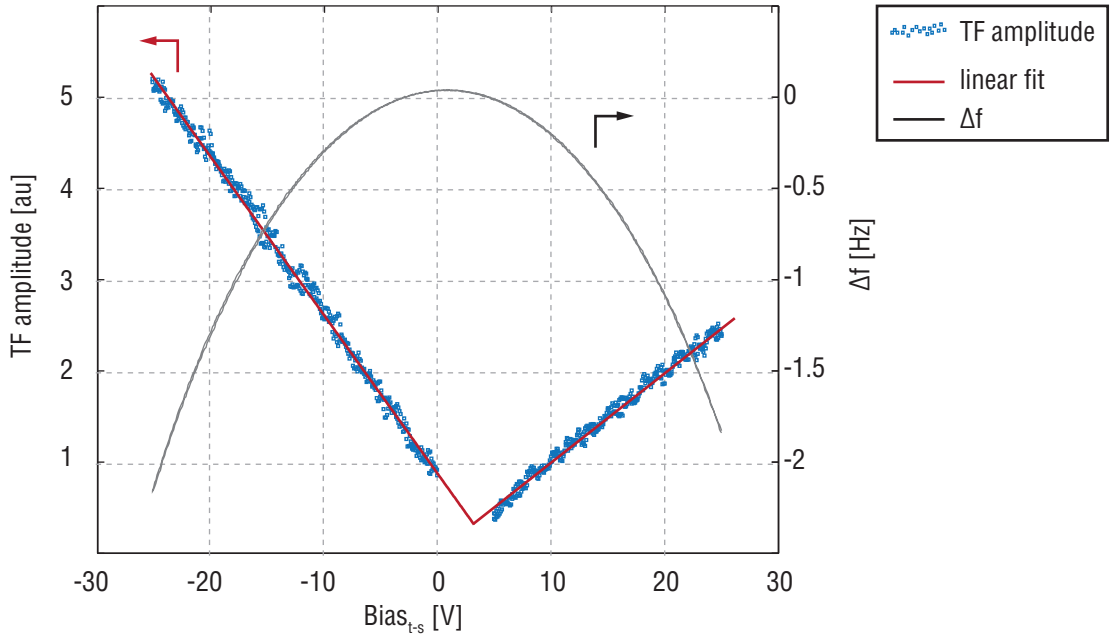

Figure 5.15: By applying a dc bias between the tip and sample, the force on the tuning fork in the ac-EFM mode is increased linearly. Also shown is the resulting resonance frequency shift, quadratically dependent on the $V_{t\text{-}s}$ as expected from the dc bias term in (5.15a).

Spatially Mapping the Potential

Once we are confident that the tuning fork excitation is indeed a consequence of the applied ac signal on the 2DEG, we can apply the scanning action to obtain information as a function of position. The first step is to take measurements along a line perpendicular to the edge. Starting approximately 2 μm away and passing over the physical edge will ensure we cross the interesting 2DEG edge.

Procedurally, the measurement was first taken by performing frequency sweeps ($f_0 + / - 2.5$ Hz) at many points in the y direction. Figure 5.16**a** shows a compiled surface formed by these

resonance curves aligned with the topography of the area of interest. We note that the signal decays when the TF has passed over the edge and is therefore no longer above the surface.[6] The same data is presented in **b** without the topography. The amplitudes of oscillation in the tuning fork data can be considered in arbitrary units, though, they are in the order of several angstroms.

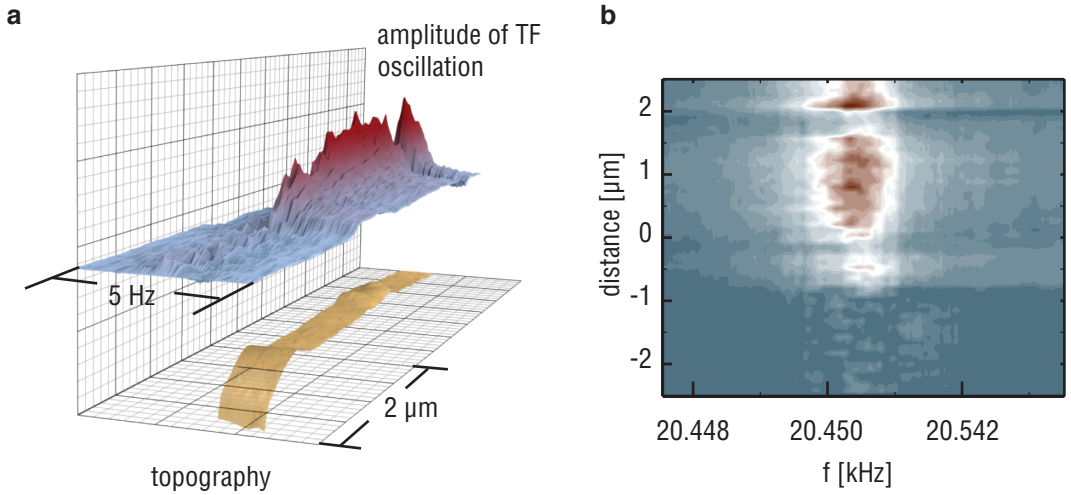

Figure 5.16: **a**: 3D image of the frequency response of the tuning fork as it passes over the edge. **b**: The same data as in **a**, but plotted without the corresponding topography. The color scale is in arbitrary units, with red being a large response and blue representing the non-excited tuning fork signal.

To speed up data acquisition times, and take advantage of the electronics developed for the SPM, we can use the PLL to lock the frequency of the excitation signal to the resonance of the tuning fork. In this case, we leave the amplitude controller unlocked so that the local potential from (5.15b) is reflected in the tuning fork amplitude, otherwise, the excitation signal to the 2DEG will be increased to compensate for losses, which could lead to destructive heating induced effects on the Hall states.

Figure 5.17 shows the measurement of the tuning fork oscillation amplitude taken over the edge of the sample while being excited through the 2DEG. The ac signal was kept constant at 75 mV on the 2DEG, while the dc bias was shifted to 5 different values as described in the legend. As expected from (5.15b), increasing the dc bias leads to a multiplicative increase in the signal. The topography over which the scan was performed is shown in the gray background.

[6]The frequency sweeps have been compensated to remove small parasitic capacitance artifacts which lead to deviations in the Lorentzian line shape.

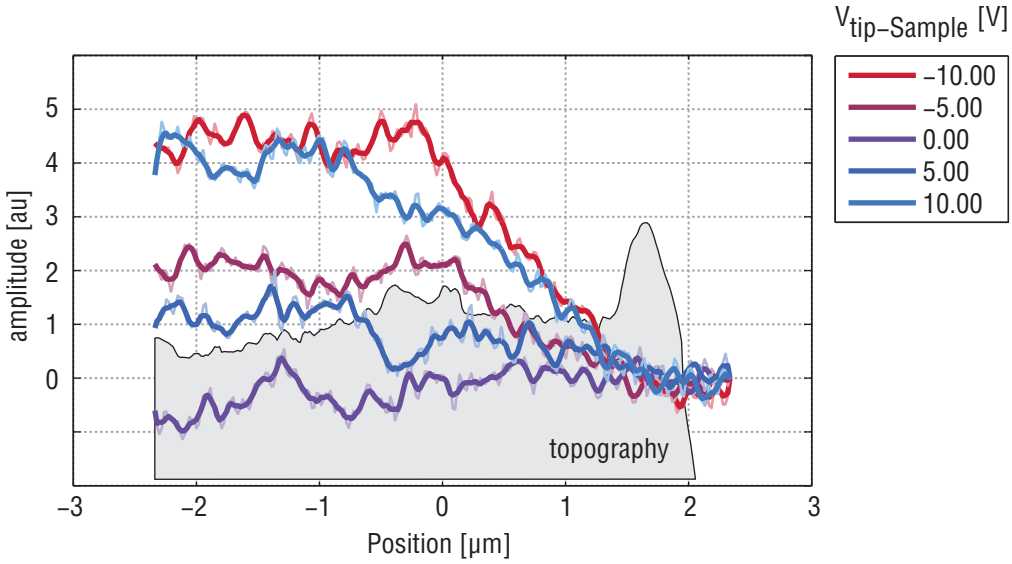

Figure 5.17: Passing the tuning fork over the edge with various dc voltages applied to the tip while exciting it through the 2DEG at 4K.

Another configuration possible for this measurement scheme involves applying the ac excitation signal to the entire sample. In this configuration, the edge electrode and the 2DEG will be at the same potential. Figure 5.18 shows the difference between the potential measured by the tuning fork with (blue) and without (red) participation from the edge electrode. From this measurement we can see clearly that the internal structure of the sample is influencing the remote potential measurements. The larger amplitude of oscillation over the edge electrode is expected since the doped GaAs of which it is comprised extends to the surface.

Examining the traces from figure 5.17 we can see a steady decline in signal as the tip approaches the edge. Of immediate interest is the length scale of the decline: it extends for almost 2 µm before the edge, unlike the dc-EFM images shown in figure 5.9, where the edge manifests itself in the measured signal only after the tip has passed. To understand these features, we can turn to electrostatic modeling of the system.

Modeling the Electrostatics of the Edge

A complete 3D simulation of the electrostatics of the tip-sample system is a major undertaking and not required to obtain a realistic model of the current experiment.[163] Furthermore, since the exact nanoscale geometry of the tip is unknown, it is unfeasible to replicate it exactly in simulation. We can approach an understanding of the system however, by creating a 2D cross

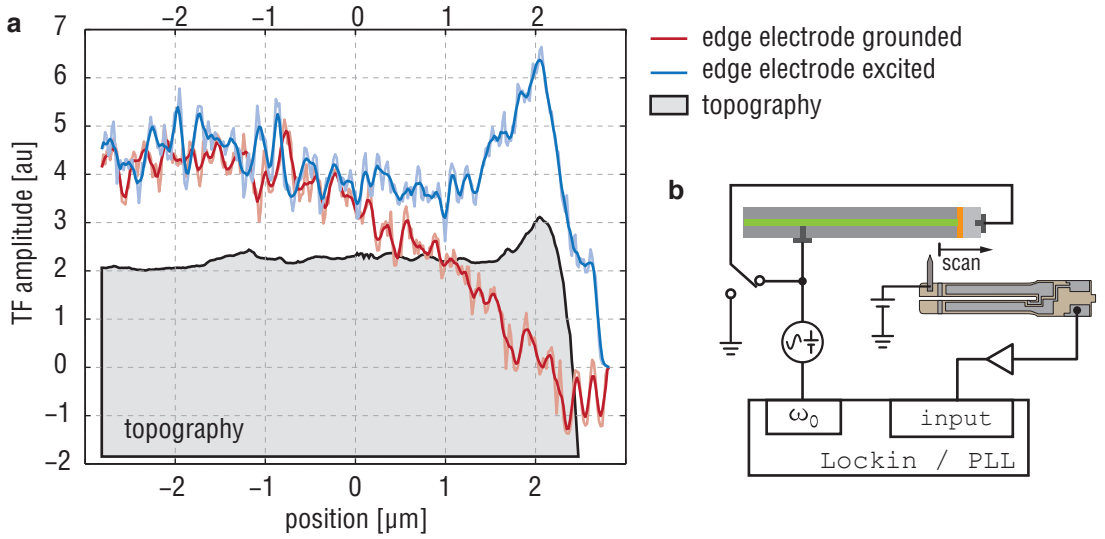

Figure 5.18: **a**: Traces of the tuning fork amplitude as scanned over the edge showing the difference between keeping the edge electrode grounded (red) and exciting the edge as well as the 2DEG (blue). **b**: Scheme of the measurement. The dc bias in both traces was -25 V and they were acquired at a lift height of 100 nm.

sectional model of the CEO sample, which should capture the essential geometry of the system. This is accomplished using standard Finite Element Modeling (FEM). Using the parameters indicated in the sample preparation documentation, essentially a table describing the layer by layer deposition of material in the MBE process, we can create a model with the exact length scales of the sample. Shown in figure 5.19**a** is the meshed model of the sample. The 2DEG, edge barrier, edge electrode and insulating AlGaAs regions are all present. The resolution of the simulation is dictated by the size of the mesh elements, which are made smaller in the region of interest: namely near the barrier.

Applying boundary conditions to the various elements in the model permits numerical solutions of the partial differential equations (PDE) governing the electrostatics of the structures, as determined by the Laplace's equation. For simplicity, the 2DEG and the the edge electrode were considered conductors, and the other elements were given dielectric constants consistent with their material properties. The relative permittivity of $Al_xGa_{1-x}As$ is $\epsilon_r = 13$.[164] A potential of 1 V was applied to the 2DEG region with respect to the edge electrode which was considered as ground. Figure 5.19**b** shows the solution produced by the PDE solver. [7]

Using the results of the calculation, we can obtain an estimation of the potential in the

[7]The meshes were created using GMesh, [165] and the solver used was Elmer.[166]

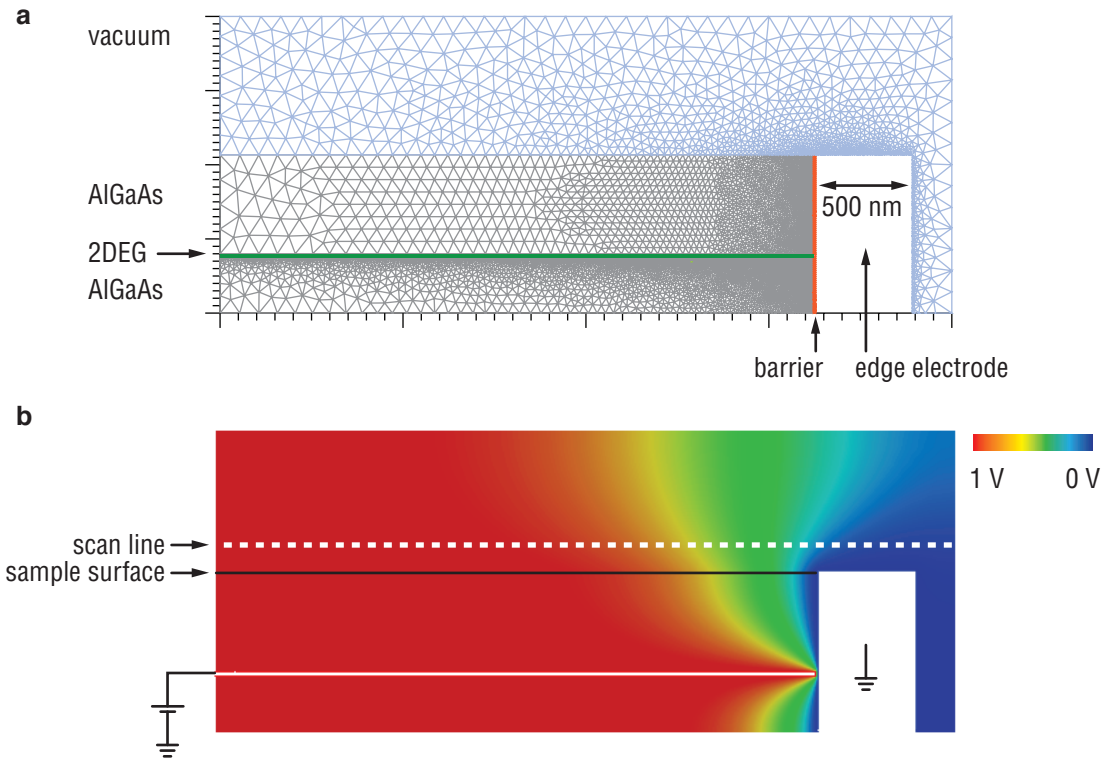

Figure 5.19: **a**: The mesh of the sample geometry. **b**: Resulting potentials when a voltage is applied to the 2DEG and the edge electrode is grounded. A dotted white line indicates the location of the tip during a pass over the edge (∼100 nm above the surface)

vicinity of the edge, as would be measured by the tip. Figure 5.19**b** also contains a line showing the approximate lift height which we take to represent the path the tip takes during a 1D trace 100 nm above the surface. The potentials along this line can be extracted yielding a line profile to be used in comparison with the experimentally measured data.

Our primary concern which prompted the modeling was the 2 μm area before the edge in which the tuning fork response slowly declined. Figure 5.20**a** shows a comparison between the modeled potential profile, and that obtained by the ac-EFM method. For reference, the topography and dc-EFM data are presented as well in **b**. The red curve in 5.20**a** is the extracted line from the solution shown in 5.19**b**. The length span of its attenuation as it approaches the edge is seen to correspond well with the experimentally acquired profile.

The decrease in potential beginning approximately 2 μm before the physical edge can now be understood as a consequence of the internal sample geometry. The implications of this result are important since we can now be confident that our AFM tip is indeed measuring the local potentials given by the electronic properties of the 2DEG. More advanced treatments of

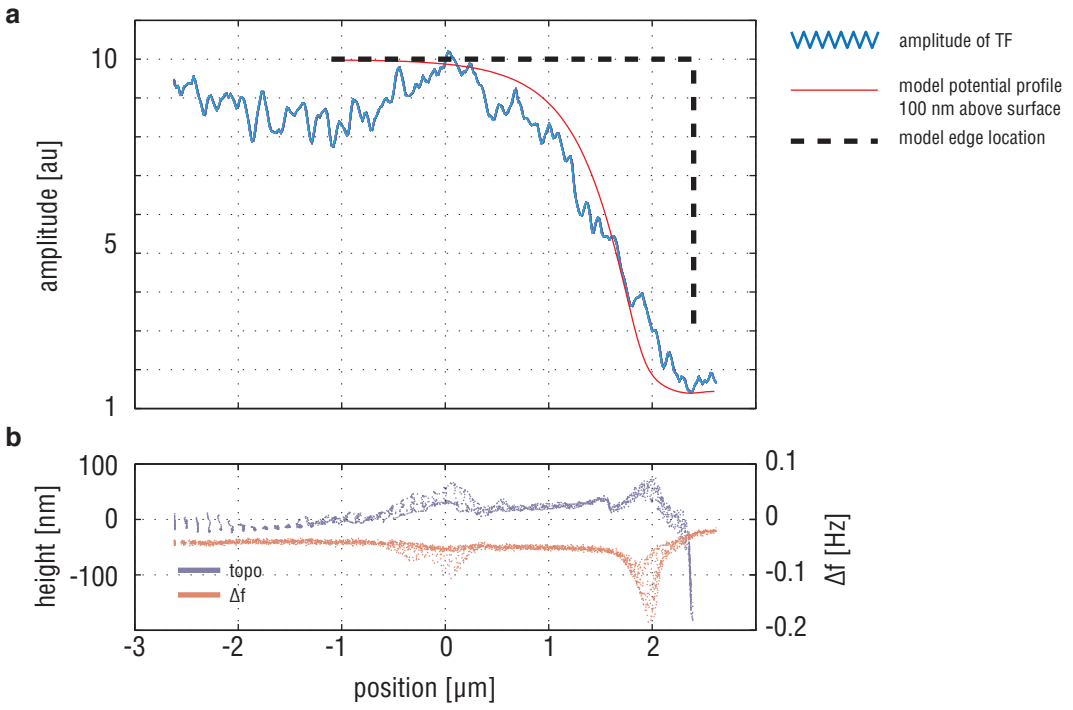

Figure 5.20: **a**: Overlain plots of experimental data and model predictions. **b**: Topographic and dc-EFM data are shown as well to establish the physical location of the edge.

the electrostatic modeling could incorporate the effects of the electron redistribution inside the 2DEG as well as any perturbations caused by the tip itself. For the current application however, the simplified model is sufficient.

Shubnikov-de Haas Oscillations Detected by the Tuning Fork

Now that the tuning fork is effectively coupled to the local potential of the electron gas, applying a magnetic field to the sample should expose the 2D nature of the system. Standard magnetotransport on the sample revealed oscillations in R_{xx} as expected from the Quantum Hall effect, as seen in figure 5.12. While vast amounts of information can be obtained from the transport measurements, they are inherently limited in several ways since the electrical contacts used to obtain them are fixed in position and large compared to the interesting lengths scales of the edge for example. Therefore, obtaining spatially correlated information from them is not feasible. Furthermore, since the resistance becomes precisely quantized at integer or certain fractional filling factors, information hoping to explore these regimes is limited as well

during standard transport measurements.[167, 168] Thus, we have strong motive for exploring alternative measurement techniques which can locally address the microscopic properties of edge states, and quantum Hall regimes in general. Since we have now established the ac-EFM method as a probe of local potential, we can apply this technique to an investigation of the electrodynamics of the QHE.

To begin, the tip is positioned just above the surface at a lift height around 10 nm, near the physical edge, but still over the 2DEG. Applying the ac-EFM excitation voltage to one of the contacts on the 2DEG at the resonance frequency of the cantilever, in this case $\sim$ 20 kHz, excites the tuning fork. We then monitor the tuning fork while ramping the magnetic field. The scheme for this measurement is shown in figure 5.21, along with a circuit model of the system.

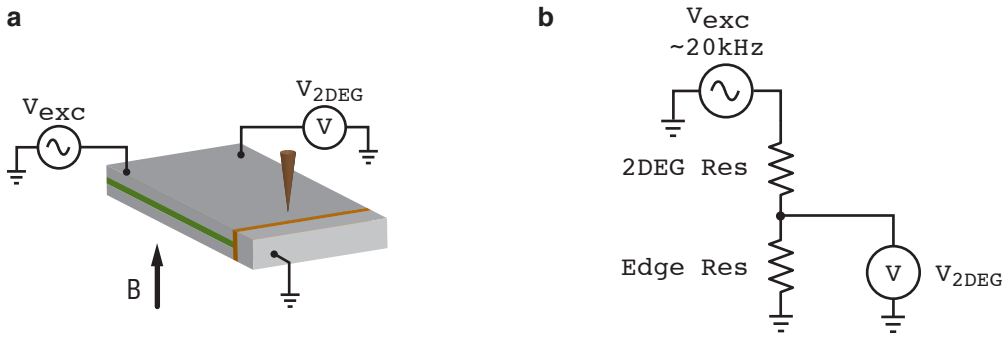

Figure 5.21: **a**: A simple scheme for the measurement of the local 2DEG potential in a magnetic field. **b**: Circuit model based on the sample.

Figure 5.22 shows a plot of the tuning fork amplitude as a function of the magnetic field. Also plotted is the potential recorded from another indium contact to the 2DEG (dotted line). While the tuning fork data is considerably noisy, if we superimpose a smoothed line over top, as a guide to the eye, we can observe a general correlation between it and the potential measured directly from the 2DEG. At low field ($.5 < T < 1$), small Shubnikov-de Haas (SdH) oscillations are seen. The sensitivity of the tuning fork was calibrated for this measurement, thus we can associate a physical amplitude with its output signal. Noticing the oscillation amplitude to be in the sub-Å regime is a testament to the efficacy of the tuning fork detection scheme outlined earlier.

A closer look at the low field, $\sim$ 1 T region shows the effects of the smoothing on the TF amplitude signal. In figure 5.23, a range of smoothing factors are applied to the data and overlain with the original, noisy trace. We can see the oscillations above 0.6 T do correspond with the measured potentials. Below this value, the oscillations are too small to be resolved by the current configuration.

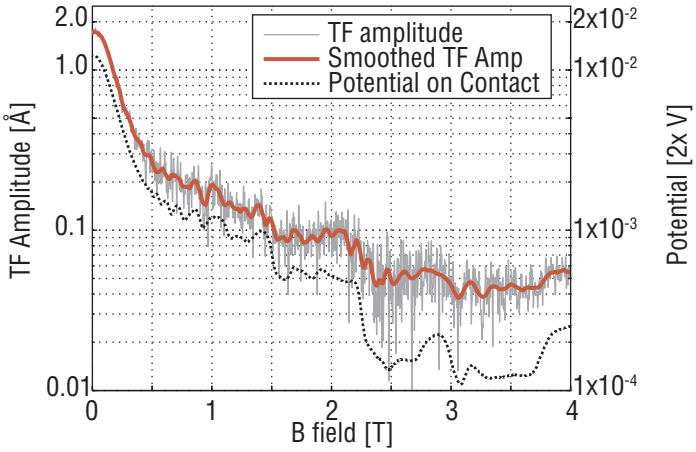

Figure 5.22: Shubnikov-de Haas oscillations measured in the amplitude of the tuning fork. The red line shows the response of the tuning fork while being excited by the potentials of the electron gas. It correlates well with the potential measured on another contact point. The data was acquired at 400 mK. A zoomed section is shown in figure 5.23.

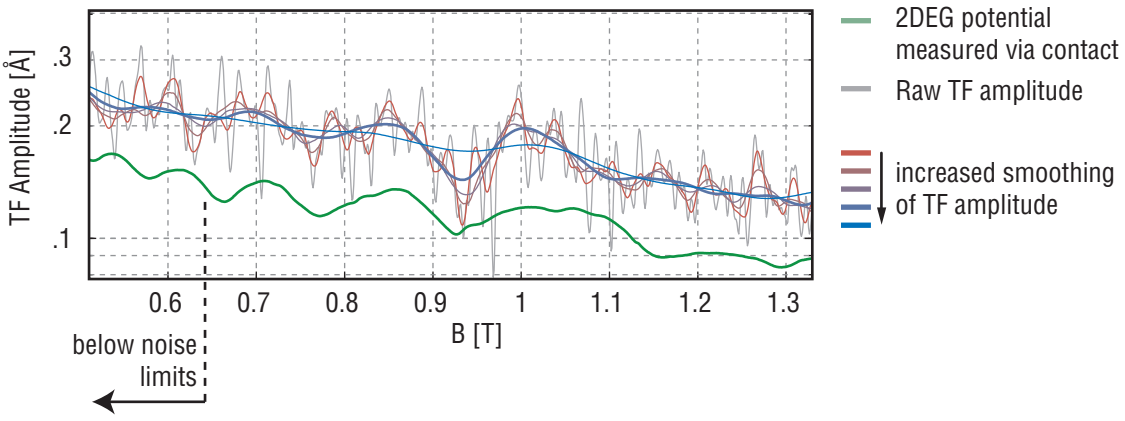

Figure 5.23: The effect of line smoothing on the tuning fork amplitude trace.

We can further understand this result by looking at the circuit model presented in figure 5.21. We note there are two characteristic resistances involved in the circuit, the resistance of the 2DEG, R_{2DEG} and the resistance of the edge barrier, R_{edge}, both of which have magnetic field dependent values. Using the standard voltage divider analysis:

$$V_{2DEG} = \frac{R_{edge}}{R_{edge} + R_{2DEG}} V_{exc}\,, \tag{5.16}$$

in conjunction with traces taken from the transport measurements alone, we can offer an estimate for the V_{2DEG}. This is shown in figure 5.24, where the tuning fork amplitude from figure 5.22 is plotted against the R_{2DEG} and the potential expected after inserting measured values into equation (5.16).

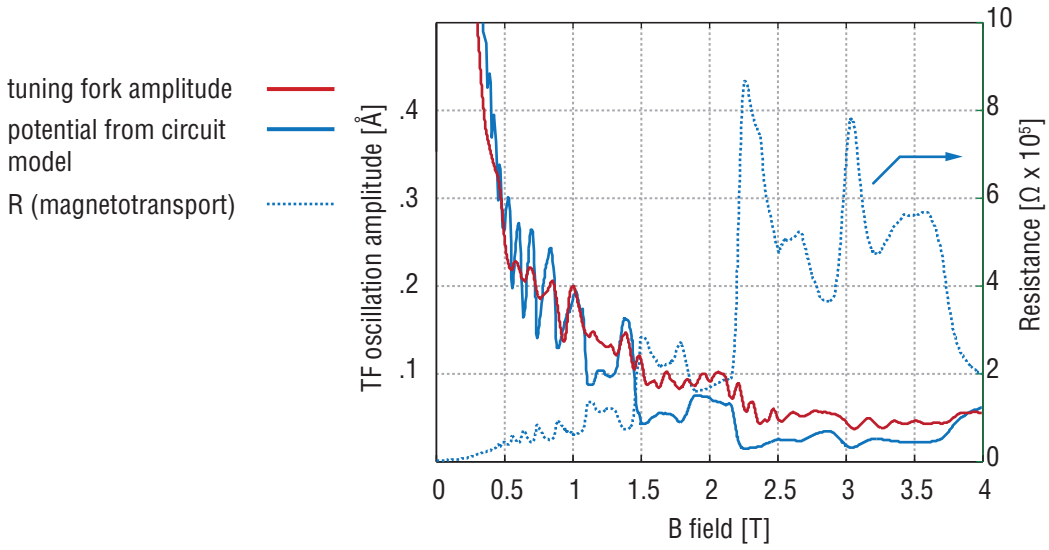

Figure 5.24: Plotting the tuning fork oscillation amplitude together with the prediction from the voltage divider model, as presented in 5.21 and equation (5.16), helps confirm the analysis.

When exciting the tuning fork through the 2DEG, it's clear that the higher V_{exc} we apply, the larger the response of the tuning fork. However, when measuring features such as the SdH oscillations, smaller signals are needed. If the energy associated with the ac input signal is too large (essentially if it exceeds the energy spacing of the landau levels: $\hbar\omega_c = 2.6$ meV at 1 T) it will obscure the features of the transport measurement. Excitation signals in the order of 10 mV are generally the upper limit that we can apply and still resolve the interesting features of the 2D physics of the sample.

5.5 Discussion

Now that it has been shown that we can a) measure the local potentials from the 2DEG, and b) couple the dynamics of the tuning fork to transport phenomena, the microscope should be able to offer insights regarding the spatial distribution of charges in the Quantum Hall regime. Preliminary investigations relying on the ac-EFM technique on the CEO sample were therefore attempted. Shown in figure 5.25**b** are frequency spectra taken in scans over the edge in several magnetic fields (The correlated topography is shown in 5.25**a**).

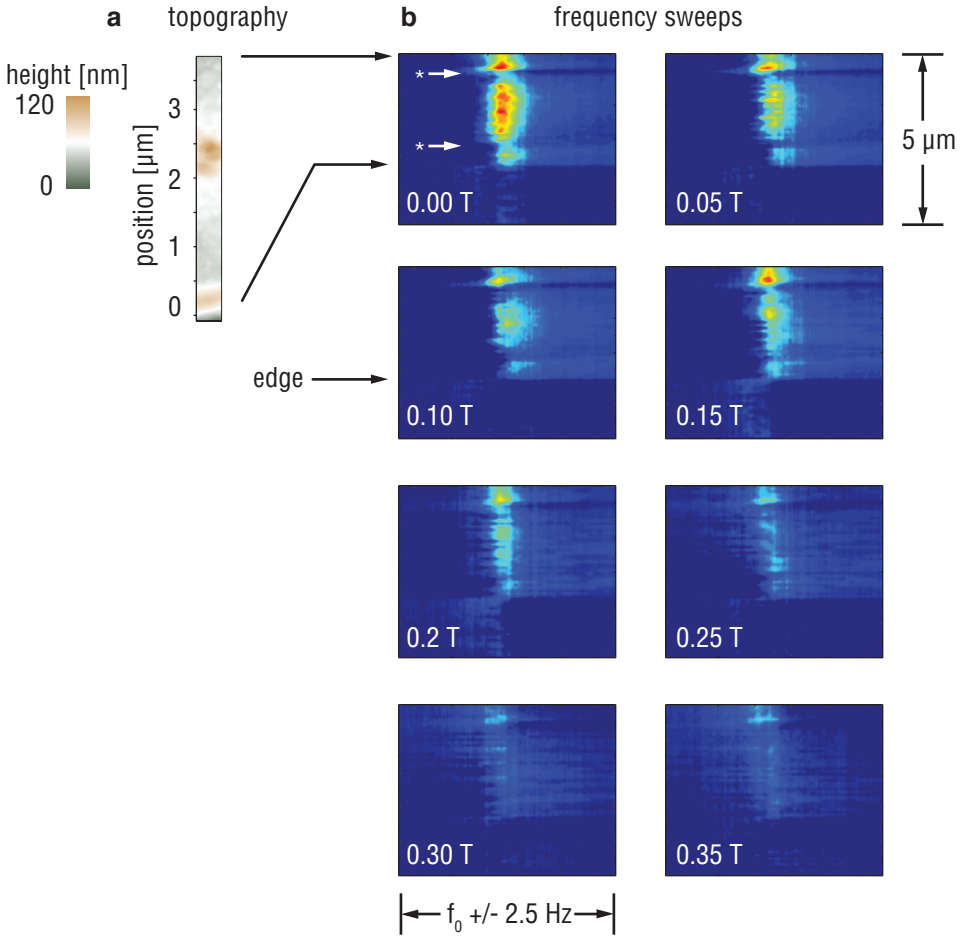

Figure 5.25: **a**: Topographic scan of the area underneath the scans shown in **b**: Sweeps of the excitation frequency of V_{exc} around the resonant frequency of the tuning fork. Red contrast indicates a large response while the dark blue indicates the lower noise floor of the tuning fork. (100 nm lift height and -10 V tip-sample bias)

The essential trend observed in the tuning fork response over the edge as the magnetic field

is applied is a reduction in signal strength, as seen in the lowering of the peak amplitude as the field increases. The features that appear in the frequency response curves (marked with an asterisk⋆ in the 0 T graph) are likely caused by local inhomogeneities in surface charges or other hard to quantify topographic disturbances. Higher fields were attempted as well, yet the only observed effect was again a reduction in the signal, as shown in the two traces in figure 5.26**a**.

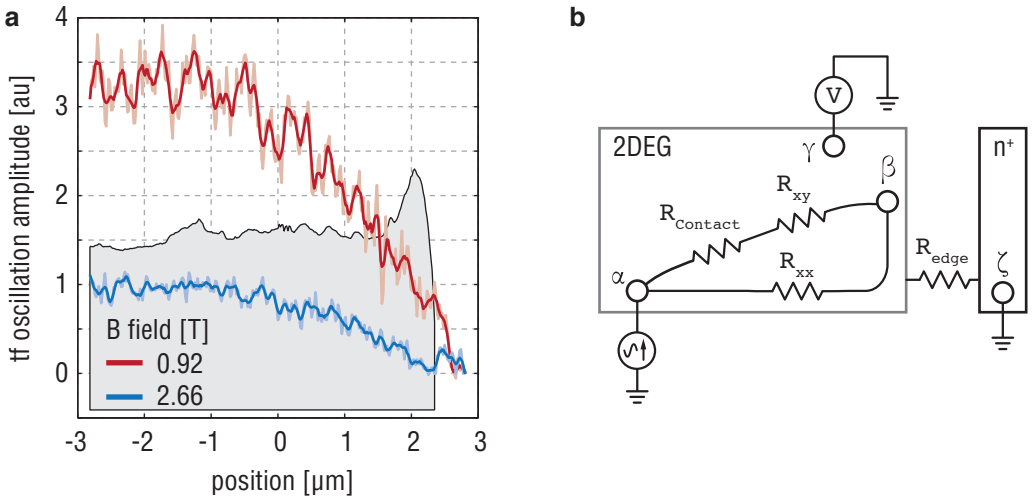

Figure 5.26: **a**: The tuning fork amplitude in higher fields. (100 nm lift and -25 V tip-sample bias) **b**: Geometrical schematic of the 2DEG and contact arrangement showing the combination of resistances which contribute to a measurement.

The strong reduction in signal is attributable to the increased resistance of the 2DEG, R_{2DEG}, when the field is applied, as seen in the resistance plot from figure 5.24. The schematic shown in figure 5.26**b**, a top view of the 2DEG, edge and contact arrangement, helps illustrate. The point labeled α is the 2DEG contact to which the excitation signal is applied. Point β is the approximate location of the force sensing tip. Point γ is the location of another diffused contact which was used to acquire the two-terminal magnetotransport trace. Due to the geometrical arrangement of the contacts and the probe tip, the apparent R_{2DEG} will in fact be a complicated network of several resistances. It must include the contact resistance of the diffused contact, $R_{contact}$, contributions from the Hall resistance, R_{xy}, of the sample as well as contributions from the edge channels. Combining these resistances into one measurement leads to the magnetotransport curve in 5.24, wherein we note a lack of proper zero resistance states. Since we cannot separate the resistances into the orthogonal components, R_{xy} and R_{xx}, in a two probe measurement, we are constrained by the geometry to measure a combination. Our local potential probe is similarly affected. As R_{xy} increases, the potential we are relying on to actuate the cantilever drops well before it reaches the position of the probe tip.

Thus, with this analysis, we can see that the current contact configuration of the CEO sample is not ideal for such measurements. If, for example, two contacts were available on the edge, as is the case in some versions of similar samples, then our instrument would be in a better position to measure isolated R_{xx} transport states since the edge currents could be addressed without resistive contributions from the Hall resistance. Additionally, if the spatial extent of the edge and 2DEG were significantly reduced, scanning gate experiments could be realized in which local density modulations created by the tip were used to affect transport characteristics. These concerns however, belong to the domain of sample preparation rather than instrumentation development.

5.6 Conclusions

To summarize the results of this chapter, we demonstrated the successful application of ac-EFM using a quartz tuning fork at low temperature and with applied magnetic fields. Showing the use of ac-EFM techniques using a tuning fork based microscope inspires more intriguing experiments as many low temperature microscopes have incorporated the tuning fork as a force sensor. Coupling the transport properties of low-dimensional systems to the dynamics of the oscillator should prove useful in future work. While we were unable to ascertain much information about the quantum Hall edge and the distribution of currents therein, it is clear that given a more suitable sample, perhaps a custom made, AFM friendly electron system, such a measurement should be achievable. Additionally, the depth of the 2DEG is another remarkable attribute of this experiment. As mentioned in the introduction, our electron gas is covered by more than half a micron of insulating material. This capping layer helps protect the sensitive transport states of the system. While resolution for spatial mapping of the buried structure will suffer due to the distance, it nonetheless is a valuable alternative method for characterizing the charge transport in such systems.

CHAPTER 6

CONCLUSIONS AND OUTLOOK

6.1 Conclusions

To conclude, we will summarize the major advances put forward during this work, mention some points for further development and propose some potential systems for investigation in the future.

As evidence for the importance of this instrument for condensed matter research, we have demonstrated several new capabilities and contributions:

- The continual effort to understand edge states in Quantum Hall systems requires new tools which can probe spatially correlated electronic properties with sub-μm or better resolution, in the limits of very low signal strength at low temperature and in high magnetic fields. We've shown that the tuning fork based force sensor, though often used for atomic resolution imaging of molecules on surfaces, can be coupled to the electronic states in a two-dimensional electron gas. This ability can be employed to further explore the distribution and nature of the transport in these systems, an area of research still very much under investigation.

- It was also shown that even with a 500 nm insulating layer covering the electron gas, the sensitivity of the instrument was high enough to spatially map the electronic potentials of the buried system. The ability to effectively probe the electronic landscape through such a large capping layer offers a means to characterize other systems which are deeply embedded.

The advances in instrumentation include several notable developments:

- We have demonstrated that atomic force microscopy in extremely high magnetic fields is achievable with the proper design considerations. Field strengths of 15 T represent the highest reported magnetic field environment for a force microscope to date and our work suggests this is limited not by the materials of the microscope but rather by the strength of the available superconducting magnet.

- Retrofitting the dilution unit to accept the microscope was an important component. The fridge was not originally designed for such a large scale experiment and thus needed

many modifications, most notably in the addition of more than one hundred meters of cabling, new thermometry, and the entire experimental tail section.

- The vibration isolation schemes we have instituted have all proven very effective. Cryogenic fluid flows are often large noise sources for sensitive mechanical systems in low temperatures systems. By the inclusion of effective isolation stages, in the low temperature apparatus as well as externally in the lab space, we have been able to suppress the unwanted influence of bubbling 1K pots and external vacuum components.
- A very reliable tip-etching protocol has been developed for the ULT-SPM system. Repeatable electrochemical etching of tungsten tips for the qPlus force sensor is an important aspect of the experimental protocol.
- The custom hardware created for the system, including the tuning fork current to voltage converter as well as several rackmount components for the position sensors and piezo drivers, have all proven effective and reliable during operation. Also, the interfacing between a large number of acquisition and control elements required careful consideration and several iterations to obtain optimum performance.

6.2 Future Modifications

Low-Temperature Electronics

As mentioned in section 2.4, a major source of noise in this instrument stems from the physical distance separating the force sensor and the room temperature electronics. Since few options exist for reducing the overall geometry of the system, the more commonly chosen path to reducing this contribution involves the installation of electronics directly at the location of the microscope. Accomplishing this however, requires very specialized devices that function at low temperature. Additionally, many devices will not perform in the presence of magnetic fields, adding a further complication to any plans for installing components near the tuning fork. Work is currently underway to develop low temperature compatible amplification stages and in time, they should prove useful.

Data Acquisition - Controller

Currently, the ULT-SPM requires two separate computer interfaced hardware components for operation: the Nanonis PLL and the GXSM/SignalRanger controller unit. The PLL serves as the feedback controller for the oscillator and its dynamics, while the GXSM/SR controls the basic scanning operations. Unfortunately, they require two separate operating systems (Windows & Linux respectively), which leads to unwanted complications in data acquisition and

storage. For example, the oscillation control parameters are monitored and stored via the LabView environment on the Windows machine, while the other scan data, such as topography, is stored via GXSM on the Linux machine. Some networking protocols have been instituted to allow communication between the two data storage systems, however, at present it is somewhat awkward and could use improvement. A more unified controller/PLL system would be a significant improvement from a user standpoint.

Force Sensor

While the quartz tuning fork, in particular the qPlus sensor, has been shown to be a highly useful force sensor in certain situations, it has certain deficiencies that prevent it from being a perfect solution to the low-T SPM. As mentioned above, the stiffness, while allowing for very small amplitude oscillation amplitudes in some measurement regimes, notably high resolution FM-AFM, hinders measurement in others. Additionally, the damping losses suffered in magnetic fields are possibly inherent to the piezoelectric detection scheme, as we saw in section 4.4. Unless this can be overcome, it presents severe limitations on the usefulness of tuning forks as force sensors in many magnetic field based experiments.

Tunneling Microscopy

To date, tunneling currents between the tip and the sample have not been measured. Yet, the qPlus sensor in its standard configuration (Figure 2.22) should be able to accommodate such measurements since the etched tungsten tip is no different than those used in many STM instruments. Again, we are limited by the availability of electronics situated near the tip, however, some tunneling measurements should be achievable as is. Having a hybrid scanning force/tunneling microscope would increase the capabilities of the instrument significantly, as tunneling currents can be used for many localized electronic measurements. Little modifications to the existing hardware are needed to operate in the STM mode; it does require non-insulating samples though.

6.3 Other Potential Systems

While certainly the largest and most obvious components in the ULT-SPM are the microscope and low temperature systems, they are only useful when there is a sample to study. The instrument is without a doubt a fantastic piece of hardware, destined for many exciting application in condensed matter physics, yet its use is still limited by the ability to produce interesting, appropriate, and functional samples to investigate. It has become clear during the course of the development of this tool that significant effort needs to be invested in creating such samples.

As this project is a marriage of two somewhat disparate fields, probe microscopy and low-T physics, we sometimes struggle to find a suitable overlap. For example, as seen in the quantum Hall discussion, variables describing the physical geometries of the samples used make no appearance in the governing equations. Thus, amazing measurements have been performed using samples that visually appear as messy as some primary school arts and craft projects. Whereas for serious SPM investigations, many experiments require samples that have never even been exposed to atmosphere. Straddling the line between these two extremes is risky since we are likely be relegated to samples uninteresting in either sphere.

Thus by way of conclusion, we will select some example samples that could provide interesting systems for study in the ULT-SPM.

Graphene

The most natural union between low-T physics and probe microscopy would likely be a graphene device. As it displays many of the exciting physics known to 2DEG structures it offers plenty of excitement in the low-T, high-B context. Additionally, it is well suited for probe microscopy investigations since, as we noted earlier, every atom in the structure is a surface atom.

We carried out preliminary examinations of a graphene device to demonstrate the possibility of attempting graphene based experiments in the future. The general structure of a graphene device involves a monolayer resting, or even suspended, above a SiO_2 insulating layer, which is supported by a larger Si substrate (shown graphically in figure 6.1**a**). To make electrical contact to a graphene sheet, so that transport measurement can be performed, the standard practice is to use electron beam lithographic techniques to create metallic contacts in the desired location and geometry. These metallic pads are usually about 100 nm high and can be defined with $\sim 1\,\mu$m spatial resolution.

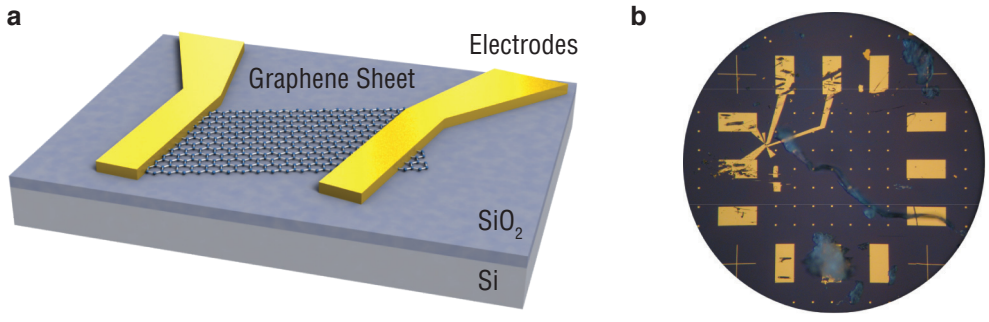

Figure 6.1: **a**: Cartoon of a graphene device layout. Electrodes are defined to create contact with the graphene sheet. **b**: An optical photo of the Si substrate showing the macroscopic view of the sample.

By careful and tedious correlation between optical images, as shown in figure 6.2**a** and AFM topography scans, we can eventually locate the area of interest in a graphene sample.[1] Figure 6.2**c** shows AFM topography of a graphene device, after being mounted in the ULT-SPM sample holder. Comparing with the SEM image of the same area, in **b**, we can see some additional debris has been accumulated on the sample. We can expect improvement in the preparation of the devices as interest continues to grow.

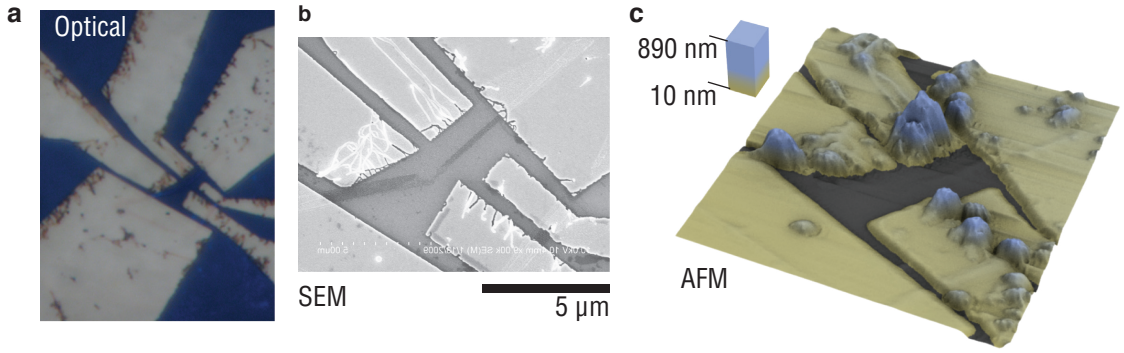

Figure 6.2: **a**: Optical image of the active area. **b**: SEM. **c**: AFM topography taken at room temperature as a proof of principle, showing that we could indeed locate a device and scan the area of interest.

Since similar two dimensional phenomena have been already reported in graphene samples, we can imagine doing experiments similar to those discussed in chapter 5, except with the 2DEG only nanometers away from the tip.[169, 26, 170, 171] This could allow for much higher resolution imaging of the QH transport phenomena and edge states in graphene. Additionally, scanning gate experiments could also yield exciting results again due to the proximity of the tip and sample.

Quantum Dots

Recent work with a low temperature SPM and self-assembled quantum dots has shown interesting results.[34] Measuring the energy loss of the cantilever when a coupled electron tunnels into the dot has enabled quantification of the energy levels of the zero dimensional quantum structure. We have attempted similar experiments in the ULT-SPM, but were unable to replicate the observed effects. This is most likely due to the stiffness of the tuning fork oscillator, which has a spring constant several orders of magnitude higher than the cantilevers used in the original experiment. The larger spring constant, while beneficial for some applications, results

[1] Again, from a sample preparation viewpoint, this difficulty can be somewhat alleviated by including lithographically defined grid markers on the sample, thus providing an *in situ* roadmap.

in a decrease in the response of the oscillator due to external interactions, in this case, the energy transferred to the tunneling electrons. It has been shown that the dissipation, γ, scales as:[34]

$$\gamma \propto \frac{\omega_0^2 A^2}{k k_B T} . \tag{6.1}$$

Thus we have two factors going against us, the spring constant, k, and resonant frequency, ω_0, of the cantilever are larger and smaller respectively. Given that our cantilever resonant frequency is ∼20 kHz, compared to 200 kHz, and the spring constant is ∼ 2000 N/m compared to 40 N/m, any damping signal detected by the tuning fork oscillator would be a factor of 2×10^{-5} smaller compared to the Si cantilever used in the original experiments, assuming all other experimental variables to be similar. To increase our sensitivity to damping terms, using smaller, softer tuning forks and/or operating at higher frequencies using higher harmonics of the oscillator might bring us within the parameter space necessary to observe single electron tunneling events in quantum dots.[130, 172] If this can be accomplished, application of the magnetic field to these systems could prove very exciting.

6.4 Final Words

With these prescriptions, we will conclude, hoping that those who seek guidance in related works find assistance herein. The ULT-SPM project has been a significant undertaking in experimental science and has produced a world class instrument with much potential.

APPENDIX A

PIEZOELECTRICITY

Several major components of the SPM rely on the physics of piezoelectricity. Hence, a minor detour into the phenomenon shall prove helpful.

History

Pyroelectricity, the generation of electric potentials on material due to heating or cooling, was a well known phenomenon at the end of the 19th century. During their investigations of pyroelectricity, the Curie brothers Jacques and Pierre, later to be recognized for other contributions to physics and chemistry, noted the formation of electric potentials on certain crystals in response to pressure applied to the crystal facets. "We have found a new way of developing polar electricity in these crystals [semi-symmetrical crystals with oblique faces] that consists of subjecting them to variations in pressure following their hemihedral axis." This was reported in the Bulletin de la Société minéralogique in 1880.[173] In the years following, the new field of piezoelectricity attracted the attentions of many prominent physicists (including: Pierre Duhem, Wilhelm Röntgen, and William Thomson). These initial forays into a physical description of piezoelectricity offer an always welcome example of the dependencies between of theory and experiment in science. Shortly after the Curies presented their results, Gabriel Lippmann, a former student of Helmholtz and Kirchoff, suggested the existence of the converse piezoelectric effect, that is, the creation of strain from applied potentials, based on newly developed conservation of charge principles. Having learned of this prediction, the Curie brothers spared no time in experimentally verifying it, initially employing somewhat incestuously the direct piezoelectric effect, then later by visually measuring a change in length of a quartz crystal. The length deviations were less than 1 micron and their measurements after several refinements matched the theory to within 10%, giving credit to their experimental methods. (For more on the history of piezoelectricity, see [174, 175]

Descriptive Framework

A complete description of the mathematical framework used to describe piezoelectric phenomena will not be necessary here. However, we can briefly examine a few points that will aid in related discussions.

The most relevant parameter used to describe the piezoelectric properties of various materials is the piezoelectric constant: d_{ij}, simply defined as the ratio of the strain in the j-axis to

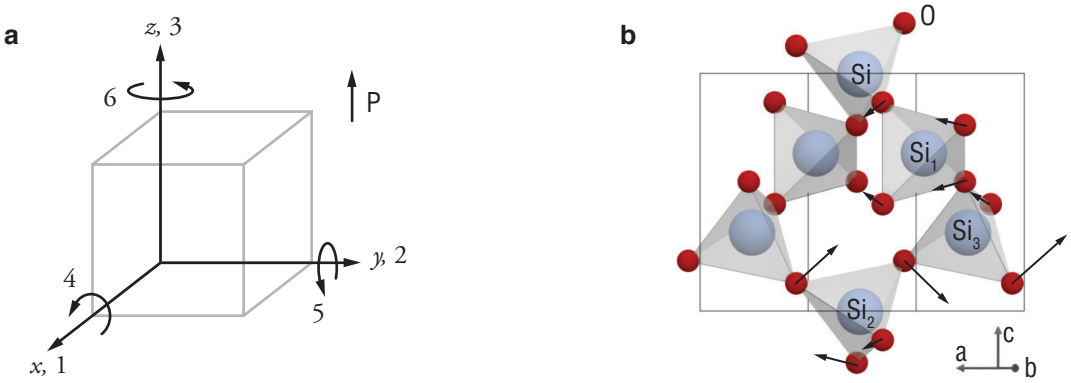

Figure A.1: **a**: The axes used in describing piezoelectric effects and **b**: the unit cell of α-quartz showing the SiO_4 tetrahedra.

the electric field applied along the i-axis, if all external stresses are zero:[118]

$$d_{ij} = \frac{S_i}{E_j}, \tag{A.1}$$

where S_i and E_j are the strain the electric field components. (Here, indices 1,2,3 refer to the x, y, and z axis, while indices 4, 5, 6 indicate torque about those same axes, as shown in figure A.1) The d_{ij} constant is often quoted by manufacturers to describe the performance of different piezoelectric crystals. For example, crystals with a significant d_{15} constant are employed as shear actuators for the coarse positioning motors. Other constants are also used to describe piezoelectric phenomena, however, they were not considered in the design of the microscope.

Microscopic Origins

PZT

The piezoelectric ceramic known as lead zirconate titanate (PZT) is in the SPM coarse motors and the scanning tube. These man-made ceramics require polarization to become piezoelectric. Above the Curie temperature, the elementary cell is cubic, and no piezoelectricity is possible. Below this temperature however, the cell forms a tetragonal structure which does allow for the piezoelectric effect (PZE), after proper polarization steps. To accomplish this, a strong electric field is applied in the desired polarization axis. This field aligns the dipoles of the Weiss domains within the crystal, leading to a non-zero macroscopic electric dipole. The crystal is now piezoelectric and will exhibit the properties expected.[176] These changes are shown in figure A.2.

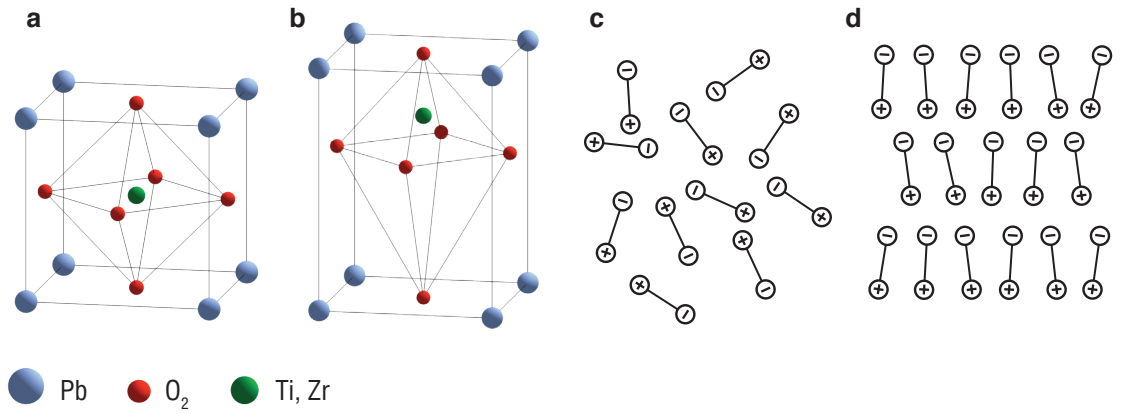

Figure A.2: The crystal structure above **a**, and below, **b** the Curie temperatures. **c**,**d** show the domain orientation before and after polarization.

Quartz

α-Quartz is the most common mineral on earth. The tuning fork force sensor used in this SPM is made of quartz, thus nearly every image shown in this document owes its existence in some way to the piezoelectric properties of quartz.

Many efforts have been made to understand the microscopic origins of the PZE in quartz. The Curie's original explanations hypothesized that intermolecular distances between polarized molecules in the quartz were altered due to compression or expansion. Soon, it became clear that this was an insufficient explanation, since polarizing effects were also observed in torsion experiments. Woldemar Voigt launched the overall successful phenomenological theory of piezoelectricity in 1890. Although failing to offer a foundational theory based on a molecular model, (this was a time even accomplished physicists had doubts about the existence of atoms [177]), Voigt's phenomenological model offered a rigorous mathematical formulation that provided an analytical scaffolding for future efforts. 1926 brought with it a major advance in an atomic description of the quartz's piezo and pyro electric properties when Bragg and Gibbs predicted, with a factor of four, the piezoelectric coefficients, based on crystallographic data obtained through x-ray diffraction. [178, 179]

Recent work in the microscopic origin of piezoelectric has been able to combine first-principle derivations based on the crystal structure of the materials. Density-functional theory based calculations suggest an microscopic origin for the PZE resulting from strain induced translocations and rotations of SiO_4 tetrahedra in the unit cell of α-quartz, as shown in figure A.1. [180]

APPENDIX B

QUALITY FACTOR

The notion of an oscillator's *quality factor* is useful for understanding many elements of this work, in particular, the choice of the quartz tuning fork as force sensor. Applicable to any oscillating system, be it a mechanical beam or resonant circuit, the quality factor describes the damping:

$$Q = 2\pi \frac{\text{TotalEnergy}}{\text{EnergyLostperCycle}} \tag{B.1}$$

Considering a driven resonator response, the quality factor can also be found by examination of the Lorentzian line shape characteristic of an oscillator.[181]

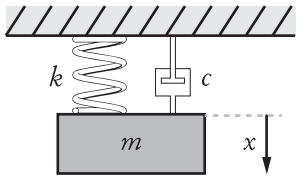

Figure B.1: A spring-mass-damper system

Starting with the damped, driven oscillator, as described in figure B.1, the differential equation of motion can be written as:

$$m\ddot{x} + c\dot{x} + kx = F_0 e^{i\omega t}\,, \tag{B.2}$$

where m is the mass of the object, k the spring constant, c the damping coefficient, and F_0 the applied force. We can try the solution $x(t) = Ae^{i(\omega t - \phi)}$, leading to the real and imaginary solutions:

$$A(k - m\omega^2) \quad = F_0 \cos\phi \tag{B.3}$$

$$c\ \omega A \quad = F_0 \sin\phi\,. \tag{B.4}$$

Or, since $\sin^2\phi + \cos^2\phi = 1$, we have for the oscillator's amplitude as a function of drive frequency ω:

$$A(\omega) = \frac{F_0}{\left[\left(k - m\omega^2\right)^2 + c^2\omega^2\right]^{1/2}}. \tag{B.5}$$

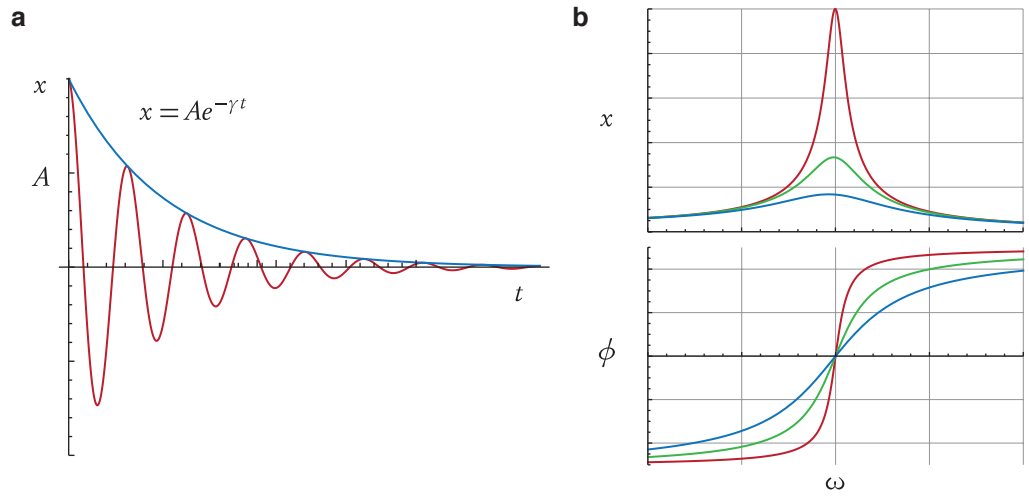

Figure B.2: **a**: Response of an oscillator to damping over time. **b**: Amplitude and phase plots showing a decrease in amplitude as damping is increased.

And, with $\omega_0^2 = k/m$ and $\gamma = c/2m$, we arrive at the common Lorentzian line shape describing the amplitude of oscillation:

$$A(\omega) = \frac{F_0/m}{\left[\left(\omega_0^2 - \omega^2\right)^2 + 4\gamma^2\omega^2\right]^{1/2}}, \tag{B.6}$$

and

$$\tan\phi = \frac{2\gamma\omega}{\omega_0^2 - \omega^2}, \tag{B.7}$$

to describe the phase response of the oscillator. The energy of an oscillator is given by:

$$E = \frac{1}{2}m\dot{x}^2 + \frac{1}{2}kx^2 \tag{B.8}$$

To find the amount lost per cycle, we can integrate the time derivative of this expression,

$$\Delta E = \int_0^{T_d} \dot{E}\,dt \tag{B.9}$$

over one full period, T_d. Assuming small damping, we arrive at

$$\Delta E = -\gamma m\omega_0^2 A^2 e^{-2\gamma t} T_d \tag{B.10}$$

Using the time constant formulation, $\tau = 1/2\gamma$, and the average energy, $\langle E\rangle = \langle V\rangle + \langle K\rangle$, we can obtain:

$$\frac{\Delta E}{E} = \frac{T_d}{\tau}. \tag{B.11}$$

Thus the quality factor, Q, can be expressed as:

$$Q = \frac{2\pi}{\left(T_d/\tau\right)} = \omega_d \tau = \frac{\omega_d}{2\gamma} \approx \frac{\omega_0}{2\gamma}, \tag{B.12}$$

where the last approximation is valid in the case of weak damping, Since γ is a measure of the width of the resonance curve, specifically, the distance in frequency away from the resonance that will have $1/2$ the energy of the resonance point, we can also write:

$$\Delta\omega = 2\gamma \simeq \frac{\omega_0}{Q} \rightarrow \frac{\Delta\omega}{\omega_0} = \frac{\Delta f}{f_0} = \frac{1}{Q} \tag{B.13}$$

APPENDIX C

RECIPES

C.1 Construction of a qPlus Sensor

Isolate the tuning fork from its packaging: this can be accomplished using a pair of small tweezers. After breaking the epoxy seal at the base of the cylinder, the tuning fork unit is easily removable. The wire electrodes soldered to the tuning fork must also be removed as they are of unknown composition and tend to be somewhat magnetic.

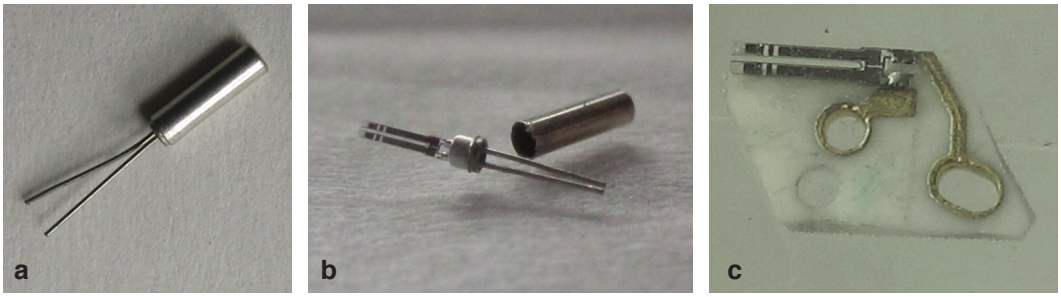

Figure C.1: photographs of the tuning fork in various stages: **a**: in its original, vacuum sealed packaging, **b**: removed from the can yet still attached to leads, **c**: glued to alumina substrate

The tuning fork must then be glued to a firm base unit. This base unit is a micro-machined alumina substrate with patterned electrodes in place.[1] Alumina is a good choice for the base unit since it has a low coefficient of thermal expansion [100], is electrically insulating, and quite hard. The patterned electrodes were designed to allow for easy contacting of the tuning fork electrodes. Stycast 1266 epoxy is used to anchor one tine of the TF to the Alumina substrate. After extensive testing with different epoxies, 1266 was found to offer the best adhesion in this circumstance and generally led to higher quality factors for the tuning forks.

After the tuning fork is mounted to the alumina substrate, a tungsten tip must then be glued to the free tine of the tuning fork. To make the electronics simpler during operation of the microscope, the tungsten wire is electrically isolated from the tine of the tuning fork and connected via a ultra-thin Silver wire. Silver epoxy (Epotek 4110) is used for these junctions. Electrical contact to the tip is necessary for a number of reasons:

[1] Thanks to Franz Giessibl for providing us with these substrates

- *tip sample biases*, a key ingredient in many experiments require well-defined contact to the tip. This is made simpler by including a separate wire to the tip.
- *electrochemical etching* can only be accomplished by using the tip as a counter-electrode in the cell.
- *tunneling microscopy* can be performed if the current between the tip/sample can be measured. This measurement is also much simpler if the tip is isolated from the tuning fork.

C.2 Low-Temperature Measurement Schemes

The experiments documented herein, as well as many of the others proposed for the ULT-SPM, require the use of standard low temperature physics measurement techniques. A quick overview of this methodology is included here since several measurement techniques required the construction of specialized instrumentation hardware and devices.

Resistance

Resistance measurements are often a key component to many low-T experiments. For example, standard Quantum Hall traces plot the resistance of the 2DEG as a function of magnetic field. Or, as will be seen in Chapter 5, the tunneling resistance a barrier can be of interest. Thus, sensitive resistance measurement are needed. The standard methods for resistance measurements rely on Ohm's Law:

$$V = IR \tag{C.1}$$

By applying either a known Voltage, V, and measuring the resulting current, I, or visa versa, a value for the resistance, R, can be obtained.

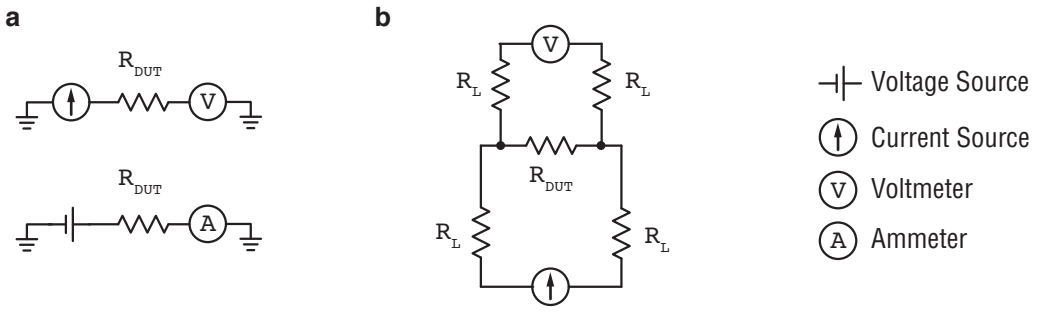

Figure C.2: **a**: Standard two probe measurement schemes. **b**: The four probe scheme.

Two-Probe measurement

The most basic means of accomplishing this is by a standard two-probe measurement in which we provide either a source voltage (current) and measure the resulting current (voltage). This requires only two contacts to the device under test (DUT). A major drawback to this scheme is the inclusion of any contact or lead resistances, R_L, in the measured resistance. In 2DEG measurements, contact resistances can be in the same order of magnitude as the sample resistance, and will thus interfere with an accurate evaluation of R_{DUT}.

Four-Probe measurement

The standard workaround for eliminating contact resistances in measurements is by using a four terminal measurement scheme, as shown in figure C.2. Here, a sourcing current I is forced through the DUT via one pair of leads. Simultaneously, the voltage across the DUT is measured by another set of leads. Since the impedance of the voltmeter can be considered high, only a negligible current will flow through the sensing leads, allowing the voltage measurement to determine only the voltage drop across the DUT.

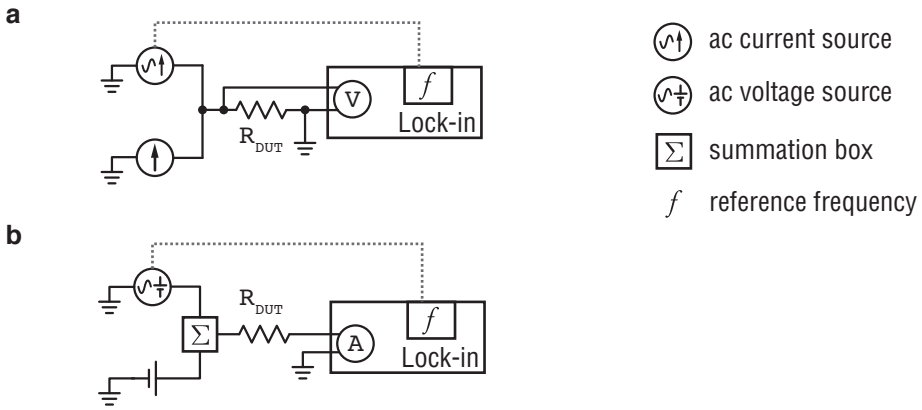

Figure C.3: **a**: Current sourced differential resistance measurement. **b**: Voltage sourced differential conductance measurement requiring a custom built summation box to add the ac and dc voltages.

Derivative measurements

To increase the sensitivity of our resistance measurements, differential measurements are often used. Rather than sourcing currents (voltages) with DC values, currents (voltages) with small ac modulations (usually in the order of 10 Hz) can be applied to the DUT. The resulting ac voltage

(current), is then measured with a lock-in amplifier set to the frequency of the ac source. Since

$$\frac{dV}{dI} = R, \tag{C.2}$$

measuring the change in voltage (current) with respect current (voltage) yields a measure of resistance (conductance). Experimentally, this involves slightly more instrumentation, yet the investment is worth it as the resolution of the measurement will be improved. See figure C.3 for a basic schematic.

C.3 Approaching the Surface

Perhaps the most painstaking part of performing an experiment in the ULT-SPM is the first coarse approach in which the scan tube is raised by the z motors until the tip and sample are within feedback distance. Low temperature piezo motors are notorious for being temperamental. With due patience however, they can usually be coaxed into motion.

The Function Generator (HP 33220A) will be used to create the pulsed wave form needed to drive the piezo motors. It has a higher resolution in frequency and voltage which seems to be needed to find the optimal driving parameters for the motors. The GXSM software will only be used to trigger the FG, rather than generate the needed waveforms.

Make sure OUTPUT on the FG is off.

1. Connect the output of the FG to the input of the HV transformer on the rack.

2. Connect the Motor output of the Signal Ranger to the External Trigger on the back of the FG.

3. Select the Arbitrary waveform labeled SLIP_STICK3 by entering the ARB menu on the FG.

4. In the GXSM Mover Control window, enter the following parameters:
   Amplitude: 2V
   Wave Period: 3 ms
   Max. Steps: 1

5. If the optimal parameters for z motion are known (see Table 2.1 for suggestion values), enter them into the FG.

6. Press the BURST button and select the number of Cycles that will move the Prism Up (30-60 at RoomT)

7. Pressing OUTPUT now will arm the FG. Pressing TRIGGER will execute the bursts -or- pressing the +Z on GXSM mover control will also execute the bursts.

8. To move in the opposite direction: Select UTILITY from the FG front panel, and change from normal to invert in the settings tab.

APPENDIX D

VIBRATION ISOLATION

Analysis of Vibration Isolation Stages

Since nearly all the measurable quantities in an AFM based experiment are in someway related to the distance between the tip and sample d_{t-s}, minimizing unwanted fluctuations of this value is a crucial component of the instrumentation.

The first line of defense against the attacking hoards of vibrations is a very rigid microscope, such that d_{t-s} remains constant in the absence of any intentional modulation.[182] Factors that influence the rigidity include:

- The mechanical rigidity of the SPM body: Early SPMs used an open frame type design. While facilitating access to the scanner assembly, such a frame also allows for a bending mode induced level action between the upper and lower sections. This can be negated by using a closed structure. Figure D.1 highlights this difference.

- Batten down the hatches: In our SPM frame design, a modular approach was needed to allow access to the course motors and position sensors. As shown in section 2.2, there are two detachable sections. Before undergoing an experiment, ensuring that these two sections are firmly secured via the internal threaded rods is a critical step.

- The piezo tube resonances as dictated by its physical properties: Although, we are very much limited in our choice of piezo tube geometry since the low temperatures reduction of the piezoelectric constant requires a long tube in order to achieve practical scan ranges.

We can model the microscope and infrastructure as spring-mass-damper systems in series, as shown in Figure D.1.[183] Preventing vibrations from reaching the scanner assembly is also crucial. The amplitude of these transmitted vibrations depends on the various parameters of the systems and can be determined by examining the transfer functions of the various displacements. We can write the kinetic (T) and potential (U) energies and dissipative function, D for

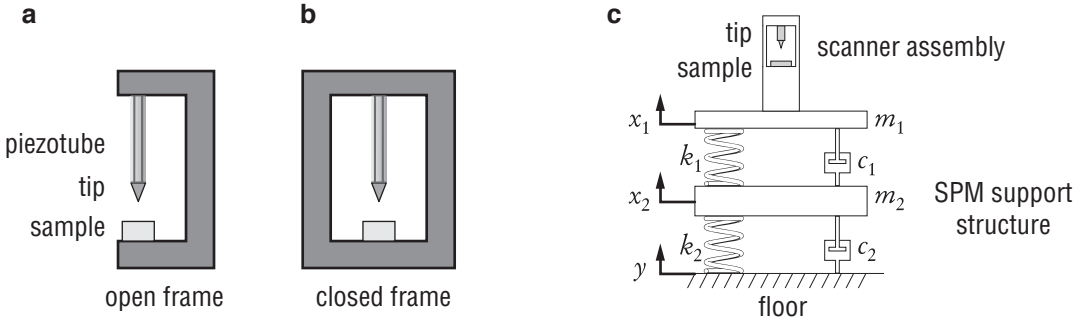

Figure D.1: **a** and **b** show the open vs. closed frame concepts. **c**: A simplified 1-D model of the vibration isolation concept showing the different degrees of freedom in a multi-stage isolation design.

the system of Figure D.1 as:

$$T = \frac{1}{2}\left(m_1\dot{x}_1^2 + m_2\dot{x}_2^2\right) \tag{D.1}$$

$$U = \frac{1}{2}\left(k_1(x_1 - x_2)^2 + k_2(x_2 - y)^2\right) \tag{D.2}$$

$$D = \frac{1}{2}\sum_{i,k} c_{i,k}\dot{x}_i\dot{x}_k = \frac{1}{2}\left(c_1(\dot{x}_1 - \dot{x}_2)^2 + c_2(\dot{x}_2 - \dot{y})^2\right), \tag{D.3}$$

where m_i is the mass, c_i is the dissipation constant, and k_i is the spring constant for the various coordinates. Then, with the Lagrangian for dissipative systems:

$$\sum_{i=1}^{n}\left[\frac{d}{dt}\left(\frac{\partial L}{\partial \dot{x}_i}\right) - \frac{\partial L}{\partial x_i} + \frac{\partial D}{\partial \dot{x}_i} = Q_i\right], \tag{D.4}$$

where:

$$L = T - U \text{ and } Q_i = \text{applied force}, \tag{D.5}$$

we can arrive at a system of differential equations describing the various motions.

$$m_1\ddot{x}_1 + c_1(\dot{x}_1 - \dot{x}_2) + k_1(x_1 - x_2) = 0 \tag{D.6}$$

$$m_2\ddot{x}_2 + c_2(\dot{x}_2 - \dot{y}) + c_1(\dot{x}_2 - \dot{x}_1) + k_2(x_2 - y) + k_1(x_2 - x_1) = 0 \tag{D.7}$$

Assuming the standard oscillatory solutions:

$$y = A\,e^{i\omega t} \tag{D.8a}$$

$$x_1 = H_{x_1 y}\,A\,e^{i\omega t} \tag{D.8b}$$

$$x_2 = H_{x_2 y}\,A\,e^{i\omega t}, \tag{D.8c}$$

will lead to the transfer functions: $H_{x_1 y}(\omega)$ and $H_{x_2 y}(\omega)$ where $H_{ij}(\omega)$ is the frequency response of the coordinate i to an input excitation j. This system can easily be expanded to deal with more degrees of freedom. For example, as shown in Figure 3.7, our microscope support structure has a third spring-mass-damper damper system. By picking some reasonable values for the constants m_i, k_i, and c_i, when can come to a basic understanding of the effect of multiple stages. In the absence of any damping terms, i.e. $c_i = 0$, we can see in Figure D.2 an attenuation of the transfer function at frequencies above the cross-over frequency, which is determined by the highest resonance of the structure. This attenuation come at the cost of adding resonance peaks in the lower frequency regime. However, if damping terms are considered, we can see the trade off to be beneficial.

Generally, it is impractical to try to access the exact coefficients for the various stages before construction. However, some reasonable estimations can be made to guide the design stage.

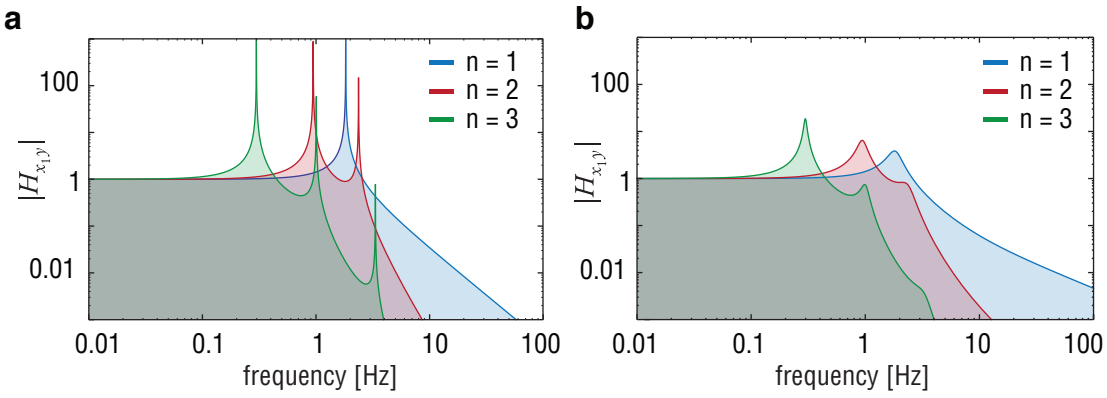

Figure D.2: Comparison of single, double, and triple spring-mass-damper stages where $n =$ the number of stages: a) The undamped transfer function of a three coupled spring-mass-damper systems. The three resonances of the various stages. (Values for the equations of motion: $m_{1,2,3} = 1, 10, 100$; $k_{1,2,3} = 10$; $c_{1,2,3} = 0$.) b) Including damping terms reduced this resonance peaks at the expense of the high frequency attenuation. (Values for the equations of motion: $m_{1,2,3} = 1, 10, 100$; $k_{1,2,3} = 10$; $c_{1,2,3} = 1$.) The plots were calculated using the solutions for $H_{x_1 y}$ in equation D.8 via Mathematica.

APPENDIX E

DETAILED SCHEMATICS

E.1 Fridge Components

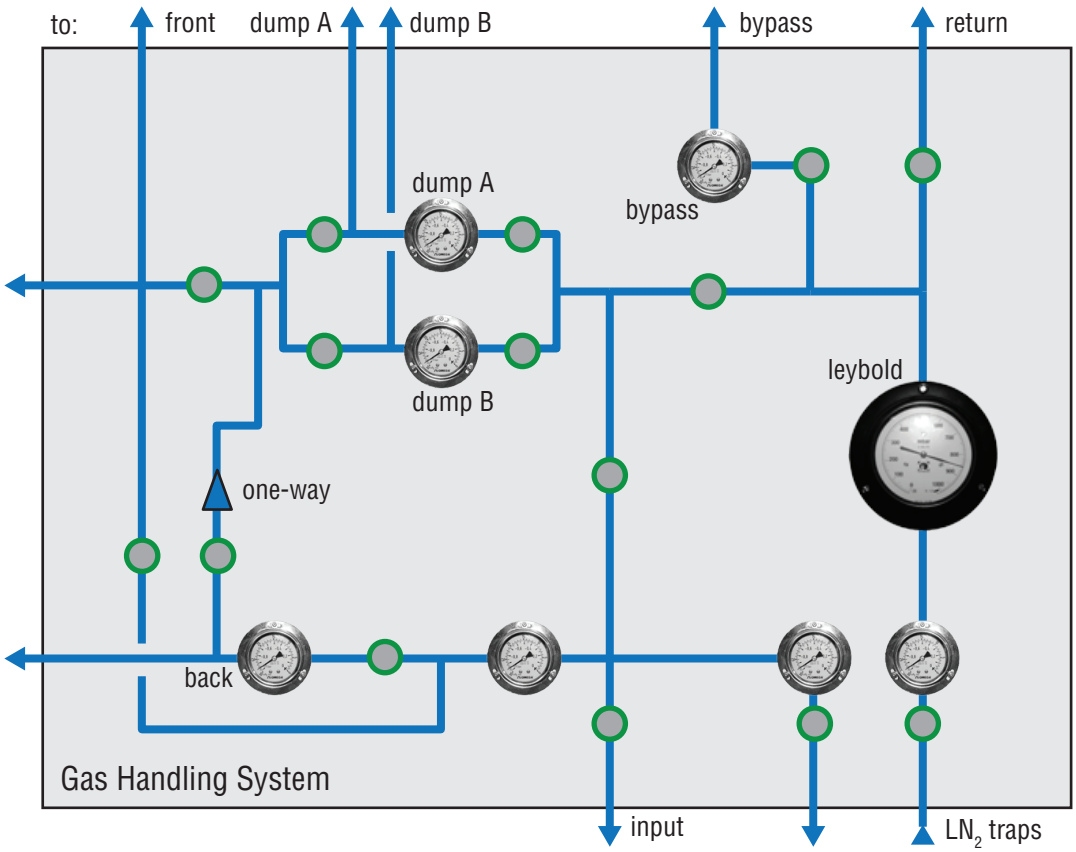

Figure E.1: Detail of the gas handling system showing gauges, piping lines, and valves

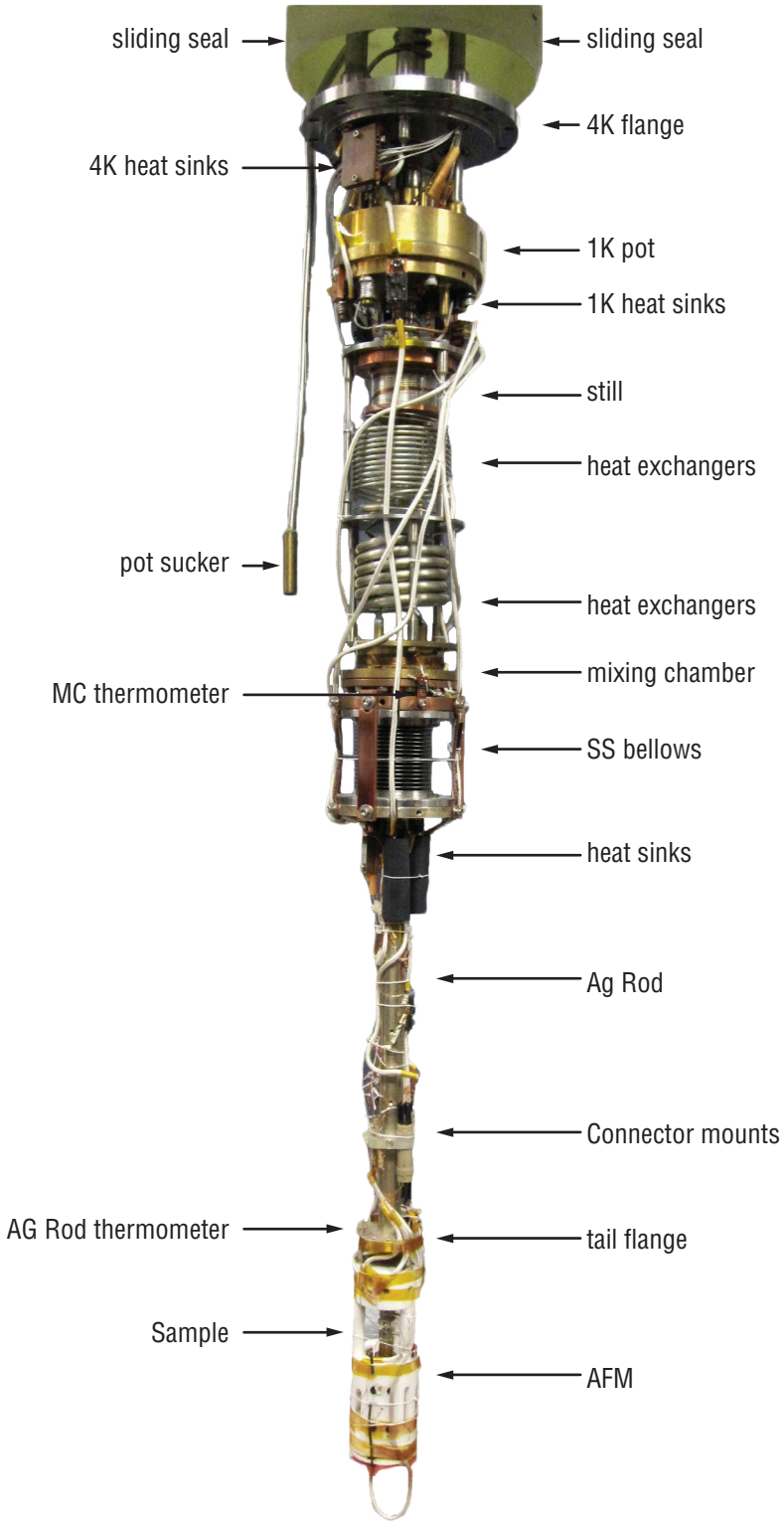

Figure E.2: Photograph of the dilution unit with the AFM in place

E.2 Superconducting Magnet (Oxford)

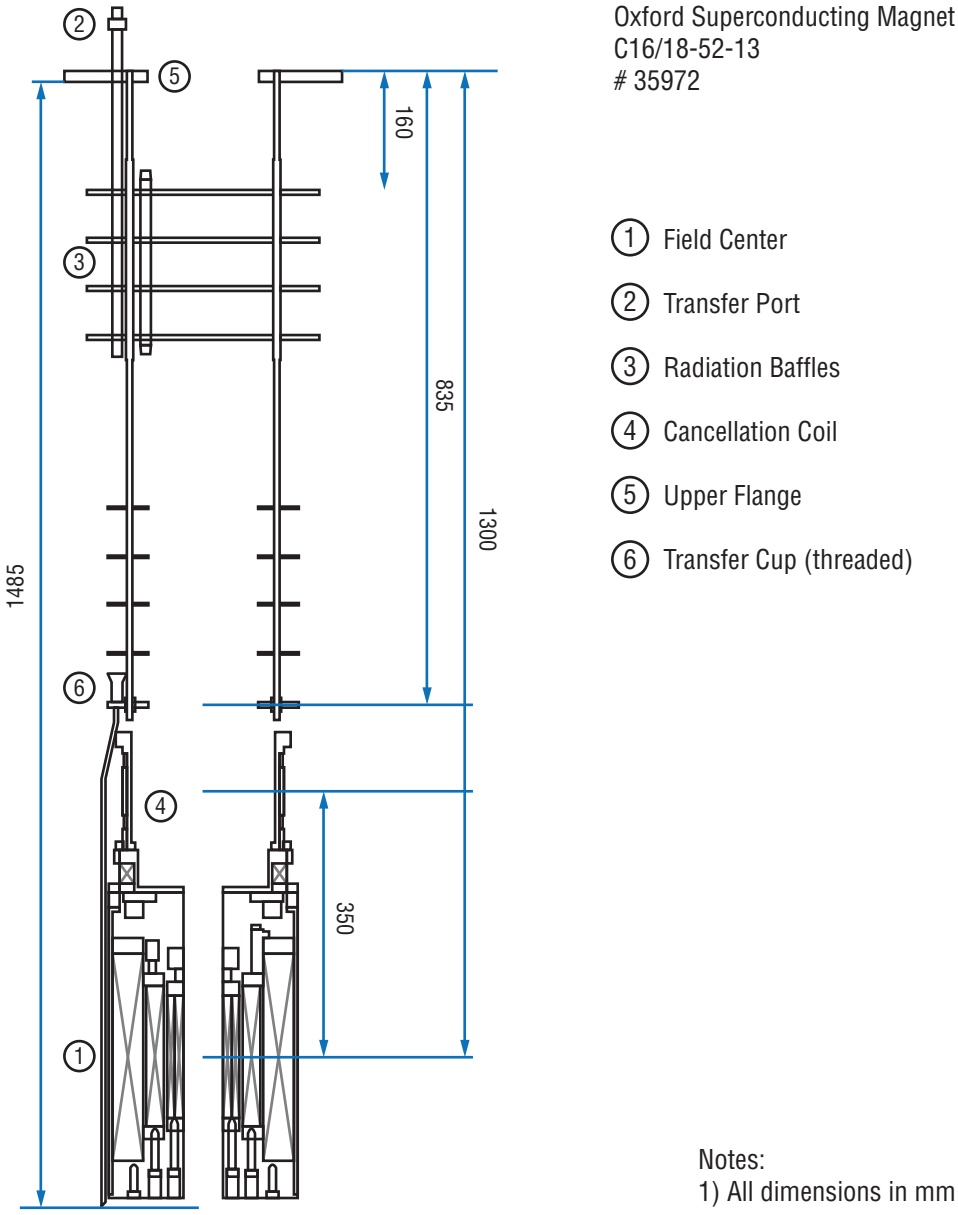

Figure E.3: The superconducting magnet schematics

E.3 AFM Body Schematics

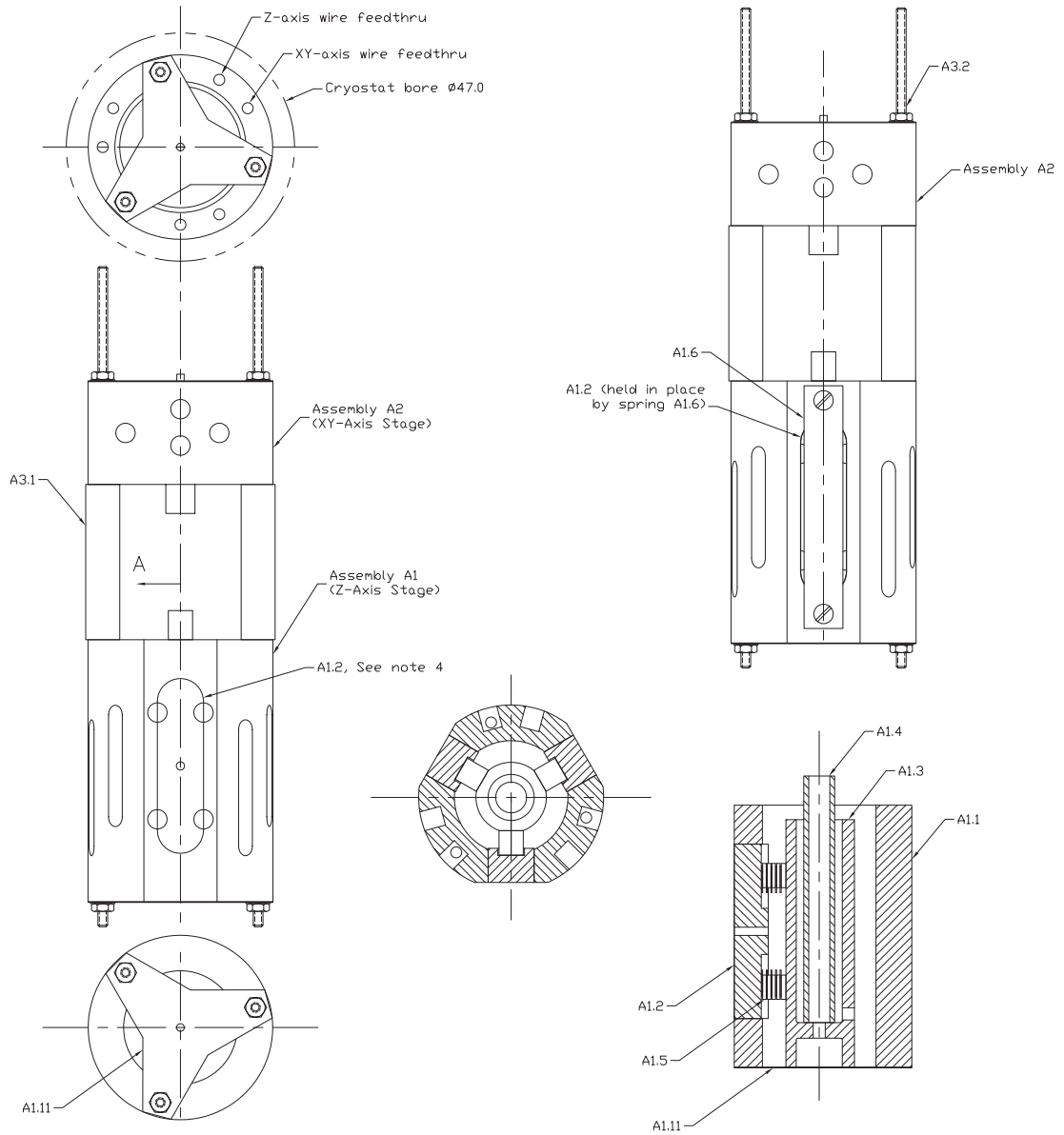

Figure E.4: Assembly instructions for the AFM (these and the following 6 figures where originally drawn by Leo Nikkinin.

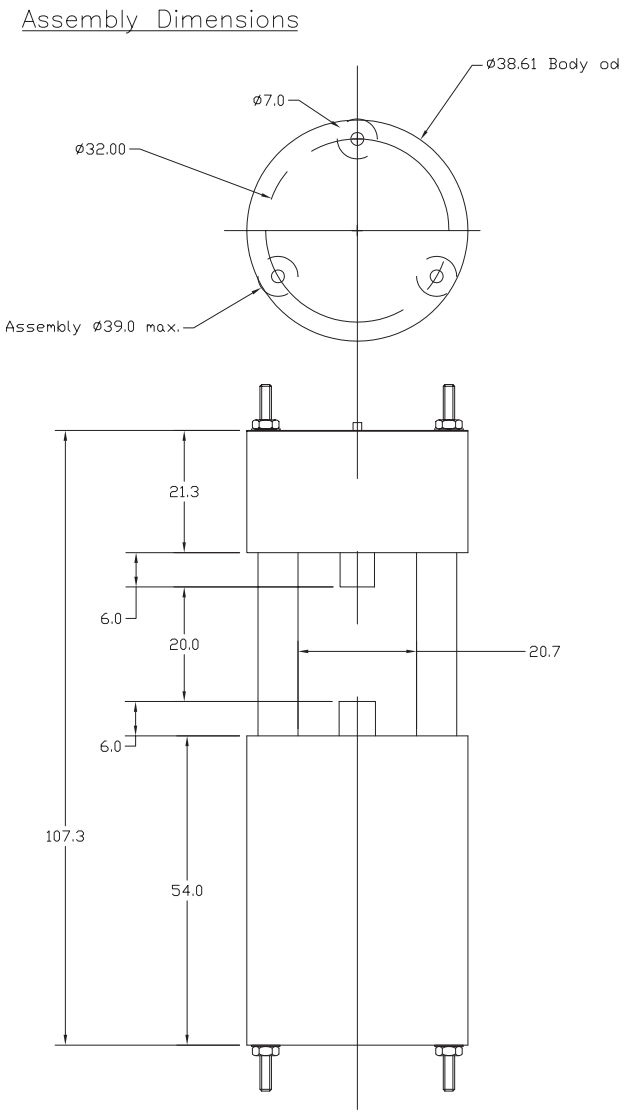

Figure E.5: Final Dimensions

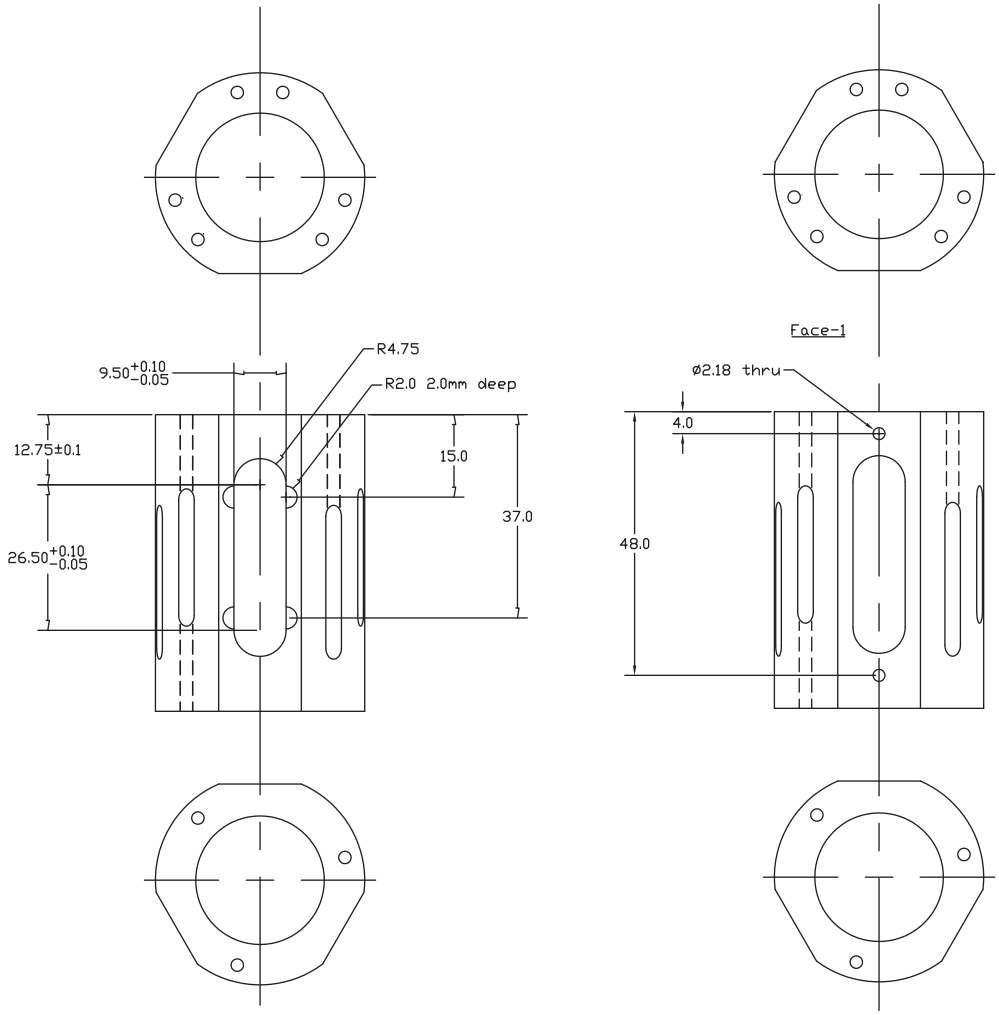

Material: Macor

Notes:
1) All dimensions in mm unless otherwise indicated [inches in square brackets]
2) Dimensions in brackets (x.xx) are for reference only

Figure E.6: Z section macor pieces

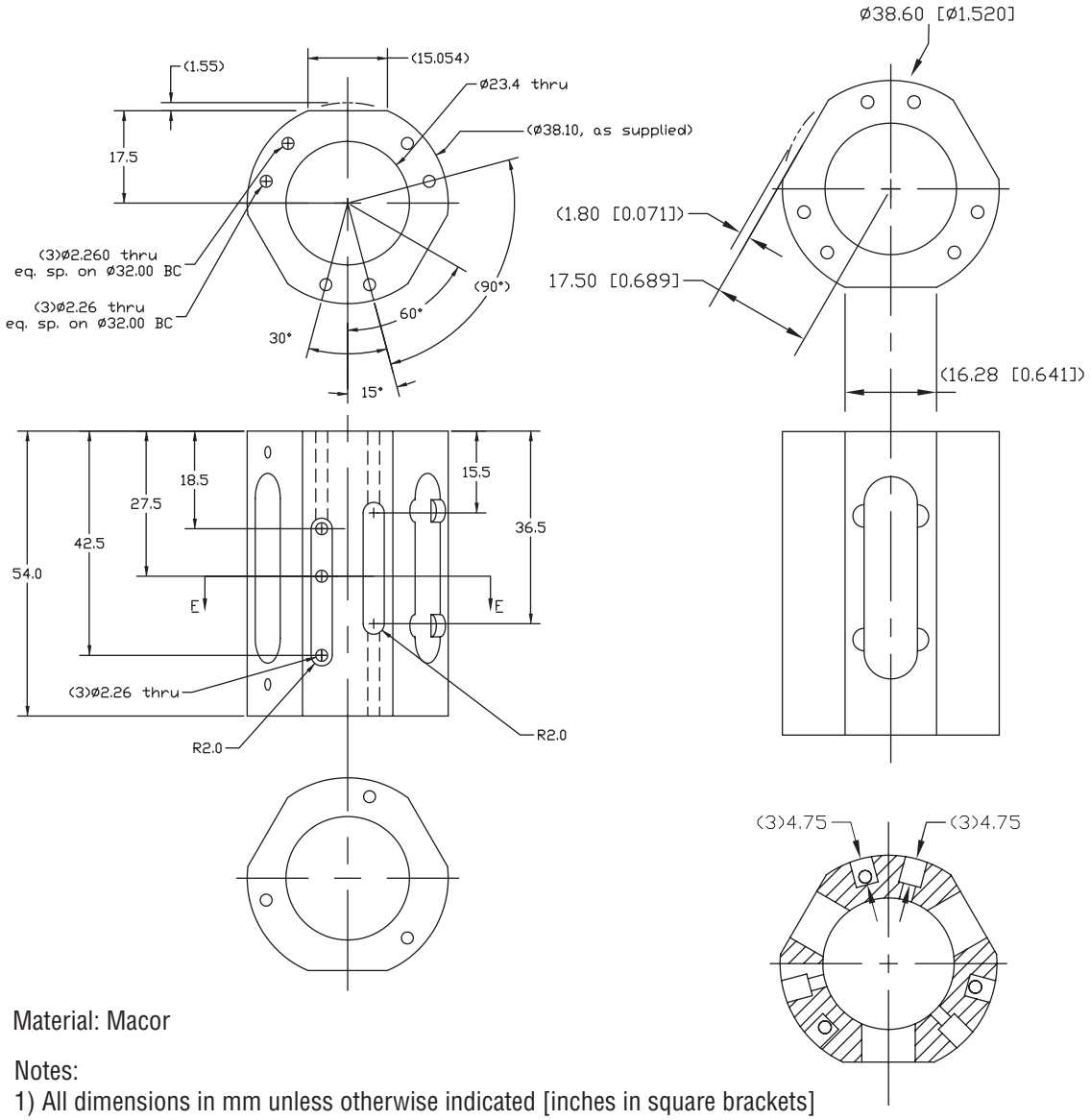

Material: Macor

Notes:
1) All dimensions in mm unless otherwise indicated [inches in square brackets]
2) Dimensions in brackets (x.xx) are for reference only

Figure E.7: Z section macor pieces, cont.

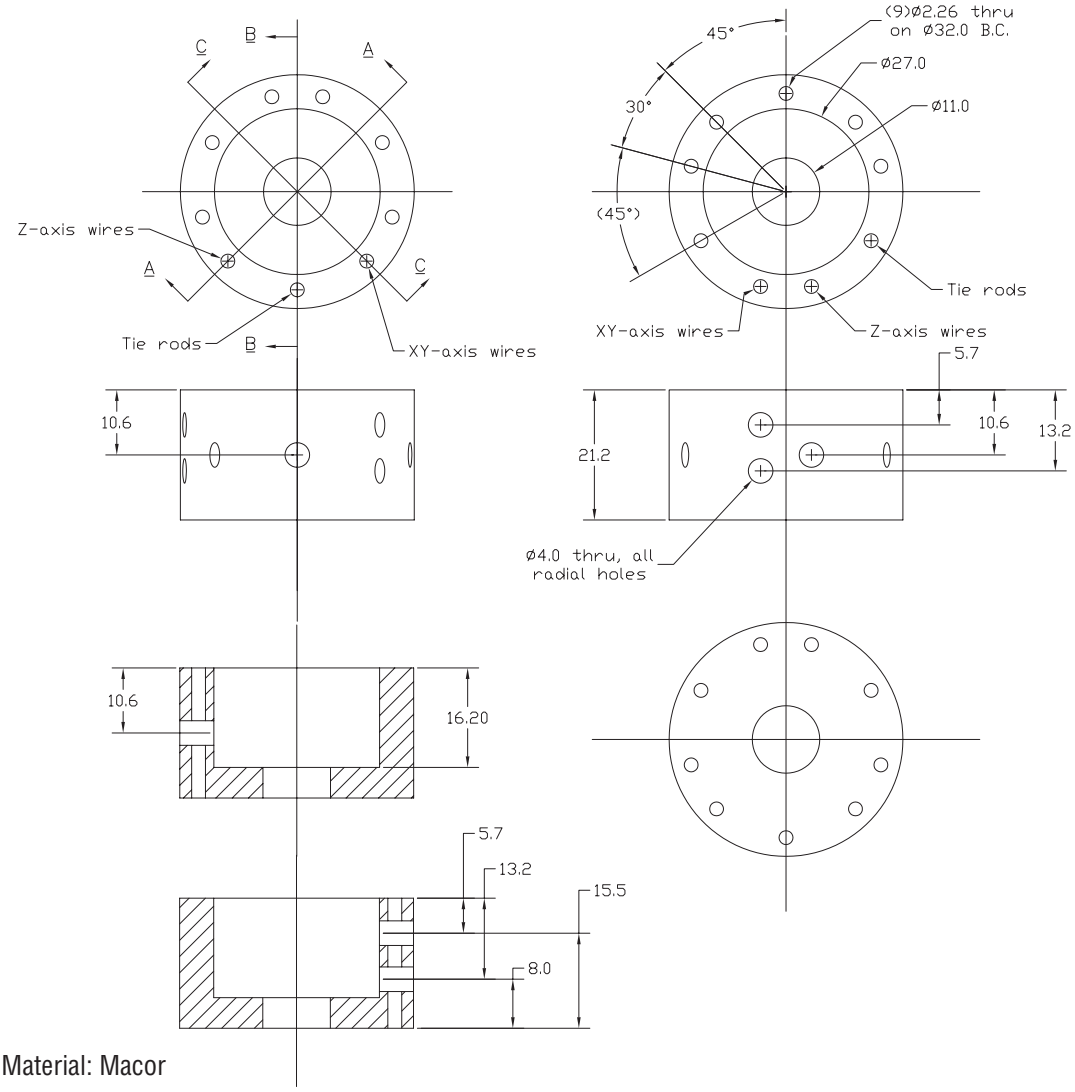

Material: Macor

Notes:
1) All dimensions in mm unless otherwise indicated [inches in square brackets]
2) Dimensions in brackets (x.xx) are for reference only

Figure E.8: XY section macor pieces

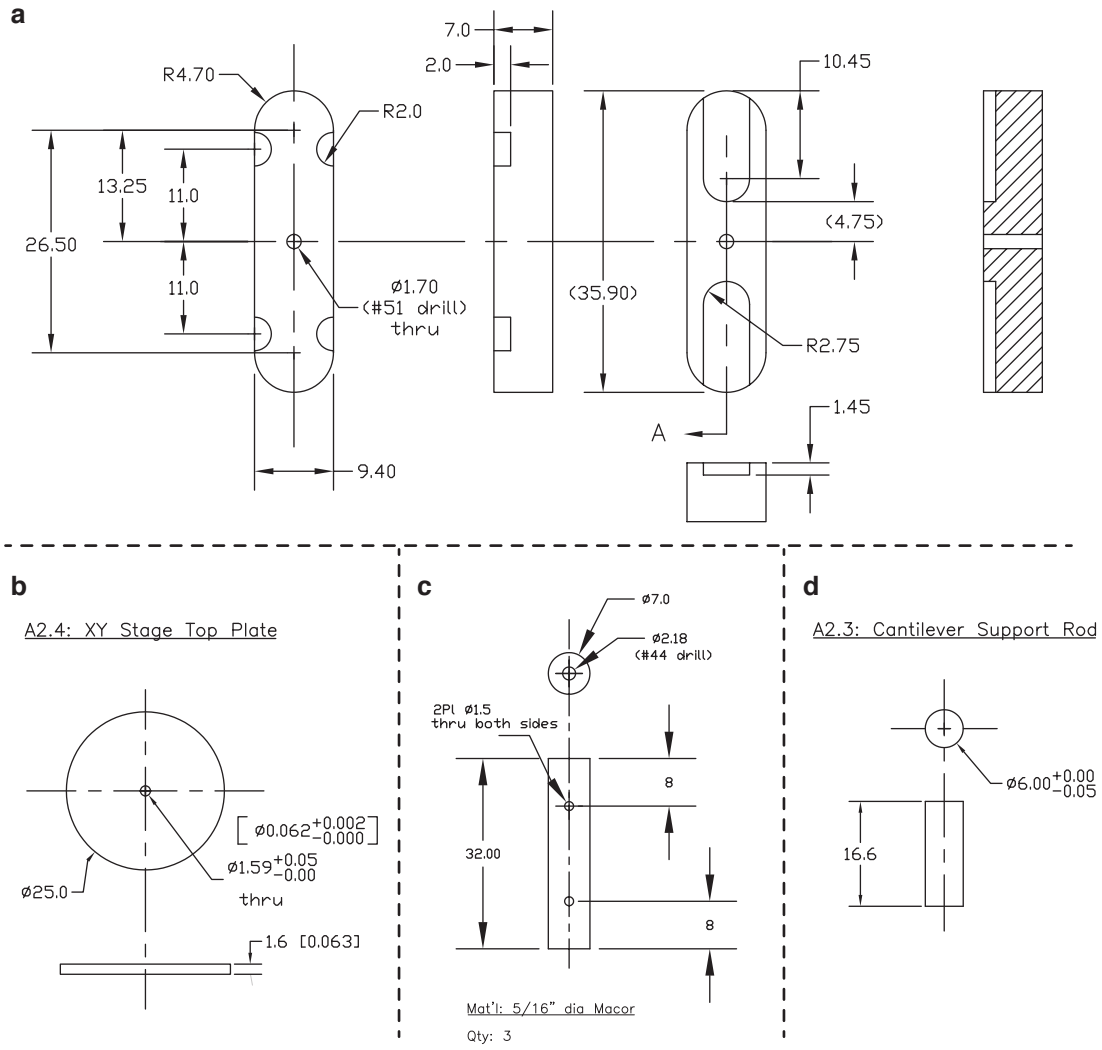

Material: Macor

Notes:
1) All dimensions in mm unless otherwise indicated [inches in square brackets]
2) Dimensions in brackets (x.xx) are for reference only

Figure E.9: **a**: The z motor shoes. **b**: xy motor compression plate. **c**: macor spacers separating the z and xy sections. **d**: tip/sample extension unit.

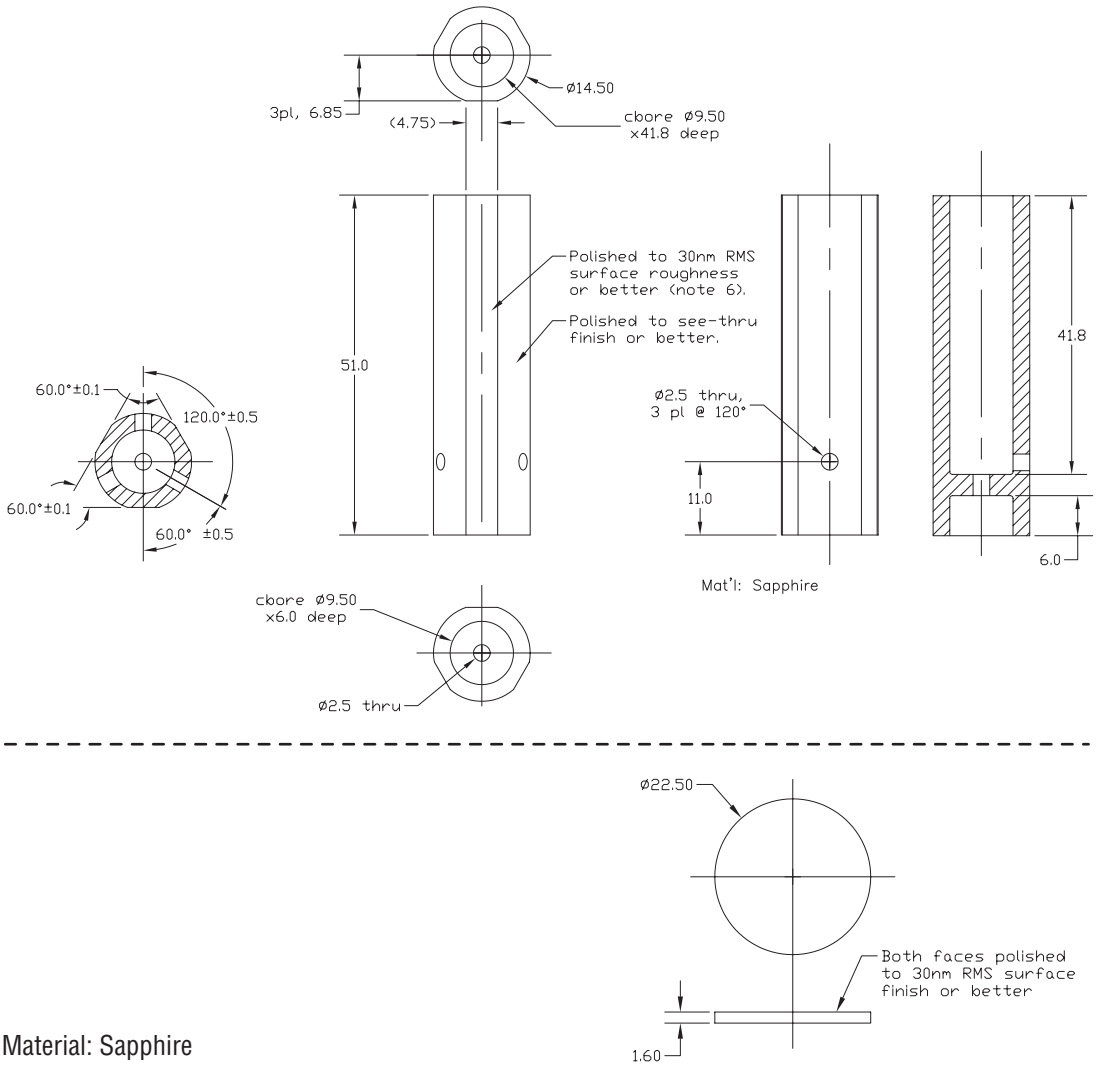

Material: Sapphire

Notes:
1) All dimensions in mm unless otherwise indicated [inches in square brackets]
2) Dimensions in brackets (x.xx) are for reference only

Figure E.10: The sapphire prism for the z motors and the disc for xy.

BIBLIOGRAPHY

[1] G. Binnig and H. Rohrer, Reviews of Modern Physics **59**, 615 (1986).

[2] G. Binnig, H. Rohrer, C. Gerber, and E. Weibel, Phys Rev Lett **49**, 57 (1982).

[3] G. Binnig, C. Quate, and C. Gerber, Phys Rev Lett **56**, 930 (1986).

[4] R. Hooke, *Lectures de potentia restitutiva, or, Of spring* (1678).

[5] R. Hooke, *Micrographia: or some physiological descriptions of minute bodies made by magnifying glasses : with observations and inquiries thereupon* (1667).

[6] F. Giessibl, Phys Rev B **56**, 16010 (1997).

[7] Y. Martin, C. Williams, and H. Wickramasinghe, J Appl Phys **61**, 4723 (1987).

[8] T. Albrecht, P. Grutter, D. Horne, and D. Rugar, J Appl Phys **69**, 668 (1991).

[9] J. Stern, B. Terris, H. Mamin, and D. Rugar, Appl Phys Lett **53**, 2717 (1988).

[10] Y. Martin, D. W. Abraham, and H. K. Wickramasinghe, Appl Phys Lett **52**, 1103 (1988).

[11] P. Tangyunyong and C. Nakakura, Journal of Vacuum Science & Technology A: Vacuum, Surfaces, and Films **21**, 1539 (2003).

[12] M. Azize, P. Girard, R. Teissier, A. Baranov, and A. Joullie, Journal of Vacuum Science & Technology B: Microelectronics and Nanometer Structures **21**, 2151 (2003).

[13] X. Xie, O. Kwon, D. Zhu, T. V. Nguyen, and G. Lin, J. Phys. Chem. B **111**, 6134 (2007).

[14] T. Matsukawa, S. Kanemaru, M. Masahara, M. Nagao, H. Tanoue, and J. Itoh, Appl Phys Lett **82**, 2166 (2003).

[15] P. Girard, Nanotechnology **12**, 485 (2001).

[16] M. Nakamura and T. Yamada, *Roadmap 2005 of Scanning Probe Microscopy: Electrostatic Force Microscopy* (Springer, 2006).

[17] S. Kalinin and A. Gruverman, *Scanning Probe Microscopy Electrical and Electromechanical Phenomena at the Nanoscale: Fundamentals and Applications* (Springer-Verlag GmbH, 2006) ISBN 9780387286679.

[18] R. Oliver, Rep. Prog. Phys. **71**, 076501 (2008).

[19] M. Planck and A. Wills, *Eight lectures on theoretical physics*, Dover books on physics (Dover Publications, 1998) ISBN 9780486697307.

[20] K. von Klitzing, G. Dorda, and M. Pepper, Phys Rev Lett **45**, 494 (1980).

[21] D. Tsui, H. L. Stormer, and A. C. Gossard, Phys Rev Lett **48**, 1559 (1982).

[22] K. Hashimoto, C. Sohrmann, J. Wiebe, T. Inaoka, F. Meier, Y. Hirayama, R. Römer, R. Wiesendanger, and M. Morgenstern, Phys Rev Lett **101**, 256802 (2008).

[23] B. Halperin, Physical Review B **25**, 2185 (1982).

[24] E. Wigner, Physical Review **46**, 1002 (1934).

[25] K. Novoselov, A. Geim, S. Morozov, D. Jiang, Y. Zhang, S. Dubonos, I. Grigorieva, and A. Firsov, Science **306**, 666 (2004).

[26] K. S. Novoselov, Z. Jiang, Y. Zhang, S. V. Morozov, H. L. Stormer, U. Zeitler, J. Maan, G. Boebinger, P. Kim, and A. K. Geim, Science **315**, 1379 (2007).

[27] J. Berezovsky, M. Borunda, E. Heller, and R. Westervelt, Nanotechnology **21**, 274013 (2010).

[28] Y. Zhang, V. Brar, C. Girit, A. Zettl, and M. Crommie, Nat Phys **5**, 722 (2009).

[29] S. Iijima, Nature **354**, 56 (1991).

[30] A. Bachtold, M. S. Fuhrer, S. Plyasunov, M. Forero, E. Anderson, A. Zettl, and P. McEuen, Phys Rev Lett **84**, 6082 (2000).

[31] A. Barboza, A. Gomes, B. Archanjo, P. Araujo, A. Jorio, A. Ferlauto, M. Mazzoni, H. Chacham, and B. Neves, Phys Rev Lett **100**, 256804 (2008).

[32] C. Staii, M. Radosavljevic, and A. Johnson, "Scanning Probe Microscopy Electrical and Electromechanical Phenomena at the Nanoscale: Fundamentals and Applications," (Springer-Verlag GmbH, 2006) Chap. Scanning Probe Microscopy of Individual Carbon Nanotube Quantum Devices, ISBN 9780387286679.

[33] B. LeRoy, Journal of Physics: Condensed Matter **15**, R1835 (2003).

[34] L. Cockins, Y. Miyahara, S. Bennett, A. Clerk, S. Studenikin, P. Poole, A. Sachrajda, and P. Grutter, P Natl Acad Sci Usa **107**, 9496 (2010).

[35] J. Bardeen, L. Cooper, and J. Schrieffer, Physical Review **108**, 1175 (1957).

[36] C. Guillemot, M. Baudet, M. Gauneau, A. Regreny, and J. Portal, Physical Review B **35**, 2799 (1987).

[37] J. Johnson, Physical Review **32**, 97 (1928).

[38] H. Nyquist, Physical Review **32**, 110 (1928).

[39] M. Kirk, T. Albrecht, and C. Quate, Rev Sci Instrum **59**, 833 (1988).

[40] F. Giessibl, C. Gerber, and G. Binnig, Journal of Vacuum Science & Technology B: Microelectronics and Nanometer Structures **9**, 984 (1991).

[41] T. Albrecht, P. Grütter, D. Rugar, and D. Smith, Ultramicroscopy **42**, 1638 (1992).

[42] M. Tortonese, R. Barrett, and C. Quate, Appl Phys Lett **62**, 834 (1993).

[43] C. Yuan, E. Batalla, M. Zacher, A. D. Lozanne, M. Kirk, and M. Tortonese, Appl Phys Lett **65**, 1308 (1994).

[44] D. Pelekhov, J. Becker, and G. N. Jr, Rev Sci Instrum **70**, 114 (1999).

[45] H. Edwards, L. Taylor, W. Duncan, and A. Melmed, J Appl Phys **82**, 980 (1997).

[46] W. Atia and C. Davis, Appl Phys Lett **70**, 405 (1997).

[47] J. Rychen, T. Ihn, P. Studerus, A. Herrmann, and K. Ensslin, Rev Sci Instrum **70**, 2765 (1999).

[48] W. Allers, A. Schwarz, U. Schwarz, and R. Wiesendanger, Rev Sci Instrum **69**, 221 (1998).

[49] P. Weitz, E. Ahlswede, J. Weis, K. von Klitzing, and K. Eberl, Physica E: Low-dimensional Systems and Nanostructures **6**, 247 (2000).

[50] H. Hug, B. Stiefel, P. van Schendel, A. Moser, S. Martin, and H. Güntherodt, Rev Sci Instrum **70**, 3625 (1999).

[51] M. Liebmann, A. Schwarz, S. Langkat, and R. Wiesendanger, Rev Sci Instrum **73**, 3508 (2002).

[52] P. Weitz, E. Ahlswede, J. Weis, K. von Klitzing, and K. Eberl, Applied Surface Science **157**, 349 (2000).

[53] T. Ihn, *Electronic quantum transport in mesoscopic semiconductor structures* (Springer Verlag, 2004).

[54] A. Gildemeister, T. Ihn, C. Barengo, P. Studerus, and K. Ensslin, Rev Sci Instrum **78**, 013704 (2007).

[55] N. Moussy, H. Courtois, and B. Pannetier, Rev Sci Instrum **72**, 128 (2001).

[56] J. Senzier, P. Luo, and H. Courtois, Appl Phys Lett **90**, 043114 (2007).

[57] M. Pala, B. Hackens, F. Martins, H. Sellier, V. Bayot, S. Huant, and T. Ouisse, Phys Rev B **77**, 125310 (2008).

[58] S. Kičin, A. Pioda, T. Ihn, K. Ensslin, D. Driscoll, and A. Gossard, Phys Rev B **70**, 205302 (2004).

[59] N. Aoki, C. D. Cunha, R. Akis, D. K. Ferry, and Y. Ochiai, Phys Rev B **72**, 155327 (2005).

[60] A. Baumgartner, T. Ihn, K. Ensslin, G. Papp, F. Peeters, K. Maranowski, and A. C. Gossard, Phys Rev B **74**, 165426 (2006).

[61] M. Topinka, B. LeRoy, S. Shaw, E. Heller, R. Westervelt, K. Maranowski, and A. C. Gossard, Science **289**, 2323 (2000).

[62] S. Chakraborty, I. Maasilta, S. Tessmer, and M. Melloch, Phys Rev B **69**, 73308 (2004).

[63] K. L. McCormick, M. T. Woodside, M. Huang, P. L. McEuen, C. Duruoz, and J. Harris, Jr, Physica B: Condensed Matter **249-251**, 79 (1998).

[64] P. Glicofridis, G. Finkelstein, R. C. Ashoori, and M. Shayegan, Phys Rev B **65**, 121312 (2002).

[65] S. Tessmer, P. Glicofridis, R. Ashoori, L. Levitov, and M. Melloch, Nature **392**, 51 (1998).

[66] R. Crook, R. Schneble, M. Kataoka, H. Beere, D. Ritchie, D. Anderson, G. Jones, C. Smith, C. Ford, and C. Barnes, Phys Rev B **78**, 125330 (2008).

[67] N. Zhitenev, T. Fulton, A. Yacoby, H. Hess, L. N. Pfeiffer, and K. W. West, Nature **404**, 473 (2000).

[68] J. Hedberg, A. Lal, Y. Miyahara, P. Grütter, G. Gervais, M. Hilke, L. Pfeiffer, and K. West, Appl Phys Lett **97**, 143107 (2010).

[69] Corning, "Macor: Machinable Glass Ceramic," `http://www.corning.com/docs/specialtymaterials/pisheets/Macor.pdf`.

[70] S. Pan, E. Hudson, and J. Davis, Rev Sci Instrum **70**, 1459 (1999).

[71] C. Meyer, O. Sqalli, H. Lorenz, and K. Karrai, Rev Sci Instrum **76**, 063706 (2005).

[72] A. Stemmer and A. Engel, Ultramicroscopy **34**, 129 (1990).

[73] S. Moheimani, Rev Sci Instrum **79**, 071101 (2008).

[74] K. Brown, L. Sun, and B. Kane, Rev Sci Instrum **75**, 2029 (2004).

[75] M. Roseman and P. Grütter, Rev Sci Instrum **71**, 3782 (2000).

[76] D. Pohl, Rev Sci Instrum **58**, 54 (1987).

[77] P. Niedermann, R. Emch, and P. Descouts, Rev Sci Instrum **59**, 368 (1988).

[78] S. Field and J. Barentine, Rev Sci Instrum **71**, 2603 (2000).

[79] H. Yoda, H. Ikeda, and Y. Yamabe, 26th Annual Symposium on Frequency Control, 140(1972).

[80] D. Sarid, *Scanning force microscopy: with applications to electric, magnetic, and atomic forces*, Oxford series on optical sciences (Oxford University Press, 1994) ISBN 9780195092042.

[81] J. Brice, Reviews of Modern Physics **57**, 105 (1985).

[82] B. Ng, Y. Zhang, S. W. Kok, and Y. C. Soh, Ultramicroscopy **109**, 291 (2009).

[83] F. Giessibl, Appl Phys Lett **73**, 3956 (1998).

[84] S. Rozhok and V. Chandrasekhar, Solid State Commun **121**, 683 (2002).

[85] P. Bryant, H. Kim, Y. Zheng, and R. Yang, Rev Sci Instrum **58**, 1115 (1987).

[86] T. Hagedorn(2010), In preparation.

[87] F. Giessibl and B. Trafas, Rev Sci Instrum **65**, 1923 (1994).

[88] S. Butterworth, Proceedings of the Physical Society of London **27**, 410 (1914).

[89] D. Dye, Proceedings of the Physical Society of London **38**, 399 (1925).

[90] R. Grober, J. Acimovic, J. Schuck, D. Hessman, P. Kindlemann, J. Hespanha, A. Morse, K. Karrai, I. Tiemann, and S. Manus, Rev Sci Instrum **71**, 2776 (2000).

[91] P. Kern, RFDesign, 26(2007).

[92] P. Zahl, T. Wagner, R. Möller, and A. Klust, J Vac Sci Technol B **28**, C4E39 (2010).

[93] P. Zahl, M. Bierkandt, S. Schröder, and A. Klust, Rev Sci Instrum **74**, 1222 (2003).

[94] G. White and P. Meeson, *Experimental Techniques in Low Temperature Physics* (Oxford Science Publications, 2002).

[95] H. Hall, P. Ford, and K. Thompson, Cryogenics **6**, 80 (1966).

[96] A. Anderson, W. Roach, R. Sarwinski, and J. Wheatley, Phys Rev Lett **16**, 263 (1966).

[97] D. Greywall, Physical Review B **27**, 2747 (1983).

[98] *Experimental Techniques in Condensed Matter Physics at Low Temperatures*, edited by E. N. S. Robert C. Richardson (Addison-Wesley, Reading, Massachusetts, 1998).

[99] C. T. V. Degrift, Physica **107B**, 605 (1981).

[100] J. Ekin, *Experimental techniques for low-temperature measurements: cryostat design, material properties, and superconductor critical-current testing* (Oxford University Press, 2006).

[101] F. Pobell, *Matter and methods at low temperatures* (Springer Verlag, 2007).

[102] C. Hagmann and P. Richards, Cryogenics **35**, 345 (1995).

[103] H. Ott, *Noise Reduction Techniques in Electronic Systems* (John Wiley and Sons, New York, 1976).

[104] M. Okano, K. Kajimura, S. Wakiyama, F. Sakai, W. Mizutani, and M. Ono, Journal of Vacuum Science & Technology A: Vacuum, Surfaces, and Films **5**, 3313 (1987).

[105] A. Oliva, M. Aguilar, and V. Sosa, Measurement Science and Technology **9**, 383 (1998).

[106] W. Kirk and M. Twerdochlib, Rev Sci Instrum **49**, 765 (1978).

[107] S. Pirro, A. Alessandrello, C. Brofferio, C. Bucci, O. Cremonesi, E. Coccia, E. Fiorini, V. Fafone, A. Giuliani, and A. Nucciotti, Nuclear Instruments and Methods in Physics Research Section A: Accelerators, Spectrometers, Detectors and Associated Equipment **444**, 331 (2000).

[108] R. Bhatia, J. Bock, P. Ade, A. Benoît, T. Bradshaw, B. Crill, M. Griffin, I. Hepburn, V. Hristov, and A. Lange, Cryogenics **39**, 701 (1999).

[109] P. Gorla, C. Bucci, and S. Pirro, Nuclear Instruments and Methods in Physics Research Section A: Accelerators, Spectrometers, Detectors and Associated Equipment **520**, 641 (2004).

[110] A. Raccanelli, L. Reichertz, and E. Kreysa, Cryogenics **41**, 763 (2001).

[111] "Palatine Precision LTD," `http://www.paletineprecision.co.uk`.

[112] M. Locatelli, G. Lamboley, J. Michenaud, and V. Bayot, Rev Sci Instrum **59**, 661 (1988).

[113] C. Chen, Appl Phys Lett **60**, 132 (1992).

[114] K. Vandervoort, R. Zasadzinski, G. Galicia, and G. Crabtree, Rev Sci Instrum **64**, 896 (1993).

[115] H. Fukuyama, H. Tan, T. Handa, T. Kumakura, and M. Morishita, Czechoslovak Journal of Physics **46**, 2847 (1996).

[116] Y. Qin and R. Reifenberger, Rev Sci Instrum **78**, 063704 (2007).

[117] F. Giessibl, Appl Phys Lett **76**, 1470 (2000).

[118] S. Moheimani and A. Fleming, *Piezoelectric transducers for vibration control and damping* (Springer Berlin, 2006).

[119] R. Bechmann, Physical Review **110**, 1060 (1958).

[120] J. Liu, A. Callegari, M. Stark, and M. Chergui, Ultramicroscopy **109**, 81 (2008).

[121] G. Graham and F. Pereira, J Appl Phys **42**, 3011 (1971).

[122] A. G. Beda, Soviet Physics - Solid State **9**, 1043 (1967).

[123] S. Hembacher, F. Giessibl, and J. Mannhart, Applied Surface Science **188**, 445 (2002).

[124] P. Mohanty, D. Harrington, K. Ekinci, Y. Yang, M. Murphy, and M. L. Roukes, Physical Review B **66**, 85416 (2002).

[125] U. Dürig, H. Steinauer, and N. Blanc, J Appl Phys **82**, 3641 (1997).

[126] F. Giessibl, Reviews of Modern Physics **75**, 949 (2003).

[127] L. Gross, F. Mohn, P. Liljeroth, J. Repp, F. Giessibl, and G. Meyer, Science **324**, 1428 (2009).

[128] F. Giessibl, Appl Phys Lett **78**, 123 (2001).

[129] J. Sader and S. Jarvis, Appl Phys Lett **84**, 1801 (2004).

[130] M. Barbic, L. Eliason, and J. Ranshaw, Sensors and Actuators A **136**, 564 (2007).

[131] M. Jura, M. Topinka, L. Urban, A. Yazdani, H. Shtrikman, L. Pfeiffer, K. West, and D. Goldhaber-Gordon, Nat Phys **3**, 841 (2007).

[132] M. Woodside and P. L. Mceuen, Science **296**, 1098 (2002).

[133] J. Rychen, T. Ihn, P. Studerus, A. Herrmann, K. Ensslin, H. Hug, P. van Schendel, and H. Güntherodt, Rev Sci Instrum **71**, 1695 (2000).

[134] M. Suddards, *Scanning Capacitance Microscopy in the Quantum Hall Regime*, Ph.D. thesis, University of Nottingham (2009).

[135] D. Clubb, O. Buu, R. Bowley, R. Nyman, and J. Owers-Bradley, Journal of Low Temperature Physics **136**, 1 (2004).

[136] K. Karraī and R. Grober, Ultramicroscopy **61**, 197 (1995).

[137] D. Bradley, P. Crookston, S. Fisher, A. Ganshin, A. Guénault, R. Haley, M. Jackson, G. Pickett, R. Schanen, and V. Tsepelin, Journal of Low Temperature Physics **157**, 476 (2009).

[138] A. Cleland and M. L. Roukes, Sensors and Actuators A **72**, 256 (1999).

[139] K. Schwab, Appl Phys Lett **80**, 1276 (2002).

[140] A. Carl, G. Dumpich, and D. Hallfarth, Physical Review B **39**, 915 (1989).

[141] R. C. Munoz, M. A. Suárez, S. Oyarzún, R. Henríquez, A. Espinosa, G. Kremer, L. Moraga, S. Cancino, and R. Morales, Physical Review B **81**, 165408 (2010).

[142] L. N. Pfeiffer, K. West, H. L. Stormer, J. Eisenstein, K. W. Baldwin, D. Gershoni, and J. Spector, Appl Phys Lett **56**, 1697 (1990).

[143] H. L. Stormer, Reviews of Modern Physics **71**, 875 (1999).

[144] H. L. Stormer, R. Dingle, A. Gossard, W. Wiegmann, and M. Sturge, Solid State Commun **29**, 705 (1979).

[145] M. Grayson, C. Kurdak, D. T. Tsui, S. Parihar, S. Lyon, and M. Shayegan, Solid-State Electronics **40**, 233 (1996).

[146] E. Hall, American Journal of Mathematics **2**, 287 (1879).

[147] D. Yennie, Reviews of Modern Physics **59**, 781 (1987).

[148] D. Chklovskii, B. Shklovskii, and L. Glazman, Physical Review B **46**, 4026 (1992).

[149] E. Ahlswede, P. Weitz, J. Weis, K. von Klitzing, and K. Eberl, Physica B: Condensed Matter **298**, 562 (2001).

[150] M. Suddards, A. Baumgartner, C. Mellor, and M. Henini, Physica E: Low-dimensional Systems and Nanostructures **40**, 1548 (2008).

[151] G. Granger, J. Eisenstein, and J. Reno, Phys Rev Lett **102**, 86803 (2009).

[152] M. Grayson, L. Steinke, M. Huber, D. Schuh, M. Bichler, and G. Abstreiter, phys. stat. sol. (b) **245**, 356 (2008).

[153] F. Milliken, C. Umbach, and R. Webb, Solid State Commun **97**, 309 (1996).

[154] I. Maasilta and V. Goldman, Physical Review B **55**, 4081 (1997).

[155] M. Hilke, D. Tsui, M. Grayson, L. N. Pfeiffer, and K. West, Phys Rev Lett **87**, 186806 (2001).

[156] M. Grayson, Solid State Commun **140**, 66 (2006).

[157] A. Chang, Reviews of Modern Physics **75**, 1449 (2003).

[158] A. Chang, L. N. Pfeiffer, and K. West, Phys Rev Lett **77**, 2538 (1996).

[159] M. Grayson, *Tunneling Into the Edge of a Two-Dimensional Electron System*, Ph.D. thesis, Princeton University (1998).

[160] M. Woodside, C. Vale, K. L. McCormick, P. L. Mceuen, C. Kadow, K. Maranowski, and A. C. Gossard, Physica E: Low-dimensional Systems and Nanostructures **6**, 238 (2000).

[161] J. Jackson, *Classical electrodynamics*, Classical Electrodynamics No. v. 1998 (Wiley, 1999) ISBN 9780471309321.

[162] K. McCormick, *Electrical Probes of Mesoscopic Systems with a Low Temperature Atomic Force Microscope*, Ph.D. thesis, University of California, Berekely (1998).

[163] G. Steele, *Imaging Transport Resonances in the Quantum Hall Effect*, Ph.D. thesis, MIT (2006).

[164] S. Adachi, J Appl Phys **58**, R1 (1985).

[165] C. Geuzaine and J. Remacle, "GMesh:a three-dimensional finite element mesh generator with built-in pre- and post-processing facilities," `http://geuz.org/gmsh/`.

[166] CSC-IT Center for Science Ltd, "Elmer: Open Source Finite Element Software for Multiphysical Problems," `http://www.csc.fi/english/pages/elmer`.

[167] H. Fertig, Physics **2**, 15 (2009).

[168] C. Altimiras, H. L. Sueur, U. Gennser, A. Cavanna, D. Mailly, and F. Pierre, Nat Phys **6**, 34 (2009).

[169] X. Du, I. Skachko, F. Duerr, A. Luican, and E. Andrei, Nature **462**, 192 (2009).

[170] Y. Zhang, Y. Tan, H. L. Stormer, and P. Kim, Nature **438**, 201 (2005).

[171] K. Bolotin, F. Ghahari, M. Shulman, H. L. Stormer, and P. Kim, Nature **462**, 196 (2009).

[172] R. Tung, T. Wutscher, D. Martinez-Martin, R. G. Reifenberger, F. Giessibl, and A. Raman, J Appl Phys **107**, 104508 (2010).

[173] P. Curie and J. Curie, Comptes rendus hebdomadaires des séances de l'Académie des sciences, 294(1880).

[174] W. Mason, Journal of the Acoustical Society of America **70**, 1561 (1981).

[175] S. Katzir, *The beginnings of piezoelectricity: a study in mundane physics*, Boston studies in the philosophy of science (Springer, 2006) ISBN 9781402046698.

[176] R. Ballas, *Piezoelectric multilayer beam bending actuators: static and dynamic behavior and aspects of sensor integration*, Microtechnology and MEMS (Springer, 2007) ISBN 9783540326410.

[177] H. Kragh, Physics in Perspective (PIP) **10**, 379 (2008).

[178] W. Bragg and R. Gibbs, Proceedings of the Royal Society of London. Series A, Containing Papers of a Mathematical and Physical Character, 405(1925).

[179] R. Gibbs, Proceedings of the Royal Society of London. Series A, Containing Papers of a Mathematical and Physical Character, 443(1926).

[180] T. Zhang, Y. Zheng, C. Jianjun, S. Lixin, and S. Erwei, Japanese Journal of Applied Physics **45**, 8755 (2006).

[181] G. Fowles and G. Cassiday, *Analytical mechanics* (Thomson Brooks/Cole, 2005) ISBN 9780534494926.

[182] C. Chen, *Introduction to scanning tunneling microscopy*, Monographs on the physics and chemistry of materials (Oxford University Press, 2007) ISBN 9780199211500.

[183] S. Smith and D. Chetwynd, *Foundations of ultra-precision mechanism design* (Gordon and Breach Scientific Publishers, 1992).